Optimal design of a residential hybrid microgrid system for enhancing renewable energy deployment and energy use efficiency

吉田, 雄一郎
九州大学大学院総合理工学府環境エネルギー工学専攻

OPTIMAL DESIGN OF A RESIDENTIAL HYBRID MICROGRID SYSTEM FOR ENHANCING RENEWABLE ENERGY DEPLOYMENT AND ENERGY USE EFFICIENCY

Yuichiro Yoshida

Supervisor
Associate Professor. Hooman Farzaneh

February 2020

Energy and Environmental System Laboratory,
Department of Energy and Environmental Engineering
Interdisciplinary Graduate School of Engineering Sciences

KYUSHU UNIVERSITY
Japan

CONTENTS

LIST OF TABLES

LIST OF FIGURES

ABSTRACT

After the Great East Japan Earthquake, energy security and vulnerability have become important issues facing the Japanese energy system. Besides, due to increased energy demand, the dramatic consumption of fossil fuels and rising energy prices are inevitable. As such, the transition to Renewable Energy Resources (RER) can be considered an essential solution to the problems arising from the widespread use of fossil fuels in the Japanese power industry. As one of these solutions, the integration of renewable energy sources to meet specific regional energy demand is a promising scenario to overcome the challenges of renewable energy.

In this study, modeling and simulation of a fully autonomous microgrid system is conducted in order to find the optimal configuration autonomous microgrid system that can be used to meet the power demand of a small community in Kasuga City, Fukuoka, using the least cost-perspective approach. The proposed microgrid system in this study consists of a cluster of loads and micro sources such as the wind turbines, solar photovoltaic panels, battery storage, and a diesel generator. The simulation part is developed to estimate the electrical power generated by each component, taking into account the variation of the weather parameters such as wind, solar irradiation and ambient temperature. The optimal system design is then based on using a PSO algorithm. Design variables, the capacity of each component, are defined as vectors, which are called particles. The total cost of the system is considered as the objective function of the optimization.

Based on the model results, the optimal size of the main components of the system was estimated as: PV: 2.65 kW, wind power: 2.01 kW, battery: 14.86kW, diesel generator: 3.6 kW, converter: 2.8 kW. The total cost of the proposed system was estimated at 4.65 million yen. The LCOE of the proposed system was estimated at 95.3 yen / kWh, which is much higher than the average electricity rate in Japan (22 yen / kWh). The share of each power source in supplying the annual electrical load demand of the selected building was estimated as: 43.4% solar PV, 16.7% wind, 4.9% diesel generator, and 35% battery discharge. The model results revealed that the power loss due to the charging and discharging efficiency of the battery is extremely large at about 720 kWh per year.

The results also revealed the remarkable impact of weather conditions on power generation from the proposed microgrid and showed that the Day-ahead forecasting of the weather data could help in managing the battery operation through monitoring its SOC condition and lowering the usage of diesel generator in order to reduce its cost and environmental impacts on the system.

ACKNOWLEDGMENT

Foremost, I would like to express my sincere gratitude to my supervisor, Associate Prof. Hooman Farzaneh, for the continuous support of my master's study and research, for his patience, motivation, enthusiasm, and immense knowledge. His guidance helped me in all the time of research and writing of this thesis. I could not have imagined having a better advisor and mentor for my master's study.

I am thankful to Naoto Takatsu who gives me some useful assistance and inspiration for this works. The discussion with him often made produce a beneficial effect on my research.

I also express my gratitude to Ayas Shaqour for his precious assistance, encouragement, and discussion in my research.

I am thankful to all of members of our laboratory members (Energy and Environment System Lab.) and staff for their help and cooperation.

Last but not the least, I would like to thank my family: my parents Kazuo Yoshida and Yuki Yoshida, for giving birth to me in the first place and supporting me spiritually throughout my life.

Yuichiro Yoshida

Chapter 1

Introduction

1.1 Energy situation in Japan

Japan has limited fossil fuel resources. As shown in Figure 1.1. Japan's energy self-sufficiency rate was as low as 9.6% in 2017, indicating that energy security issue in this country [1]. The energy self-sufficiency rate indicates the proportion of primary energy required for daily life and economic activities that can be secured in the country.

After the Great East Japan Earthquake, it became clear that energy security and vulnerability are critical issues facing the Japanese energy system. Besides, as shown in Figure 1.2, the large-scale blackout associated with the Eastern Hokkaido Iburi Earthquake reminded us once again the vulnerability of the energy infrastructure in Japan.

In addition, since the Paris Agreement came into effect, Japan has been focusing on reducing and decarbonizing its energy system. Therefore, in Japan, 3E + S (3E (Energy Security, Economic Efficiency, Environment) + S (Safety)) is adopted as an energy policy.

1.2 Overview of energy supply and demand in Japan

Since the 1970s, energy consumption has increased in Japan, due to the high economic growth, however, the impact of the oil shock promoted energy conservation. As shown in Figure 1.3, energy consumption peaked in fiscal 2005 due to the rise in crude oil prices since the mid-2000s. The 2011 Great East Japan Earthquake has raised awareness of energy conservation, and energy consumption has been declining. Figure 1.4 shows the improvement trend in Japan's final energy intensity.

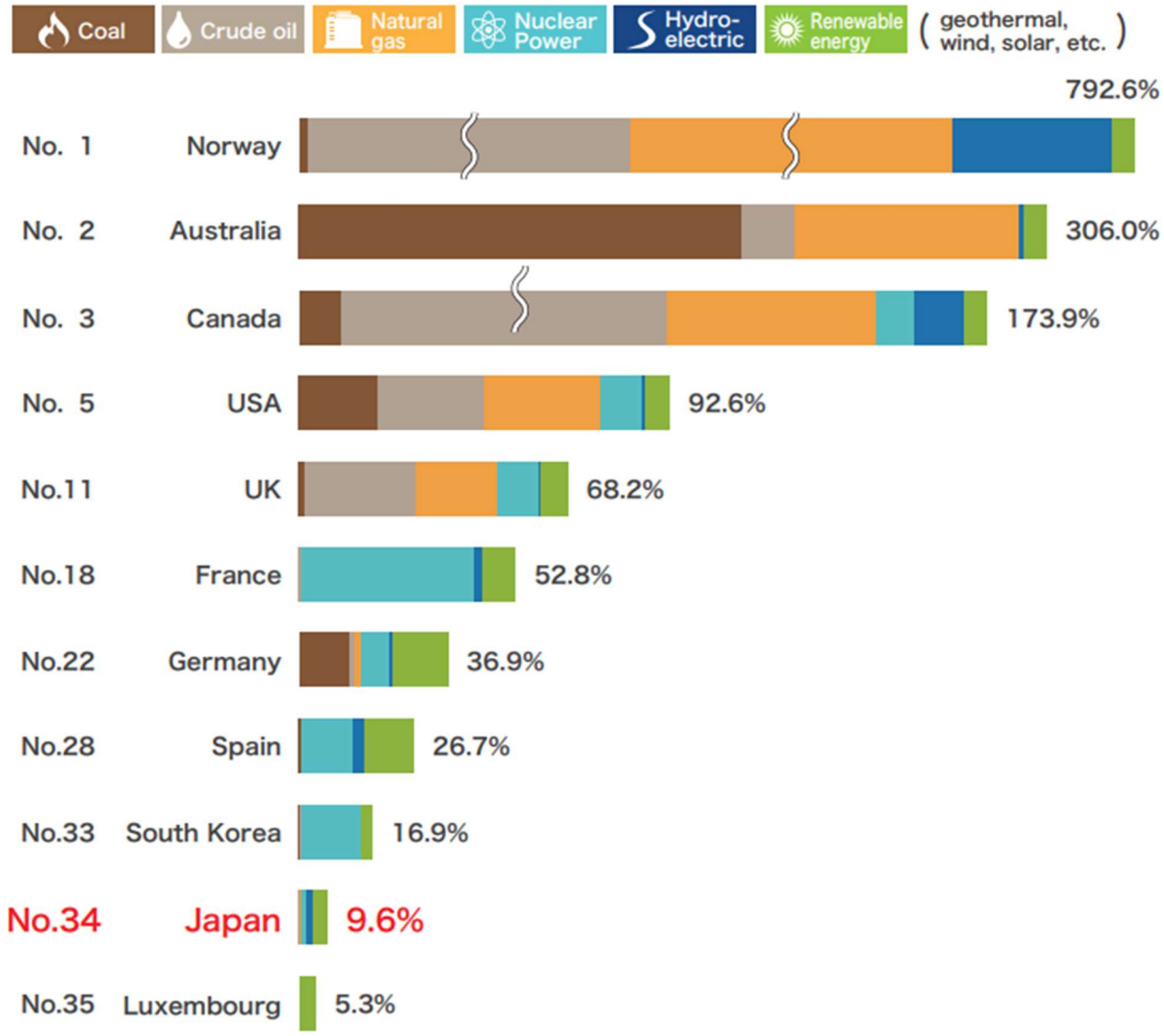

Figure 1.1: Comparison of primary energy self-sufficiency rates in major countries (2017). Addopted from Ref. [2].

The first oil shock in 1973 triggered the diversification of power sources in Japan. Due to the Great East Japan Earthquake, nuclear power plants were phased out one after another. The major sources of electricity generation in 2017 were LNG thermal power 39.8% (420.1 billion kWh), coal–based power 32.3% (340.6 billion kWh), Oil-based power 8.7% (92 billion kWh), Renewable energy 8.1% (85.5 billion kWh), hydro power 8.0% (84.9 billion kWh) and nuclear power 3.1% (32.9 billion kWh). As shown in the Figure 1.5, the use of thermal power generation increased due to the impact of the Great East Japan Earthquake in 2011 which has resulted in increasing the electricity prices in Japan (Figure 1.6).

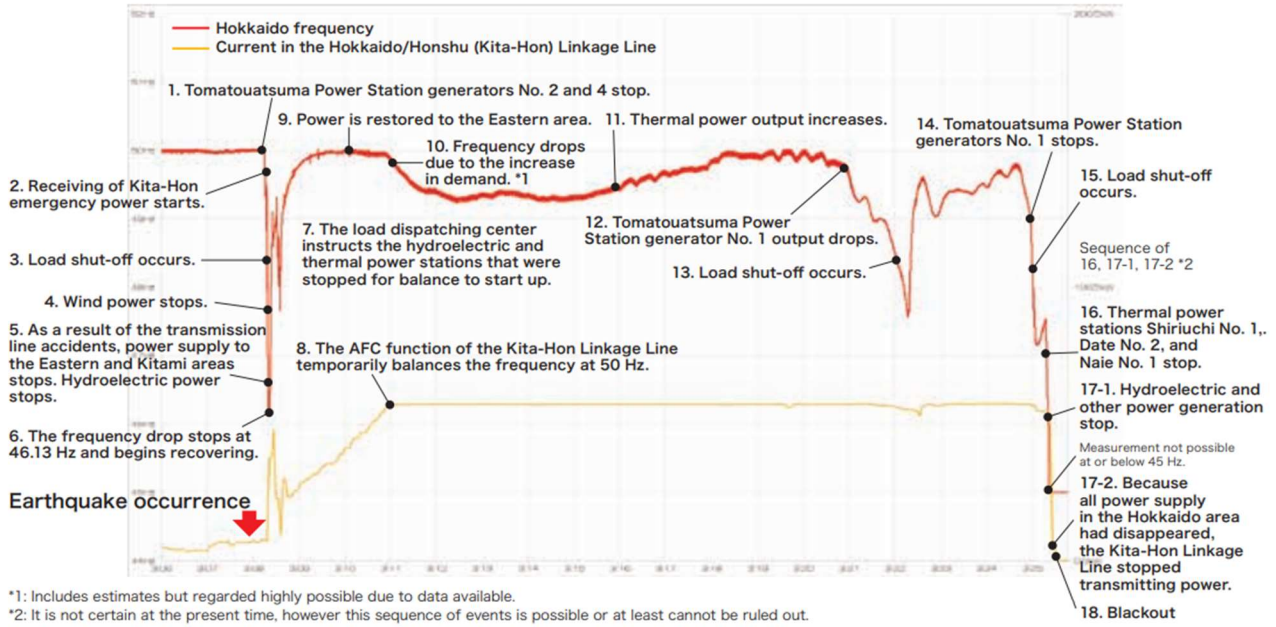

Figure 1.2: Blackout in 18 minutes by the Eastern Hokkaido Iburi Earthquake. adopted from Ref. [2].

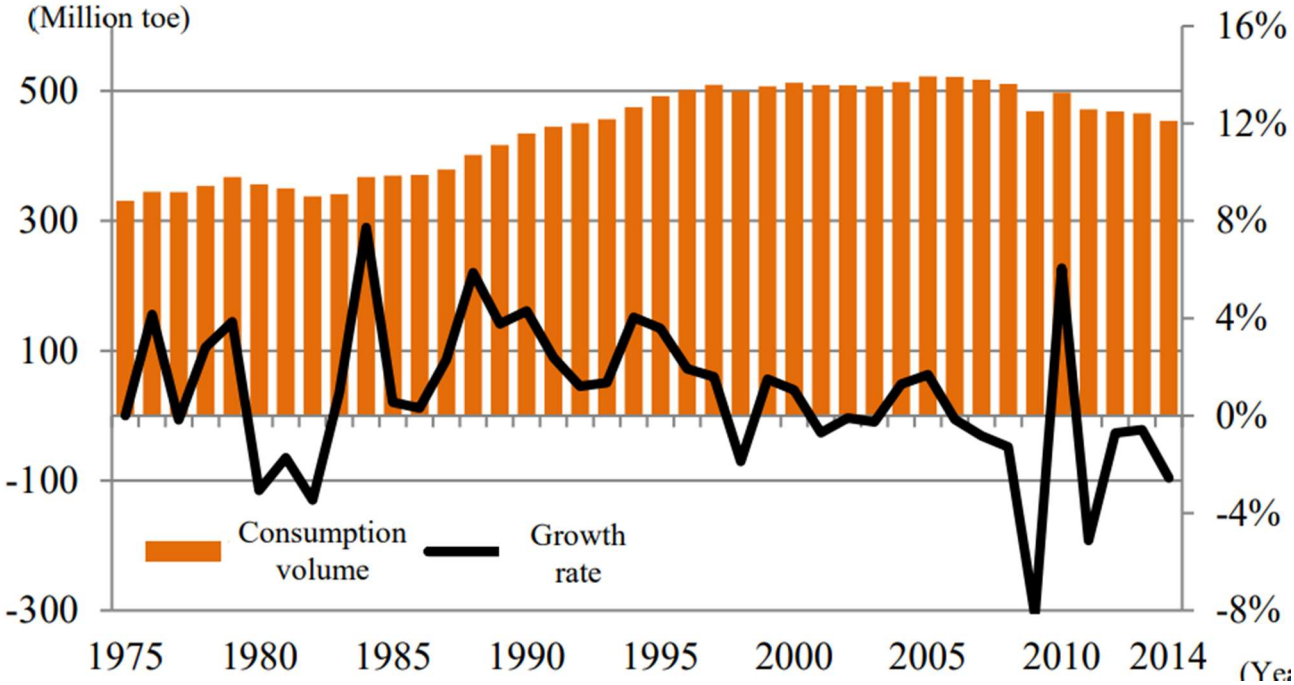

Figure 1.3: Changes in the energy consumption volume in Japan. adopted from Ref. [3].

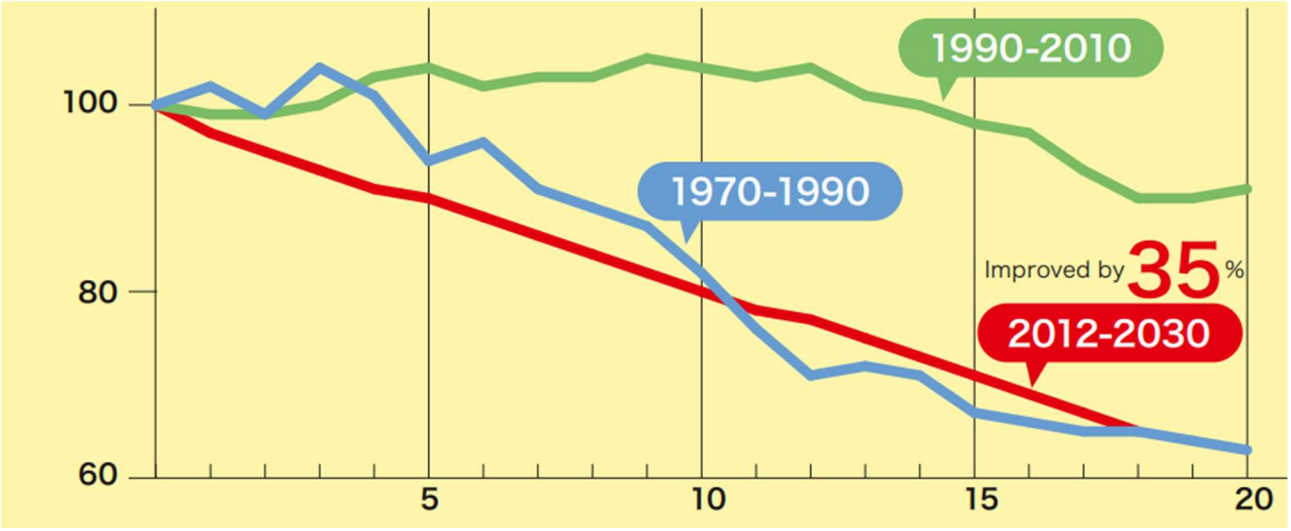

Figure 1.4: Improvement of Energy Consumption Efficiency intensity in Japan. Taken from Ref. [3].

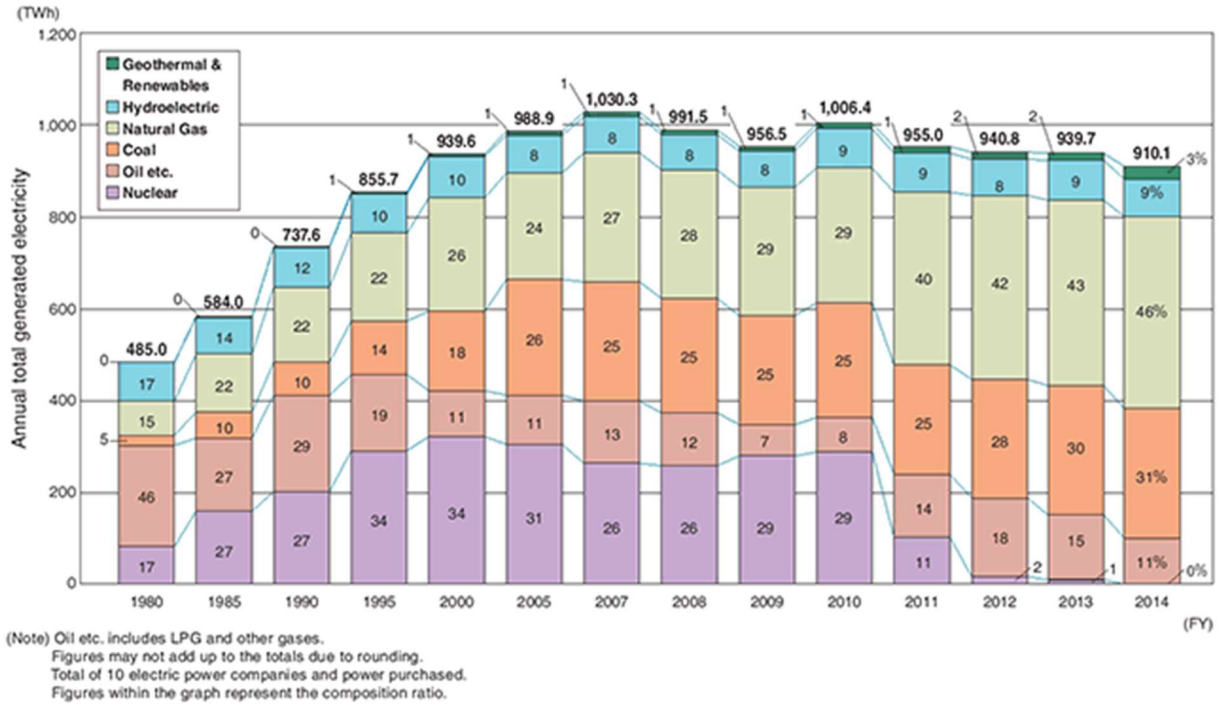

Figure 1.5: Historical trend of power generation volume by source in Japan. Taken from Ref. [4].

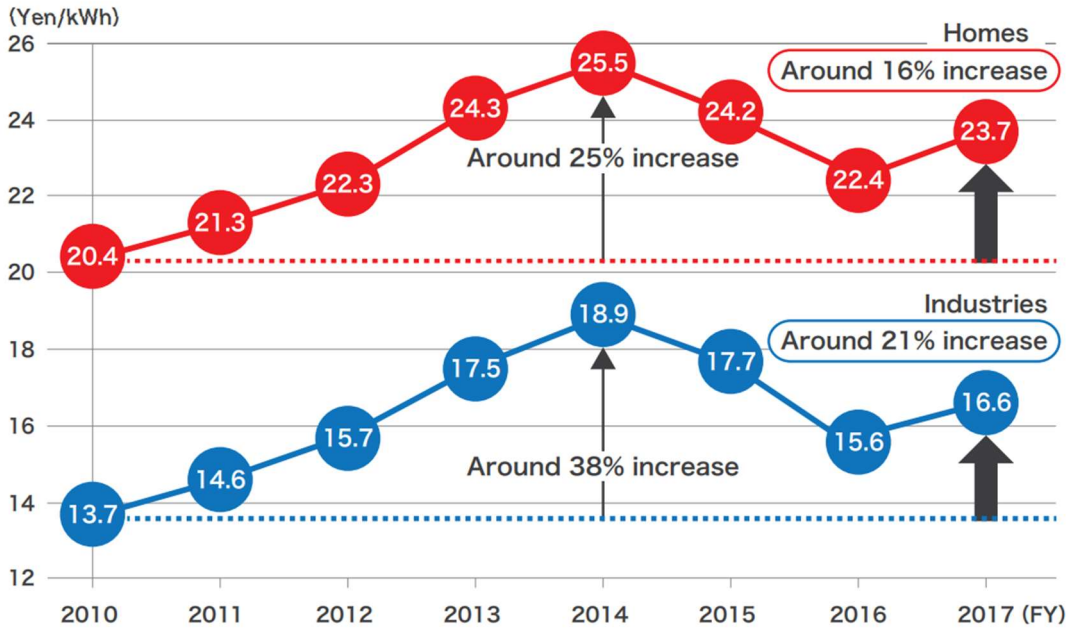

Figure 1.6: Changes in average electricity rate. Taken from Ref. [2].

1.3 Current status of renewable energy in Japan

Renewable energy is an important energy source for Japan, as it does not emit CO2 during power generation and contributes to improving the energy self-sufficiency rate [5]. Globally, the introduction of renewable energy into the power sector has led to a reduction in the Lelvlized Cost of Electricity, as Figure 1.7 shows [1].

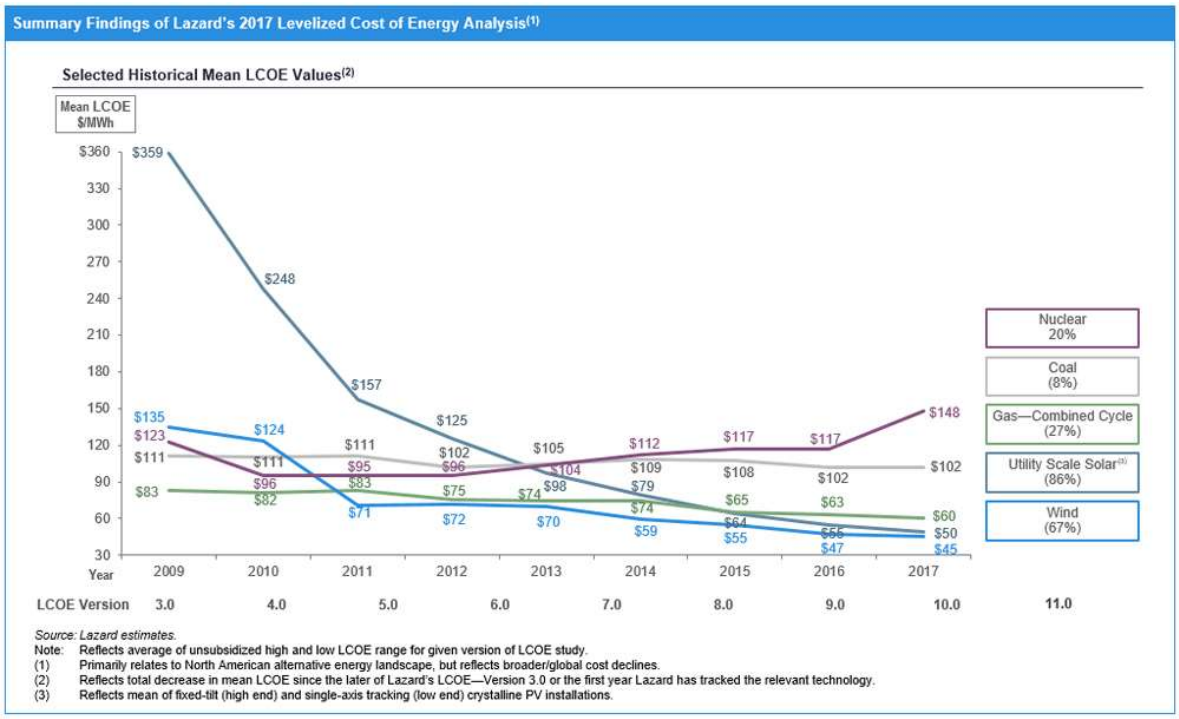

Figure 1.7: Levelized cost trends [6]

The introduction of the feed-in tariff (FIT) in Japan has led to a rapid deployment of renewable energy sources as shown in Figure 1.8. Fixed price purchase system (FIT) is a system in which electricity companies purchase electricity generated by renewable energy at a fixed price for a certain period [2].

On the other hand, renewable energy generation costs remain high compared to the other countries. As shown in Figure 1.9, the purchase cost in FY2017 reached to 2.7 trillion yen [2], and the levy burden for standard households was 686 yen/month. Besides, due to an increase in the installed capacity of renewable energy, the Japan power sector faced the burden of limited capacity.

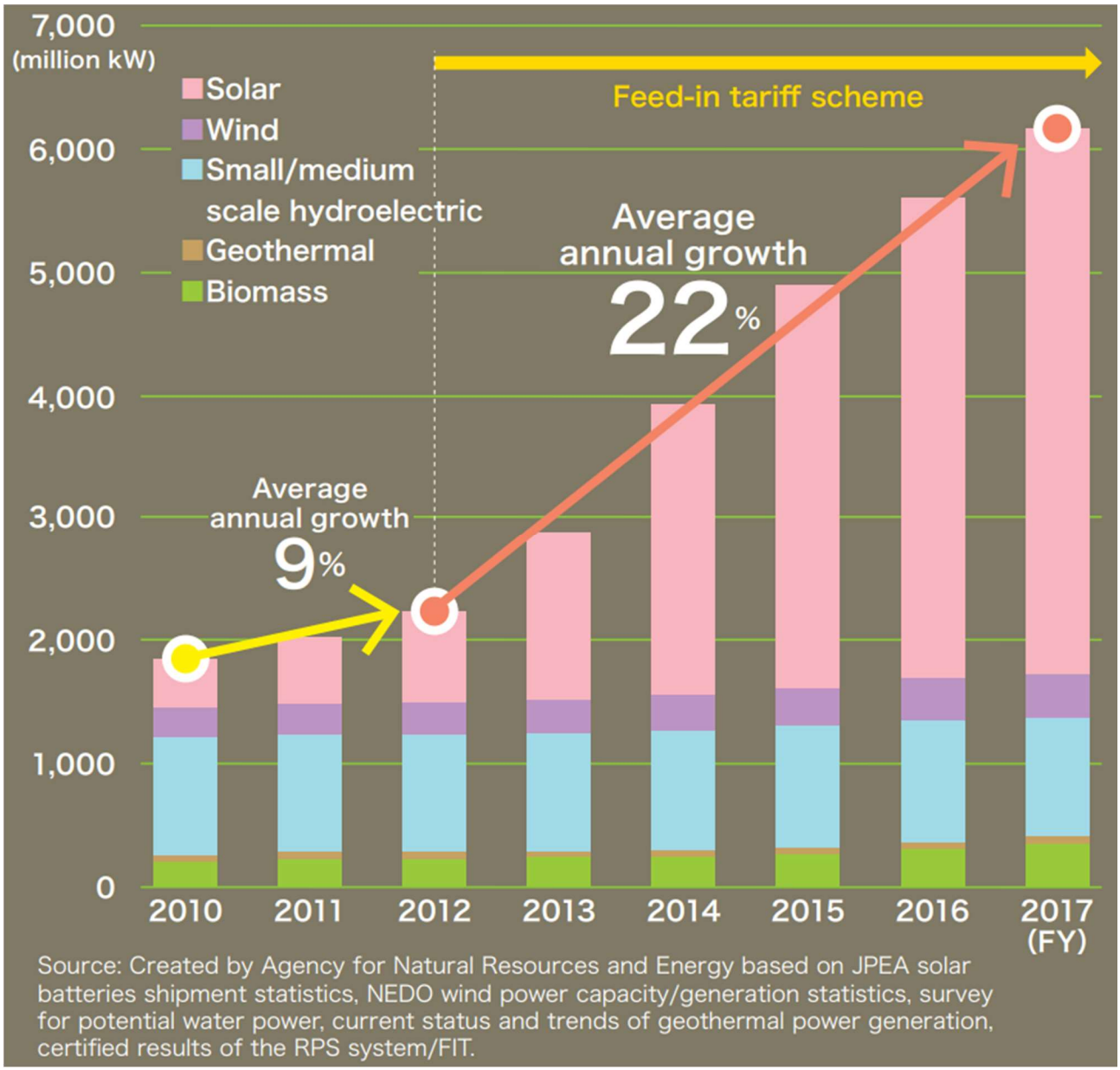

Figure 1.8: Changes in installed capacity resulting from renewable energy and other factors

Two examples include the massive blackouts due to the heavy rain in western Japan in July 2018 and the Eastern Hokkaido Iburi earthquake in September 2018. Solar power has been widely adopted in Kyushu which has prompted worries that Kyushu Electric Power Co may impose the temporary feed-in restrictions. Therefore, with the government looking to boost renewable power generation as a pillar of Japan's energy policy, the Kyushu situation highlights the urgent need to improve the country's

electricity transmission network. In response to this problem, Kyushu Electric Power Co applied output control to some solar power generators in FY2018 which is shown in Figure 1.10. This restriction can occur when power demand is low and solar power generation is high, such as in the autumn, spring or at the year-end and beginning of the year.

The establishment of a new schemes that can make profits from renewable energy projects, except the FIT scheme, is being now considered by the Japan government. Accordingly, the government plans to halt the FIT mechanism from November 2019. It is believed that, various renewable energy utilization models can be developed in Japanese housing such as efficient self-consumption combining residential solar and energy storage technologies, and effective use of surplus electricity in the home using grids and storage batteries.

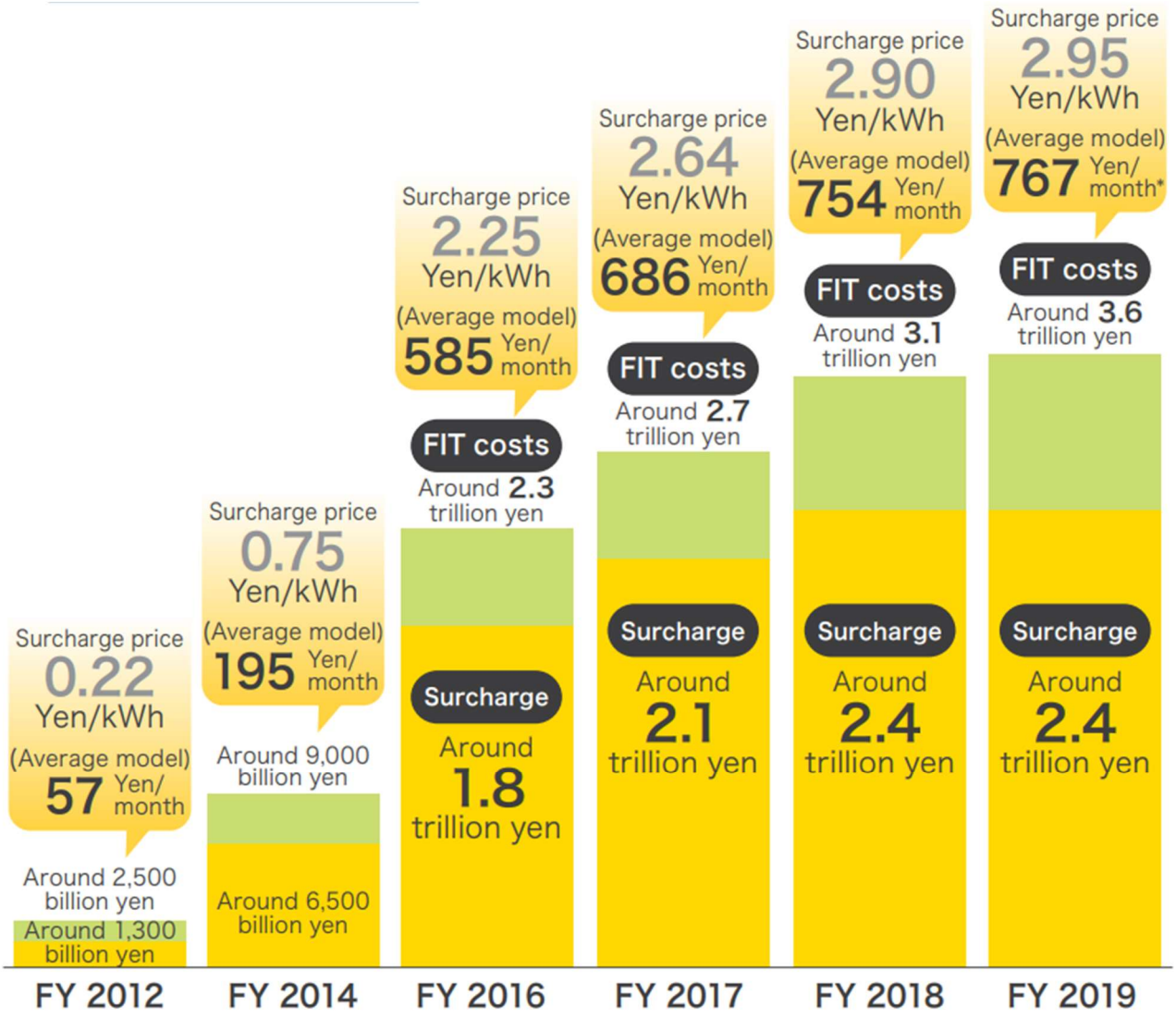

Figure 1.9: Trends in Surcharge after Introducing the FIT [2]

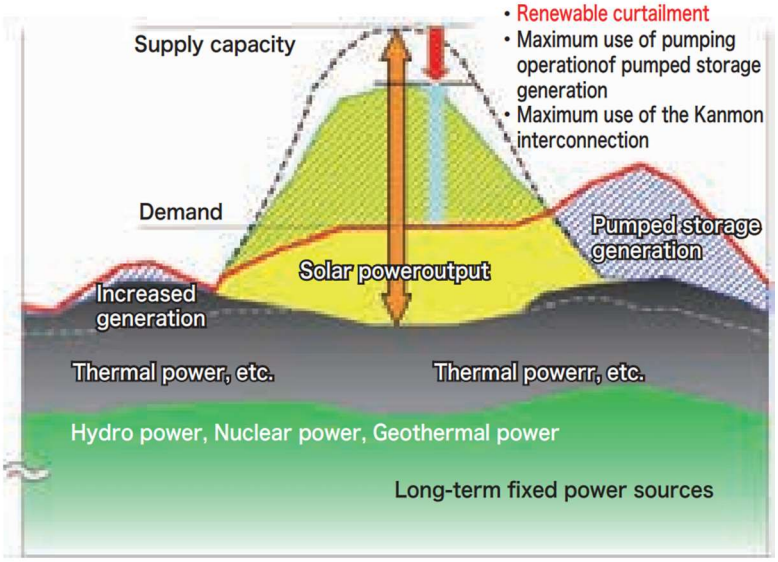

Figure 1.10: Renewable energy output restriction in mainland Kyushu [2]

1.4 Next-generation power network in Japan

Japan's electric power industry faces a wide range of challenges, including the restart of nuclear power plants, further improvement of environmental friendliness, and growing market competition. Initiatives are underway to decentralize power sector in Japan from the centralized fossil-based systems to the distributed ones (See Figure 1.11). There are three important steps which should be taken into consideration, here:

1. Maximizing the utilization of renewable energies
2. Adopting the Information Technology to increase the predictability of the electricity demand
3. Reforming the existing electricity network

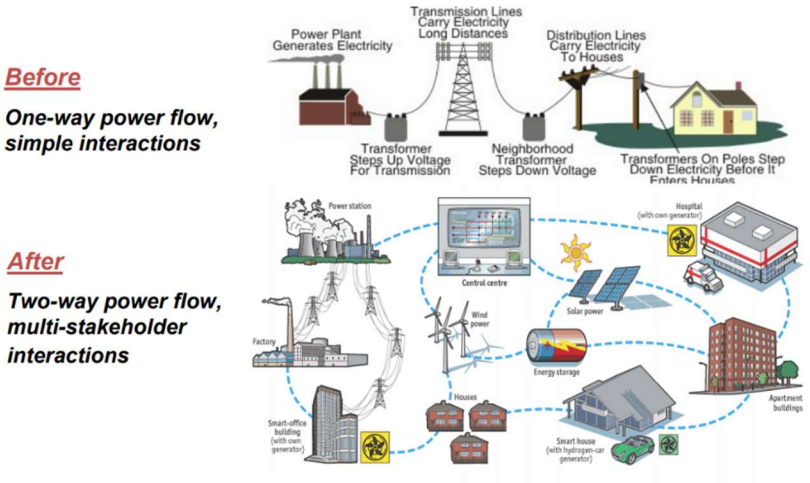

Figure 1.11: The Evolution of the Electric Utility System [6]

The amount of power generated by renewable energy sources such as solar power generation and wind power generation varies depending on the natural environment such as weather and sunshine conditions. Therefore, if the power generation from renewable energy sources exceeds, it is necessary to control the amount of power generated to maintain a stable supply of electricity.

1.5 Microgrid

The conventional Japanese power system is shown in Figure 1.11: The Evolution of the Electric Utility System [6] has many drawbacks because it is vulnerable to disasters due to extreme concentration. These systems can cause blackouts as described previously. One way to avoid this problem is to use Distributed Energy Resources (DER). DER enables the decentralization of power generation and storage. The deployment of DER involves both generators and energy storage technologies. The power generation facility is called a distributed generator (DG). A controllable subsystem that generates power from distributed energy resources (DER) can be considered a microgrid. A microgrid is a power system that combines various energy sources in the best possible way, through utilizing green energy. The microgrid can be connected to or disconnected from the utility grid depending on the local load. There are many types of DG. Some of them include the traditional internal combustion engine (IC) engines such as gas and other types utilize renewable and green energy sources such as solar energy, wind energy or hydrogen. Microgrids have several advantages, including reduced maintenance costs, emissions, and increased reliability and flexibility. However, the initial investment costs are high and needs to be reduced though finding the optimal configuration of the system in a cost-effectiveness way. To this aim, optimization of the residential microgrid system is considered as the main focal point of the recent research activities. Research that demonstrates the importance of optimizing microgrid systems with hybrid power supplies has gained more attentions from scholars word-wide (See Figure 1.12). As shown in this, HRES is a system that uses a combination of a renewable energy source such as a diesel generator, solar power (PV) or wind generator (WG), and a power storage system. HRES can provide cost- effective and reliable power, especially in remote areas where the installation of new transmission lines is expensive. Although renewable energy power sources such as solar and wind power depend on climatic conditions, it would be very difficult to predict the amount of power generated by a single renewable technology. This problem can be fixed in the HRES by combining two or more renewable energy sources that can compensate for each other's shortcomings. On the other hand, the system becomes complex and difficult to analyze. Therefore, a lot of research is being done to optimize the utilization of the HRES with a special focus on sizing, operation, and control of the output power [7,8].

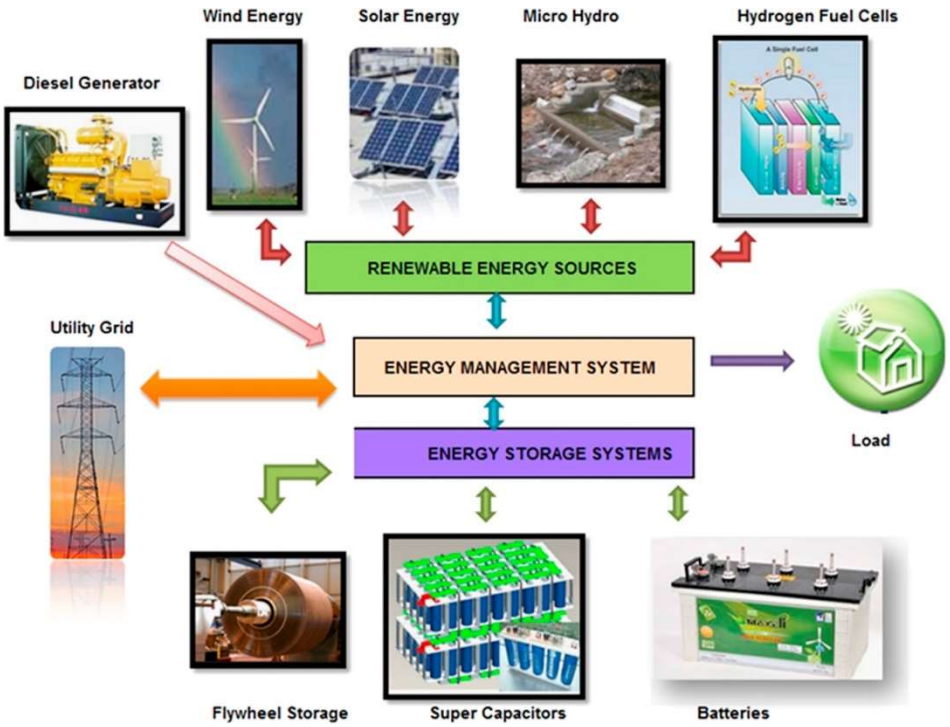

Figure 1.12: Hybrid renewable energy systems [9]

1.6 What will be elucidated in this research

This research introduces a novel optimization model based on the PSO method to find the optimal configuration of an autonomous renewable energy (RE) based microgrid system consists of solar panels, wind turbines, battery storage and diesel generators which is applied to a specific case study; a residential area in Kasuga-city in Japan (Figure 1.13). Each of the PV modules and wind turbines generate electricity from solar radiation and wind to meet the external load requirement. When the generated energy exceeds the demand load, the available surplus energy is stored in the battery. Moreover, if the battery is full, extra power is sent to a dummy load. If the amount of electricity generated by PV panels and wind turbines are less than the load requirement, the battery is discharged. If the battery's charge level is insufficient, then the diesel generator is used as a supplementary power source. The proposed research methodology aims at introducing a cost-effectiveness approach to find the optimal size of the system components, together with addressing the uncertainties related to the impact of variable weather conditions on overall performance of the proposed system and its optimal design.
As a detailed discussion later in Chapter 2, a comprehensive survey on microgrid optimization methods will be conducted. The details of the technical simulation and system componenets and configuration of the propsed microgrid will be discussed in Chapter3. Chapter 4 explains the optimization method which is based on the PSO algorithm proposed. The detailed method used in the weather forecasting model will be introduced in Chapter 5. The aforementioned model will be applied to a small community in the city of Kasuga, Fukuoka Prefecture, Japan to find the optimal configuration of the proposed microgrid system which can be used to meet the electricity demand in this area, finally, the conclusions and future research will be presented in Chapter 7.

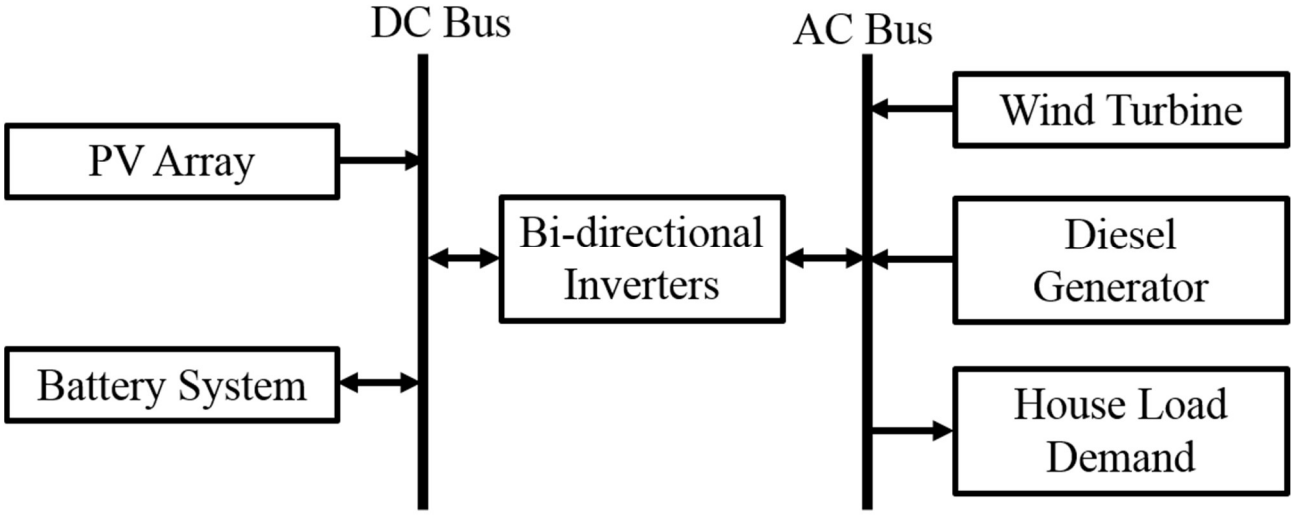

Figure 1.13: Autonomous renewable energy system in this study

Chapter 2

Problem description

In this chapter a comprehensive literature survey on past investigations which were conducted on modeling and simulation of the Microgrid systems will be given as follows:

2.1 Literature survey

Many scholars have developed optimization techniques to find the optimal operating point and configurations of microgrid systems and HRES. The main methods include minimizing of the total cost and emissions or maximizing reliability of the system. Besides, optimization methods can be classified into the single objective (SO) and multi-objective optimization problems (MOP), and there are still very few studies using MOP.

2.2 Microgrid optimization

Table 2.1 shows the classification of the different optimization methods used in the microgrids based on the optimization approach and selected objective function.

The autonomous Renewable Energy (RE) -based microgrid systems are considered as the most appropriate and cost-effective ways to electrify off-grid communities [10]. Since isolated off-grid systems cannot be connected to the grid, matching the quantity of the supplied electricity with the load requirement is an important issue. Also, isolated systems require to use multiple energy sources for supplying reliable power. Therefore, hybrid renewable energy systems are particularly suitable to be used in the small communities [11]. However, the integration of multiple energy sources into the microgrid system increases the complexity of the system. Power generation in residential community microgrid can use different Renewable Energy Resources (RERs) such as solar and wind. Therefore, in the event of a power failure, it can work as an autonomous hybrid power system that can operate disconnected from the utility grid. Photovoltaic (PV) and wind power (WG) units are the most promising technologies for supplying loads in remote and rural areas.

Table 2.1 Literature survay

Authors	Year	System components							Objective function	Optimization approach	Model period
		Wind turbine	PV	FC	Biomass	Hydro power	Storage	Diesel & other			
Zhang et al.[8]	2019	●	●	●		●		●	Minimizes total cost	CS-HS-SA-ANN	20 years
Bukar et al. [10]	2019	●	●				●	●	Minimizes total cost	GOA	1 year
Lu et al. [12]	2015	●	●					●	SOP (Minimizes cost or CO2) &MOP	NSGA-II	1 year
Sharafi et al. [13]	2014	●	●	●			●	●	MOP (Minimizes cost and CO2)	PSO	1 year
Kuzunia et al. [14]	2013	●					●	●	Minimizes total cost	SMIP	1 year
Khatib et al. [15]	2012	●	●				●		Minimizes total cost	GA	1 year
Ahmarinezhad et al. [16]	2012	●	●	●	●		●	●	Minimizes total cost	PSO	20 years
Garyfallos et al.[17]	2010	●	●	●			●	●	Minimizes total cost	SA	10 year
Kashefi et al. [18]	2009	●	●	●			●		Minimizes annualized cost	PSO	20 years
Cai et al. [19]	2009	●	●			●		●	Minimizes total cost	ISITSP	15 years
Lagorse et al. [20]	2008		●	●			●	●	Minimizes total cost	Simulation	1 year
Dufo-Lo´pez et al. [21]	2007	●	●	●		●	●	●	Minimizes total cost	GA	1 day
Raquel et al. [22]	2006	●		●			●	●	Minimizes the LEC	LP + heuristic	1 year
Koutroulis et al. [23]	2006	●	●						Minimizes total cost	GA	20 years

However, they use unpredictable renewable energy sources which raise concerns about the reliability of power system. Oversizing is an approach that overcomes reliability problems, but it a cost-intensive approach[18]. Application of the Hybrid PV / WG systems are more reliable with lower system costs compared to a single wind or solar power system[15,23]. Besides, the increasing penetration of RER through intermittent power generation causes greater technical challenges to maintain the balance between the power supply and demand in the power system. To this end, diesel generators and energy storage systems are widely used as backup power sources to cover supply and demand discrepancies and improve the stability of micro- grid systems. Renewable energy technologies such as solar and wind power systems usually require more investment costs, but their operating costs are almost negligible compared to fossil-based systems like diesel generators. Nevertheless, Diesel also plays an important role in ensuring the regulation and control of the necessary systems [11]. However, the main drawback of using diesel generators in microgrid systems is the cost and environmental impact of burning fossil fuels such as light oil, kerosene, and fuel oil. Furthermore, energy storage systems are generally expensive, and implementing large energy storage systems can be a heavy burden on consumers. Therefore, it is important to investigate the total cost minimization approach to find the optimal size of the components, specially the storage systems used in the Microgrids. Since the optimal design of HRES is a complex task, a meta heuristic optimization modeling approach would be needed rather than the traditional optimization methods [21].

Particle swarm optimization (PSO) which is based on swarm intelligence approach is one of the meta heuristic approaches that can be used to solve complex problems. Compared to other meta heuristic algorithms, PSO is simpler and easier to be implemented and requires fewer parameters. Optimization techniques require an explicit mathematical representation of the system. Sharafi et al. studied a case study for the HRES system including wind turbines, photo voltaic (PV) panels, diesel generators, batteries, fuel cells (FC), electrolyzers, and hydrogen tanks, using PSO [13]. Garyfallos et al. has developed an optimization model based on a stochastic simulated annealing algorithm which was used to find the minimum net present value of the 10-year cost for designing power generation systems which was comprised of solar panels, wind power generators, storage of batteries, electrolyzers, storage tanks, compressors, fuel cells, and diesel generators, considering the effects of weather conditions [17]. Kuzunia et al. developed a stochastic mixed-integer programming model based on the PSO method for the comprehensive hybrid power system design problems, including renewable energy generation, storage, grids, and thermal generators for remote locations and explained how the application of the PSO will help to find the optimal design of the system [14]. Kuzunia et al. developed a comprehensive hybrid system configuration problem was modeled by a stochastic integer program and solved for the first time by an efficient algorithm. Ahmarinezhad et al. optimized a wind / PV hybrid system with battery and diesel backup optimized by PSO. This stand-alone system is optimized with actual wind speed data, PV arrays, and defined area load profiles. This study reveals that applying an optimized system to a specific area is very cost-effective. Also, through the optimization of hybrid power generation systems, the demand for using diesel generators in addition to renewable energy has been implemented efficiently and economically. Kaviani et al. used PSO to minimize the annual operating cost of a hybrid wind/solar/fuel cell power system with a 20-year operation period [18]. Raquel et al.[22] developed a linear programming model as a benchmark to find the optimal control strategy of a wind-diesel systems coupled with a hydrogen storage and clarified the role of control policy in minimizing the total cost of the hybrid system. Koutroulis et al. [23] and Khatib et al.[15] introduced a genetic algorithm-based model to explore the optimal configuration of a hybrid PV / WG system though minimizing the total system cost of the system over its life span. Dufo-López et al. presented a new strategy for controlling a stand-alone hybrid renewable electrical system with hydrogen storage, using genetic algorithms.

Although RER address the need for the sustainable energy systems, its inherent variability and reliance on weather conditions can add an extra complexity to the power network. Craparo et al. introduced an ensemble weather forecast system to predict the optimal performance of the virtual grid, including wind turbines, intending to minimize cost and power loss, while taking into account the uncertainty of

system output. Precise prediction of the weather condition reduces the need for the required backup power systems such as diesel and battery storages, which is typically available at higher cost[24]. Neves et al. also investigated the impact of weather forecasting on-demand response performance of isolated microgrid [11]. Salcedo-Sanz et al.[25] showed that the hybrid MM5 neural network approach can be used to obtain a good short-term prediction of wind speed at a specific area. Several wind forecasting models which can be in a microgrid system are addressed by Soman et al.[26]. Junior et al. predicted local hourly solar electricity generation in four major areas in Japan from using the basic weather forecast data [27]. In Germany, advanced solar power forecasting systems have already been developed which use solar weather forecasting data from the European Medium-Term Weather Forecast Center (ECMWF). Therefore, it is possible to predict the hourly horizontal solar radiation based on the location of the PV system [27]. Similarly, in 2017, JMA launched the solar radiation forecast data in Japan [28]. The GPV-MSM weather forecasting system provided by JMA (Japan Meteorological Agency) [29] reproduces atmospheric phenomena using non-wet mesoscale modeling. The system provides weather forecasts with a spatial resolution of 5 km2. Hourly forecasts of the seven weather-related variable data on surface are provided 8 times a day (00:00, 03:00, 06:00, 09:00, 12:00, 15:00, 18:00, 21:00 in UTC time zone). The forecast period is up to 39 hours or 51 hours ahead, depending on the forecast time [30].

Batteries have become an important part of the HRES [31,32]. One of the most important uncertainties in designing a HRES is the state of charge (SOC) of the battery storage during the day-night. So, prediction one day ahead of the battery's SOC in a HRES has already been considered in assessing the uncertainty of the system by many scholars [33].

2.3 Research Methodology

As it was explained previously, the main goal of this thesis is to find the optimal design of a proposed stand-alone microgrid which is supposed to be used in a small community in Kasuga city. The research Steps are shown in Figure 2.1.

Figure 2.2 represents the methodological approach which is used in this research. The simulation part is developed to estimate the electrical power generated by each component, taking into account the variation of the weather parameters such as wind, solar irradiation and ambient temperature. The optimal system design is then founded by using a PSO algorithm which uses populations to search for promising areas in the search space [34]. Design variables, the capacity of each component, are defined as vectors which are called particles. The total cost of the system, which is considered as the objective function of the optimization part, is taken as the fitness function of the particles for particle evaluation. In this context, the population is called a flock and individuals are called particles. Each particle moves in an adaptable speed in the search space and keeps the highest position it has encountered in the past. The global solution of the PSO model, the best position that every individual in the flock has ever achieved, is adopted to all particles [35]. After randomly creating particles, the value of each particle is calculated in the simulation model and the performance of each particle is evaluated from the simulation results. After initializing the viable particles, they use the PSO algorithm to search for the optimal component composition based on the minimum cost of the system.

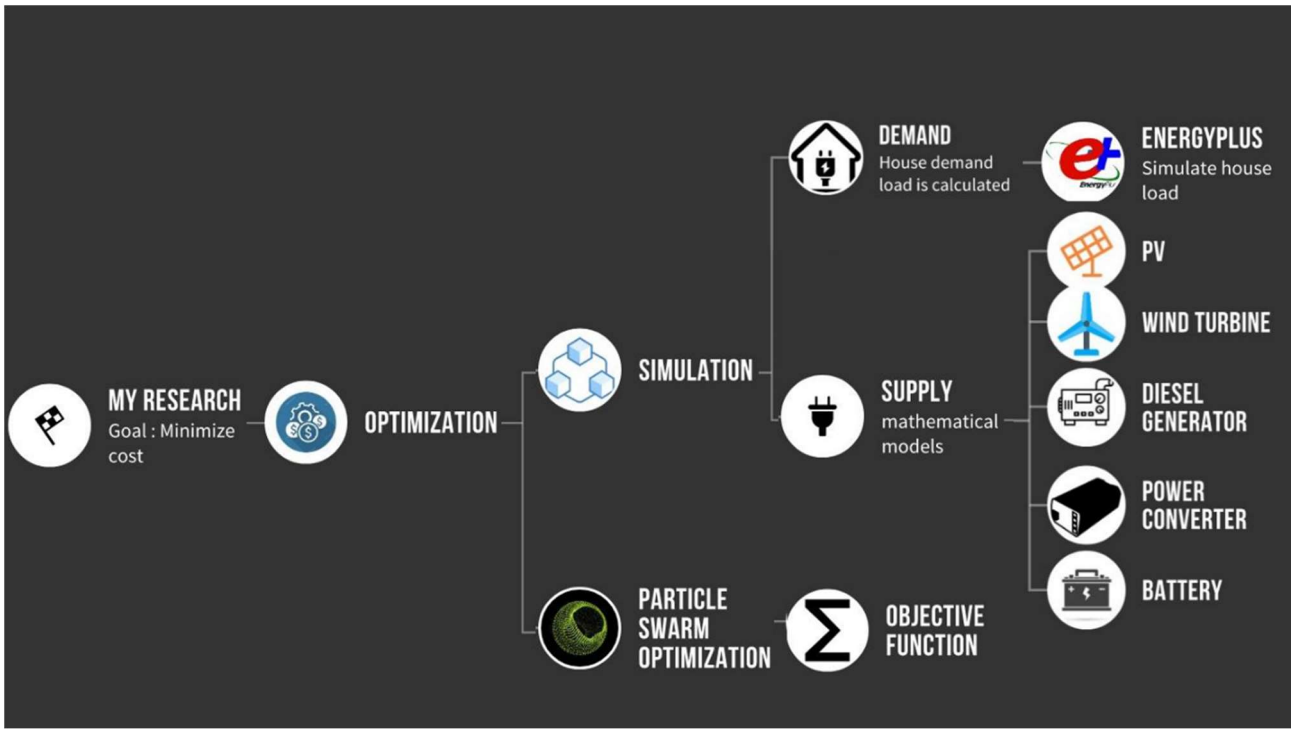

Figure 2.1: Research methodology in this study

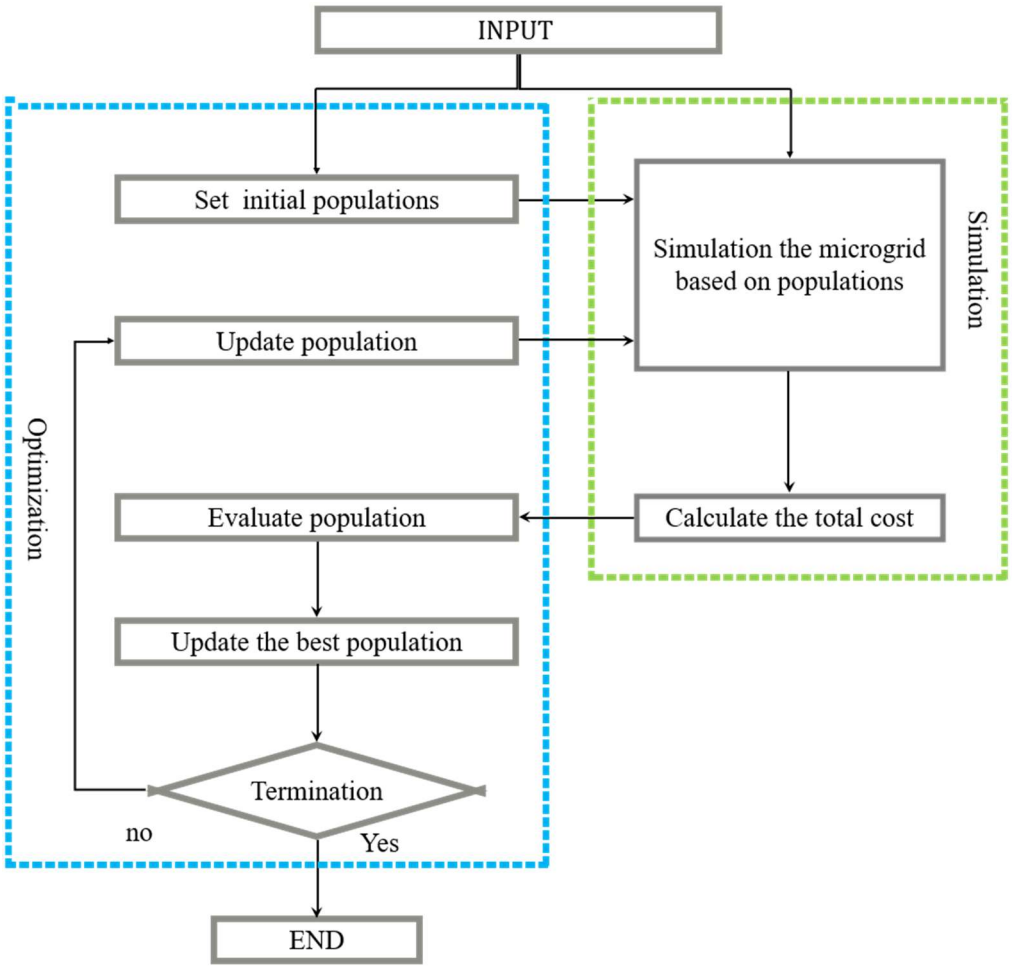

Figure 2.2: Overall modeling approach used in this study

Chapter 3

Simulation model

3.1 Wind power generation

Wind turbine converts wind energy into electrical energy. Compared to Europe and the United States, the installed capacity of wind power generation in Japan is limited, but since 2000, the number of installations has increased gradually[36]. The amount of power output of a wind turbine is directly proportional to the wind speed, which can be calculated using the following equations :

$$P_{wt}(V) = \begin{cases} \dfrac{P_r(V - V_{CIN})}{V_{rat} - V_{CIN}}, & V_{CIN} \le V \le V_{rat} \\ P_r, & V_{rat} \le V \le V_{CO} \\ 0, & V \le V_{CIN}\ and\ V \ge V_{CO} \end{cases} \quad (1)$$

$$V = V_{ref}\left(\frac{H}{H_{ref}}\right)^{\alpha} \quad (2)$$

Where, V_{ref} is the wind speed measured at the reference height, H_{ref}. α is the power-law exponent. V refers to the wind speed at the height of H is the wind speed measured at the reference height, H_{ref}, and α which is the power-law exponent.

$$P_w = \frac{\rho}{\rho_0} P_w(STP) \quad (3)$$

where, $P_w(STP)$ is the wind turbine power output at standard temperature and pressure [kW]. ρ shows actual air density [kg/m3]. ρ_0 is defined "the air density at standard temperature and pressure (1.225 kg/m3).

3.2 Solar Photovoltaic (PV) power generation

Solar electricity is the Japan's leading renewable technology. The installed capacity of the solar power in Japan has steadily been increased in recent years, reaching to a total of 39.1 millions kW in 2016. PV uses the phenomenon that electricity is generated when light hits a silicon semiconductor[36].

In this study, the following equations from Duffie and Beckman (1991) [37] was used to calculate the hourly power generation from a solar panel.

The calculation can be divided into three major steps [38].

- Calculation of PV cell temperature
- Calculation of the Radiation Incident on the PV Array
- Calculation of the Radiation Incident on the PV Array

The orientation of a PV array can be described by using two parameters of tilt and azimuth angles. The PV slope is the angle between the surface of the panel and the horizontal plane, so a zero slope indicates a horizontal direction, while a 90 ◦ slope indicates a vertical direction. Azimuth is the direction in which the surface is facing to it. As for the reference of azimuth, zero azimuth corresponds to true south, and a positive value points westward. Thus, an azimuth of -45 ◦ is southeast, and an azimuth of 90 ◦ is west. Other factors related to the geometry of the situation are latitude and time. The time of the year affects the declination of the sun. It is the latitude at which the rays of the sun are perpendicular to the surface of the earth at noon of the sun. The declination of the sun is calculated using the following formula.

$$\delta=23.45° \sin\left(360° \frac{284+n}{365}\right) \tag{4}$$

$$n = the\ day\ of\ the\ year\ [\ a\ number\ 1\ through\ 365\ days] \tag{5}$$

Time affects the position of the sun in the sky. It can be expressed as an angle of one hour, considering that the angle is zero at noon time (the time when the sun is at the highest point of the sky). The time angle can be calculated by using the following formula :

$$\omega=(t_s\text{-}12hr)\times 15°/hour \tag{6}$$

$$t_s=\text{the solar time[hour]} \tag{7}$$

The value of t_s *is* 12 hours at noon and 13.5 hours after 90 minutes. The above equation is based on the fact that the sun moves across the sky at 15 degrees per hour. The angle of incidence for surfaces of any orientation can be defined as the angle between the sun's beam radiation and the surface normal using the following equation:

$$\begin{aligned} cos\theta = {} & sin\delta sin\phi cos\beta - sin\delta cos\phi sin\beta cos\gamma + cos\delta cos\phi cos\beta cos\omega \\ & + cos\delta sin\phi sin\beta cos\gamma cos\omega + cos\delta sin\beta sin\gamma sin\omega \end{aligned} \tag{8}$$

A particularly important angle of incidence is the zenith angle, which shows the angle between the vertical line and the line to the sun. The zenith angle is zero when the sun is directly above and 90 ° when the sun is at the horizon. Then, the zenith angle can be calculated based on the following equation:

$$cos\theta_z = cos\phi cos\delta cos\omega + sin\phi sin\delta \tag{9}$$

$$\theta_z = the\ zenith\ angle[°] \tag{10}$$

To calculate the extraterrestrial normal radiation, defined as the amount of solar radiation striking a surface normal (perpendicular) to the sun's rays at the top of the earth's atmosphere, the following equation is used.

$$G_{on} = G_{sc}\left(1 + 0.033 \cdot cos\frac{360n}{365}\right) \tag{11}$$

To calculate extraterrestrial horizontal radiation, which is defined as the amount of solar radiation that hits the horizontal plane at the top of the atmosphere, the following equation is used :

$$\overline{G_o} = \frac{12}{\pi} G_{on}\left[cos\phi cos\delta(sin\omega_2 - sin\omega_1) + \frac{\pi(\omega_2 - \omega_1)}{180} sin\phi sin\delta\right] \tag{12}$$

The ratio of the surface radiation to the extraterrestrial radiation is called the clearness index. The following equation defines k_T (clearness index) :

$$k_T = \frac{\overline{G}}{\overline{G_o}} \tag{13}$$

The total of beam and diffuse radiations is called global solar radiation and is expressed by the following equation :

$$\overline{G} = \overline{G_b} + \overline{G_d} \tag{14}$$

The difference between beam and diffuse radiation is important when calculating the amount of incidents radiation on the inclined surface. It is necessary to resolve global horizontal radiation into its beam component and diffuse component to find the radiation incident on the PV array. In this research the correlation defined by Erbs et al. (1982) was used to find the diffuse fraction as a function of the transparency index :

$$\frac{\overline{G_d}}{\overline{G}} = \begin{cases} 0.165 & for\ k_T \leq 0.22 \\ 0.9511 - 0.1604k_T + 4.388k_T^2 - 16.638k_T^3 + 12.336k_T^4 & for\ 0.2 < k_T \leq 0.802 \\ 0.165 & for\ k_T > 0.80 \end{cases} \tag{15}$$

At each time step, the clearness index and the diffuse radiation are calculated by using the average global horizontal radiation. It then calculates the beam radiation by subtracting the diffuse radiation from the global horizontal radiation. To calculate the global radiation striking the tilted surface of the PV array, the HDKR model was used, which assumes that there are three components to the diffuse solar radiation :

- An isotropic component that comes from all parts of the sky equally
- A circumsolar component that emanates from the direction of the sun
- A horizon brightening component that emanates from the horizon.

Before applying this model, we must first define these three factors. The following equation defines R_b, the ratio of beam radiation on the tilted surface to beam radiation on the horizontal surface.

$$R_b = \frac{cos\theta}{cos\theta_z} \tag{16}$$

$$A_i = \frac{\overline{G_b}}{\overline{G_o}} \tag{17}$$

Finally, we need to define a factor which is considered for horizon brightening or the fact that more diffuse radiation comes from the horizon than from the rest of the sky. This term is related to the cloudiness and is given by the following equation :

$$f = \sqrt{\frac{\overline{G_b}}{\overline{G}}} \tag{18}$$

The HDKR model calculates the global radiation incident on the PV array according to the following equation :

$$\overline{G_T} = (\overline{G_b} + \overline{G_d}A_i)R_b + \overline{G_d}(1 - A_i)\left(\frac{1 + cos\beta}{2}\right)\left[1 + fsin^3\left(\frac{\beta}{2}\right)\right] + \overline{G}\rho_g\left(\frac{1 - cos\beta}{2}\right) \tag{19}$$

Photovoltaic (PV) cell temperature is the temperature of the surface of the PV array. At night, the ambient temperature is the same as the array, but when the sun hits the cell, the surface temperature may exceed the ambient temperature by more than 30 ◦ C. The overall energy balance of a PV array is given by the following equation, using the Duffie and Beckman principle (1991) [37]:

$$\tau\alpha G_T = \eta_c G_T + U_L(T_c - T_a) \tag{20}$$

where, $\tau\alpha$ is the effective transmittance-absorptance of the PV panel [39]. η_c equals to electrical conversion efficiency of the PV array [%]. U_L is overall heat transfer coefficient of the PV [kW/m^2°C]. T_C and Ta are PV cell temperature [◦C] and Ambient temperature [◦C]. The equation above states that a balance exists between the solar energy absorbed by the PV array, and the amount of electrical output and heat which is transfer to the surroundings. The cell temperature is given by the following formula :

$$T_c = T_a + G_T\left(\frac{\tau\alpha}{U_L}\right)\left(1 - \frac{\eta_c}{\tau\alpha}\right) \tag{21}$$

It is difficult to measure the value of ($\tau\alpha/U_L$) directly. Instead, the manufacturer reports the nominal operating cell temperature (NOCT) which is defined as the cell temperature at incident radiation of 0.8 kW/m^2, an ambient temperature of 20◦C, and no-load operation (meaning ηc = 0). Substituting these values into the above equation and solving for $\tau\alpha/U_L$, the following formula can be obtained :

$$\frac{\tau\alpha}{U_L} = \frac{T_{c,NOCT} - T_{a,NOCT}}{G_{T,NOCT}} \tag{22}$$

Assuming that $\tau\alpha/U_L$ is constant, this equation is substituted into the equation (20) to calculate T_c.

$$T_c = T_a + G_T\left(\frac{T_{c,NOCT} - T_{a,NOCT}}{G_{T,NOCT}}\right)\left(1 - \frac{\eta_c}{\tau\alpha}\right) \tag{23}$$

Finally, the output of the PV array is calculated by the following equation.

$$P_{pv} = G_{pv} f_{pv}\left(\frac{I_T}{I_{T,STC}}\right)\left[1 + \alpha_p\left(T_C - T_{C,STC}\right)\right] \tag{24}$$

3.3 Diesel Generator

The diesel generator will be used as the backup system in the proposed microgrid system. The diesel generators supplies electricity by converting the chemical energy stored in diesel fuel into electricity [40]. The fuel consumption of a diesel generator is calculated as follows [41]:

$$Cons_G = A_G \cdot P_{N\_G} + B_G \cdot P_G(t) \tag{25}$$

Where, $Cons_G$ is fuel consumption of diesel generator[L/h]. P_{N_G} is nominal power of diesel generator[kW]. P_G is power output of diesel generator[kW]. A_G and B_G are fuel coefficient of diesel generator which is set 0.2461[L/kWh] and 0.081451[L/kWh] [13]. The thermal efficiency of the diesel generator is estimated by using the following equation :

$$\eta_G = \frac{P_G}{Cons_G} \tag{26}$$

3.4 Power converter

The proposed system utilizes a bi-directional converter to link the AC and DC buses to each other, as shown in Figure 1.13. The amount of the converted power by the converter is calculated by the following equation [42].

$$P_{conv} = P_L^{max}/\eta_{conv} \tag{27}$$

Where, P^{max} is peak load demand in the proposed system. η_{conv} is the efficiency which is set at 90%.

3.5 Battery Energy Storage Systems (BESS)

BESS is the most popular storage system which is currently used in the microgrids. BESS stores energy in form of charging the electro-chemical cell. The desired capacitance and voltage can be achieved by connecting them in series or parallel or both. There are four main types of batteries.

1. Lead-acid
2. Nickel-cadmium(Ni-Cd)
3. Sodium-sulphur(NaS)
4. Lithium-ion(Li-ion)

Lead-acid batteries are the cheapest one, but nickel-cadmium batteries have the highest energy density of 151 kWh / m3. Nickel-cadmium batteries have a relatively long cycle life and less environmental damage than nickel-metal hydride batteries. Lithium-ion batteries are the most expensive ones but have higher energy density. Therefore, the most suitable type is selected in accordance to the system requirement. Table 3.1 shows the life and efficiency of each type of BESS.

Table 3.1 Analysis of BESS technology[9]

Energy storage type	Lifetime	Cost in ($/kW h)	Efficiency (%)
Lead–acid battery	5-15 years	150-1300	75-90
Nickel–cadmium battery (Ni–Cd)	>3500 cycles	150-1300	90
Sodium–sulphur battery (NaS)	2000 cycles	450	85
Lithium-ion battery (Li-ion)	>3500 cycles	150-1300	85
Vanadium redox flow battery (VRB)	15-20 years	150-1300	75-85
Zinc–bromine flow battery (ZBB)	20 years	150-500	75-85
Polysulphide bromide battery (PSB)	>15 years	150-1300	75

The proposed microgrid system in this research uses lead-acid batteries. The state of charge (SOC) of a lead-acid battery system should be controlled within the following range.

$$SOC_{min} \leq SOC(t) \leq SOC_{max} \tag{28}$$

Where SOCmax is the upper limit, SOCmin equals to the lower limit of SOC. The state of charge of the battery at any time step can be calculated as given below [13]:

$$SOC(t) = SOC(t-1) \pm \frac{E_{bat}(t) \cdot \eta_{bat}}{P_{bat}} \cdot 100 \tag{29}$$

Where, η_{bat} is discharge and charging efficiency [%]. $E_{bat}(t)$ and P_{bat} are battery state of charge[kWh] and maximum battery capacity[kWh].

3.6 Control strategy

The control strategy flowchart of electricity generation and storage in the proposed microgrid system is represented in Figure 3.1. If the amount of the electricity generated by the wind turbine and PV panels exceeds the load requirement, the surplus energy is stored in the battery. If the *SOC* of the battery is reached to its maximum level and there is still excess electricity, the extra electricity will be sent to a dummy load. If the amount of renewable electricity generated by the solar panels and win turbine is less than the load requirement, then the battery storage can be discharge to meet the demand. If the battery discharge was insufficient, a diesel generator will be added to the system as a backup.

3.7 Demand load calculation

This section describes how to calculate general household load consumption which is explained by ASHRAE Standard 12-75 [43]. The main terms and units are identified as follows :

- Room : an enclosed or partitioned space
- Zone : a space or group of spaces within a building with heating or cooling
- British thermal unit (Btu) : the approximate heat required to raise 1 lb. of water 1 degree Fahrenheit
- Cooling Load Temperature Difference (CLTD) : the sensible cooling load due to heat gains through the walls, floor, and ceiling of each room
- Sensible Heat Gain : the energy added to space by conduction, convection or radiation
- Latent Heat Gain : The energy added to space due to moisture content of atmosphere
- Radiant Heat Gain : the rate at which heat is absorbed by the surfaces
- Space Heat Gain : the rate at which heat is gained by the space during a given time interval.
- Space Cooling Load : the rate at which thermal energy has to be removed from a space

Chapter 3 Simulation model

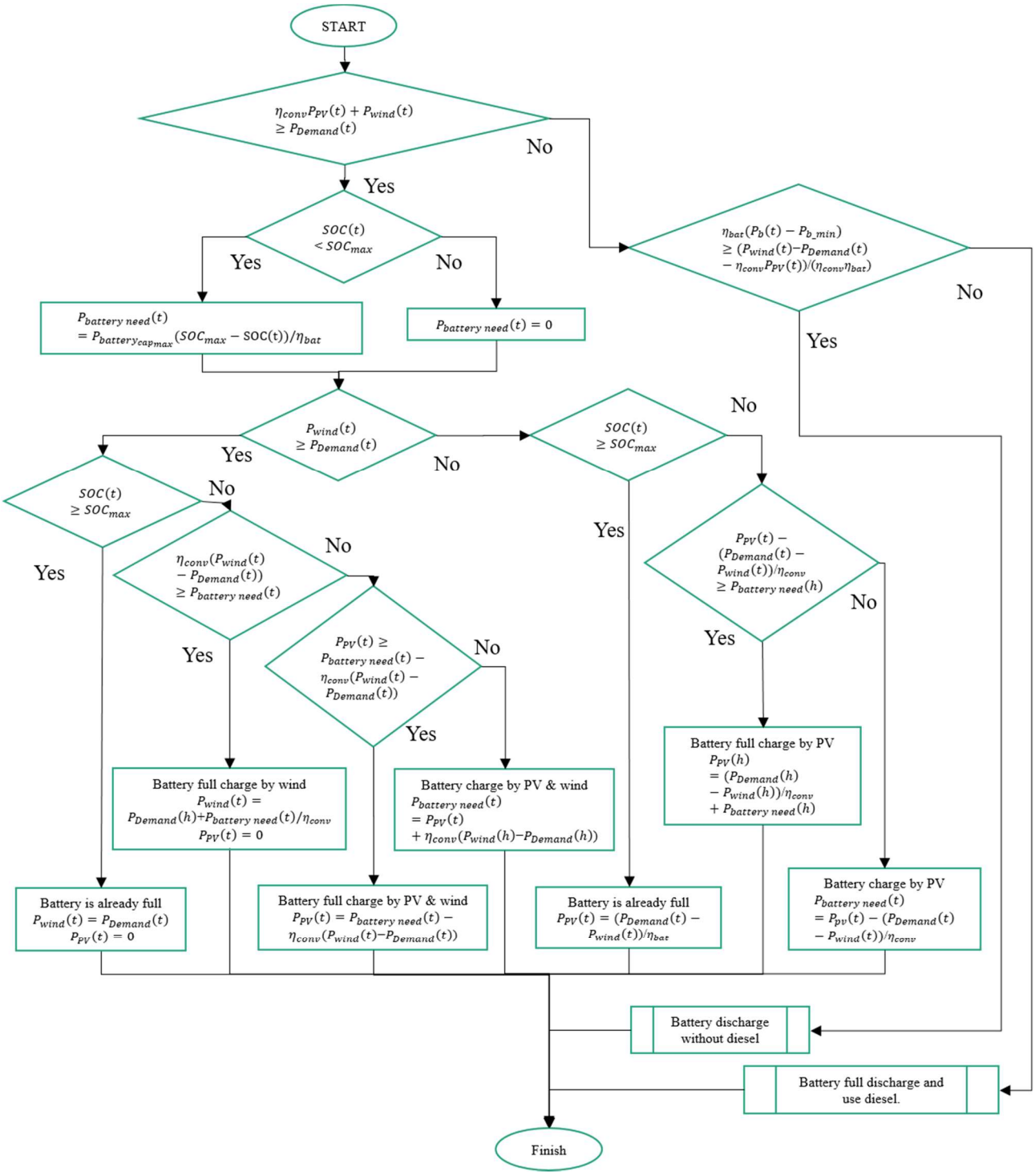

Figure 3.1: Dispatch strategy flowchart

Heating and cooling loads result from heat transfer processes through the building envelope and from internal sources and system components as described in Figure 3.2.

The total load (sensible and latent) in a zone can generally be expressed by the following equation.

$$Q_{Total} = Q_{roof} + Q_{walls} + Q_{windows} + Q_{people} + Q_{lights} + Q_{appliances} + Q_{ventilation} + Q_{infiltration} \quad (30)$$

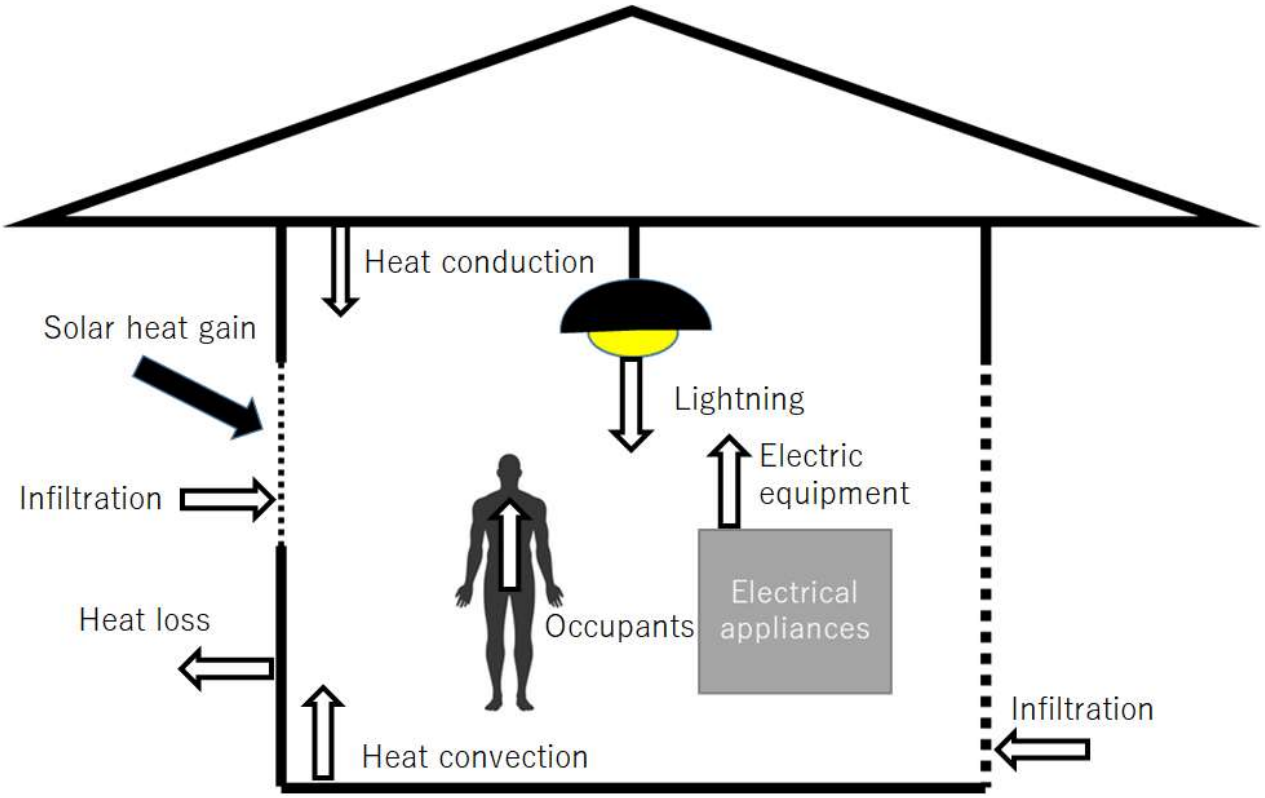

Figure 3.2: Heat balance in building

There are three important multiplier factors which should be taken into account, when the energy budget for a building is being calculated [44]:

- CLTD is the theoretical temperature difference based on the internal and external temperature difference due to the daytime temperature change, solar heat gain and heat accumulation in construction assembly / building. The CLTD factor is used to adjust the heat transfer budget from the wall, roof, floor, glass.

- CLF which explains the fact that all radiant energy entering the conditioned space at a particular time does not immediately become part of the cooling load. The CLF values of the various surfaces are calculated as a function of the time and direction of the sun which can be collected fromin the ASHRAE Handbook. The CLF coefficient is used to adjust the thermal gain due to internal loads such as lighting, occupancy rate and power equipment.

- The SCL factor is used to adjust the transfer heat gain from the glass

Walls and Roofs :

The amount of heat transferred in/out of the building space can be calculated as follows :

$$Q_{roof} = U \cdot A \cdot (CLTD) \tag{31}$$

$$Q_{Wall} = U \cdot A \cdot (CLTD) \tag{32}$$

Where, Q_{roof} *and* Q_{Wall} are load through the roof and walls [Btu/hr], respectively. *CLTD* is cooling load temperature difference[˚F].

Windows :

Heat transfer through the windows has two components :

1. Conductive heat transfer
2. Solar transmission

$$Q_{GlassConductive} = U \cdot A \cdot CLTD_{Glasscorrected} \tag{33}$$

$$Q_{GlassSolar} = A \cdot SC \cdot SCL \tag{34}$$

Where $Q_{Glass\ Conductive}$ is conductive load through the glass [Btu/hr], $Q_{Glass\ Solar}$ is solar transmission load through the glass [Btu/hr]. *SC* and *SCL* represent shading coefficient and solar Cooling Load Factor, respectively.

Partitions, ceiling and floors

Whenever a conditioned space is adjacent to a space with a different temperature, the transfer of heat through the separating physical section must be considered. This heat transfer is calculated using the following equation :

$$Q = U \cdot A \cdot (T_a - T_{rc}) \tag{35}$$

Where T_a and T_{rc} represent the temperature of adjacent space[◦F] and indoor temperature of conditioned space[◦F], respectively. It should be noted that the temperature T_a can be vary from the temperature of the air-conditioned space. For example, the temperature in a kitchen or boiler room can be 15-50[◦F] above outdoor temperatures.

Internal cooling loads :

The various internal loads consist of sensible and latent heat transfers are due to occupants, products, processes, appliances and lighting. The heat emitted from the lighting is the only sensible thermal load. The ratio of the sensible heat gain, Qinternal gains (from lighting, people, appliances, etc.) to the total cooling load, Qcooling load is as a function of the thermal storage characteristics of that space which can be adjusted by using an appropriate cooling load factors (CLF) as follows :

$$CLF = \frac{Q_{cooling\ load}}{Q_{internal\ gains}} \tag{36}$$

People :

T The sensible and latent heat gains from the occupants is given by the following formula :

$$Q_{sensible} = N(Q_s)(CLF) \tag{37}$$

$$Q_{latent} = N(Q_L) \tag{38}$$

Where

- N = number of people in space from ASHRAE, Table A28-3
- Q_s, Q_L = Sensible and Latent heat gain from occupancy is given in 1997 ASHRAE Fundamentals Chapter 28, Table 3)
- CLF = Cooling Load Factor, by the hour of occupancy. See 1997 ASHRAE Fundamentals, Chapter 28, Table 37

Note: CLF = 1.0, if an operation is 24 hours or of cooling is off at night or during weekends. Table 3.2 gives representative rates at which heat, and moisture are given off by human beings in different states of activity. Often these sensible and latent heat gains constitute a large fraction of the total load. Even for short-term occupancy, the extra heat and moisture brought in by people may be significant.

Table 3.2 Heat gain from occupants of various activities (Indoor air temperature = 78◦F)

Activity	Total heat by adult(male)	Total heat(adjusted)	Sensible heat	Latent heat
Seated at rest [Btu/hr]	400	350	210	140
Seated, very light work, writing [Btu/hr]	480	420	230	190
Seated, eating [Btu/hr]	520	580	255	325
Seated, light work, typing [Btu/hr]	640	510	255	255
Light bench work [Btu/hr]	880	1040	345	695
Light machine work, walking 3ml/hr [Btu/hr]	1360	1280	405	875
Moderate dancing	1600	1600	565	1035
Heavy work, lifting, athletics	2000	1800	635	1165

Lights :

The heat source from lighting primarily depends on light emitting elements. The heat gain rate at a particular moment can be very from the heat equivalent of the power supplied to the light. One part of the energy from the light is in the form of convection heat, which is instantly captured by the air conditioner. The rest are in the form of radiation, which is absorbed and re-emitted by walls, floors, furniture, etc., and then affects the conditioned space. The instantaneous heat gain from electrical lighting can be calculated from the following formula :

$$Q_{lights} = 3.14 \cdot W \cdot F_{UT} \cdot F_{SA} \tag{39}$$

The cooling load factor is used to convert the instantaneous heat gain from the lighting into an appropriate cooling load. Therefore, the instantaneous heat gain from electrical lighting considering the cooling load coefficient can be expressed by the following equation :

$$Q_{lights} = 3.14 \cdot W \cdot F_{UT} \cdot F_{SA} \cdot (CLF) \tag{40}$$

CLF = 1.0 if operation is 24 hours or if cooling is off at night or on weekends.

Infiltration air :

Infiltration is the flow of outdoor air in to or out from the building due to the normal use of cracks and other unintended openings and external doors for entering and exiting. Infiltration is also known as air leaks into the building. As shown in Figure 3.3, air leaks out of the building through similar types of openings.

The heat loss or gain from the infiltration is calculated by the following equations :

$$Q_{sensible} = 1.08 \cdot CFM \cdot (T_o - T_i) \tag{41}$$

$$Q_{latent} = 4840 \cdot CFM \cdot (W_o - W_i) \tag{42}$$

$$Q_{total} = 4.5 \cdot CFM \cdot (h_o - h_i) \tag{43}$$

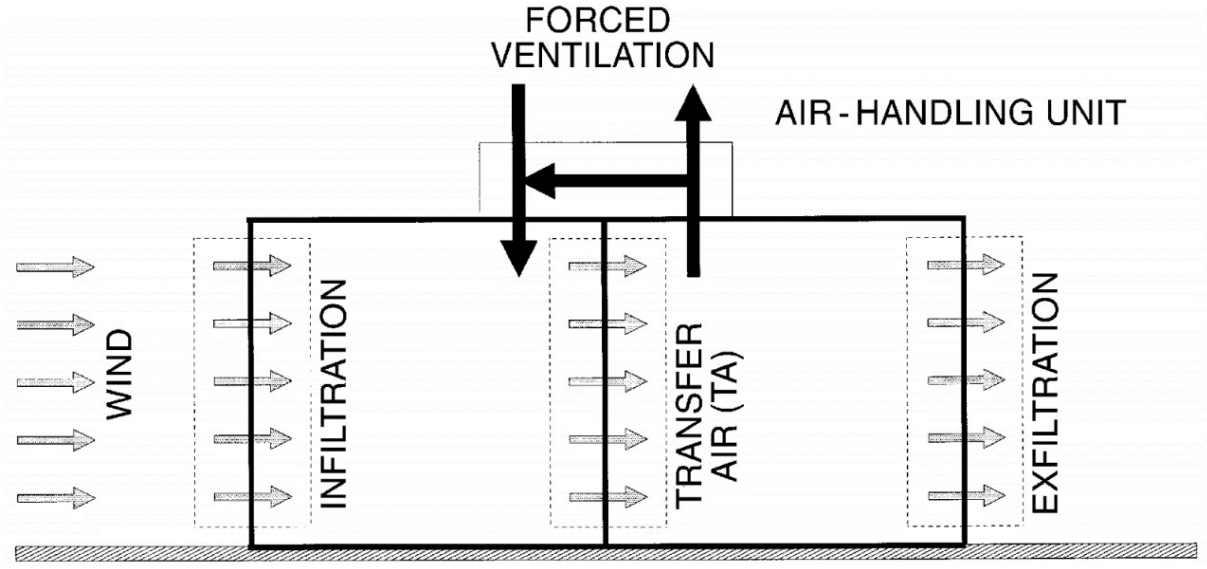

Figure 3.3: Two-Space Building with Forced Ventilation, Infiltration, and Ex-filtration. Adopted from Ref. [43].

where *CFM* is infiltration air flow rate. T_o and T_i represent outdoor and indoor dry bulb temperatures[◦F], respectively. W_o and W_i represent outdoor and indoor humidity ratios [lb water/lb dry air], respectively. h_o and h_i represent outdoor and indoor air enthalpies [Btu /lb (dry air)], respectively

Ventilation :

Ventilation air is the amount of outside air that is required to maintain the occupant's indoor comfort. In general, heat is added to the air flow in front of the cooling coil and does not directly affect the space conditions. The additional cooling coil load is calculated as follows :

$$Q_{sensible} = 1.08 \cdot CFM \cdot (T_o - T_i) \quad (44)$$

$$Q_{latent} = 4840 \cdot CFM \cdot (W_o - W_i) \quad (45)$$

$$Q_{total} = 4.5 \cdot CFM \cdot (h_o - h_i) \quad (46)$$

Where *CFM* is ventilation air flow rate. T_c is the dry bulb temperature of air leaving the cooling coil[◦F]. W_c is the humidity ratio of air leaving the cooling coil [lb (water) /lb (dry air)]. h_c represents the enthalpy of air leaving the cooling coil [Btu/lb (dry air)].

Appliances :

The sensible and latent heat gain from the electrical appliances can be calculated by using the following equations :

$$Q_{appliances} = q_{input} \cdot F_u \cdot F_r \cdot CLF \quad (47)$$

$$Q_{latent} = q_{input} \cdot F_L \quad (48)$$

Where, q_{input} is rated energy input from appliances.

F_u and F_r represent usage factor and radiation factor, respectively.

3.7.1 Calculation of electricity consumption and thermal load simulation by EnergyPlus software

In this research, EnergyPlus software is used to estimate the total energy consumption (Electrical and thermal Loads) of a standard Japanese building, using the above principles. EnergyPlus is a simulation software created based on both BLAST and DOE - 2 programs which is used for the estimation of energy demand in a building, based on the user's description of the building from, the building's physical configuration, the relevant mechanical system, etc., the thermal control setting values and the condition of the HVAC system as a whole [45]. The detailed explanation about the calculation method used in EnergyPlus can be found in Appendix I.

Chapter 4

Optimization model

4.1 Categorization of optimization

Optimization methods are mainly classified into mathematical methods and meta-heuristic methods which are shown in Figure 4.1[46]. With rapid development in computer science, Artificial Intelligence (AI) and metaheuristic methods have been become very popular which are classified into swarm intelligence (SI), non-SI, and algorithms inspired as shown in Figure 4.2. The Off-grid microgrid system optimization models are based on the single AI-based methods, analytical methods, and hybrid optimization methods. Among all existing methods, Genetic Algorithms (GA), PSO, and Simulated Annealing (SA) are the most common algorithms which are used in the Microgrid optimization. The optimal sizing of power generation units in a microgrid system is very important in order to efficient enhancement of renewable energy resources. To this aim, optimization techniques are mainly founded on the basis of the minimization of the total of the system, subject to satisfying the technical and environmental constraints. The mathematical expression of an optimization problems (NOP) can be defined as finding such $x \in S \subset \mathrm{R}^n$ that [47]

$$\begin{cases} f(\vec{x}) = min\{f(\vec{y}); \vec{y} \in S\} \\ g_j(\vec{x}) \leq 0, forj \in [1, m] \end{cases} \tag{49}$$

Where, $\vec{x} = (x_1, \ldots, x_d, \cdots, x_D)(1 \leq d \leq D, d \subset \mathbb{Z})$ and $x_d \in [l_d, u_d]$ and u_d are lower and upper values constraints, respectively. f and g_j are functions on S . S is a D -dimensional space defined as a Cartesian product of domains of variables x_d's. The set of points, which satisfying all the constraint function g_j is donated as feasible space (S_F).

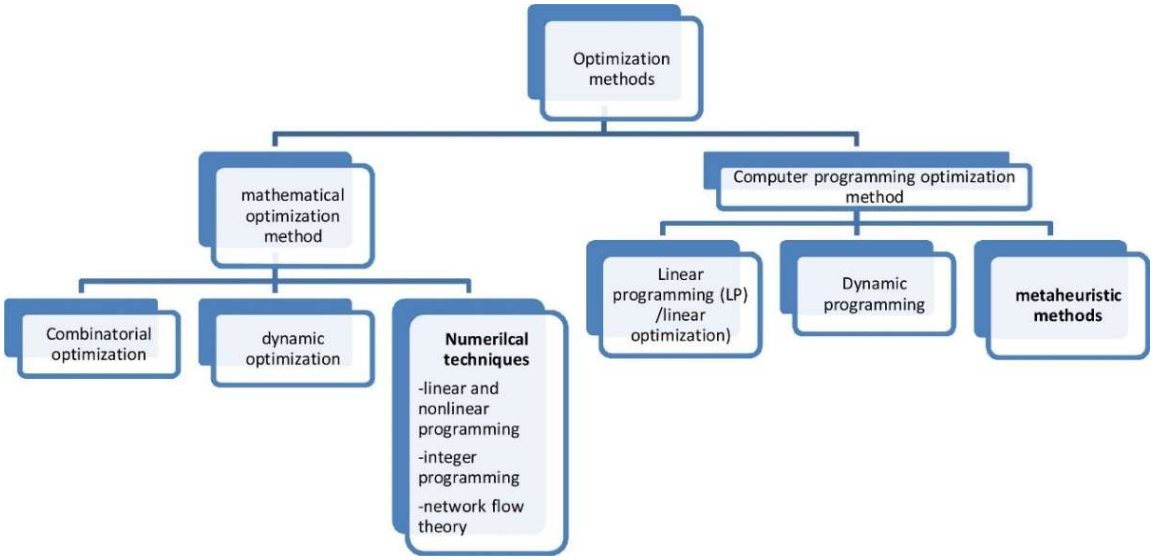

Figure 4.1: Classification of optimization methods. Taken from Ref. [46].

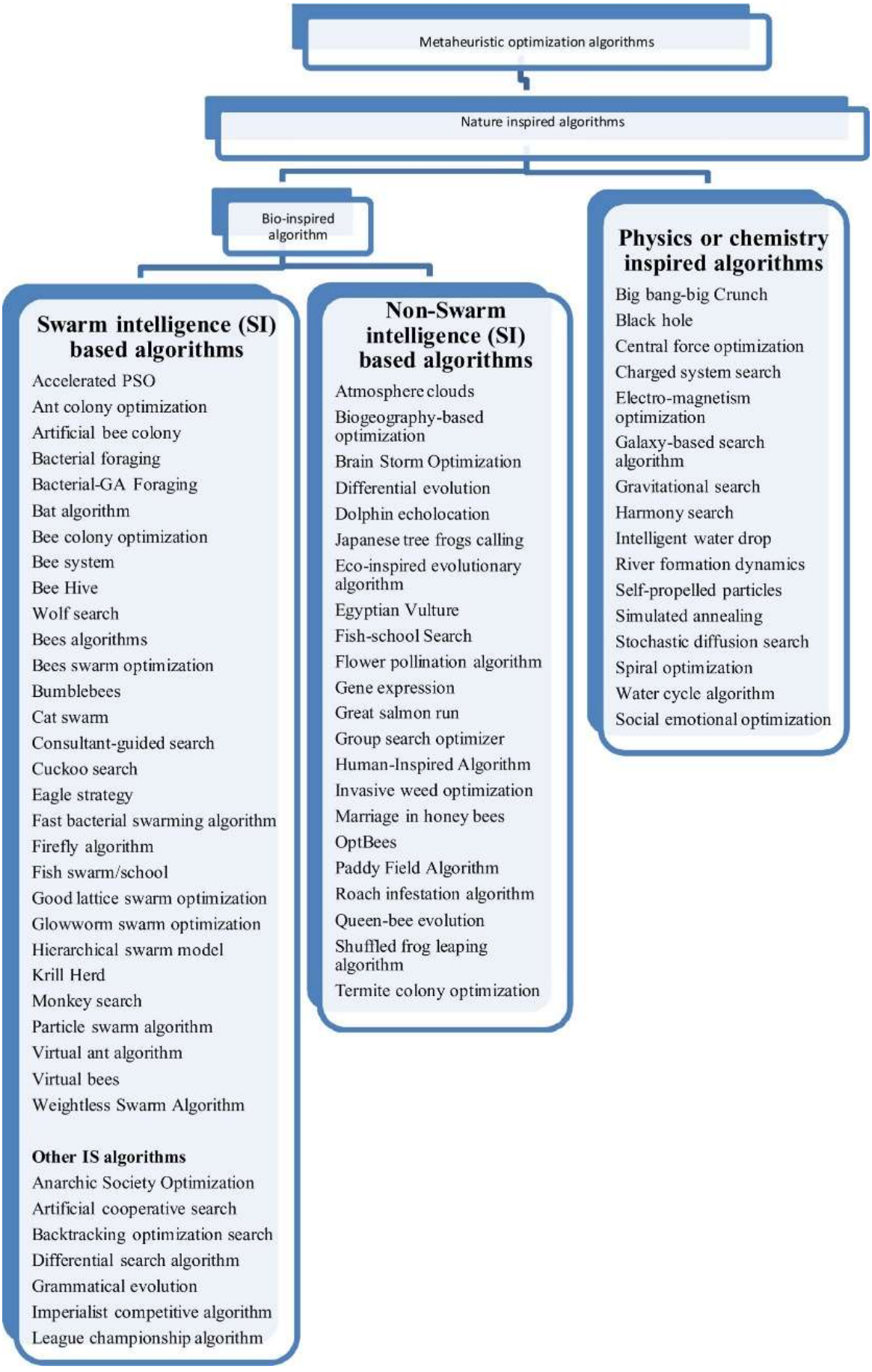

Figure 4.2: Categorization of metaheuristic optimization algorithms[46]

4.2 Objective function

The objective function in this research is identified as the total cost of the microgrid system over its lifetime. The lifetime of the system is considered to be 20 years. The vector of the decision variables of the model are [13]:

$$P = [P_{PV}, P_{WG}, P_{bat}] \tag{50}$$

Where, P_{PV} is the capacity of PV panels [kw], P_{WG} is the capacity of the wind turbine[kw], P_{bat} is the capacity of batteries[kWh]. The total cost of the system consists of investment cost, operation and maintenance cost, fuel cost, and replacement cost over the project lifetime :

$$S_{CL} = \sum_{i=1}^{n} \frac{I_t + M_t + F_t}{(1+r)^t} \tag{51}$$

Where, S_{CL} is the total cost of the system over the lifetime [JPY]. I_t, M_t and F_t are investment expenditures [JPY], O&M expenditures [JPY] and fuel expenditures in the year t[JPY]. r shows discount rate [%]

4.3 Demand-Supply Balance

The main objective of the model is to find the optimal value of the installed capacity of PV, wind power generator, battery and diesel generator subject to satisfying the following equality :

$$P_{PV}(h) + P_{wind}(h) + P_{diesel}(h) + P_{battery\ discharge}(h) = P_{Demand}(h) + P_{battery\ charge}(h) \tag{52}$$

Both strategies of battery charging and discahrging are shown in Figure 4.3 and Figure 4.4.

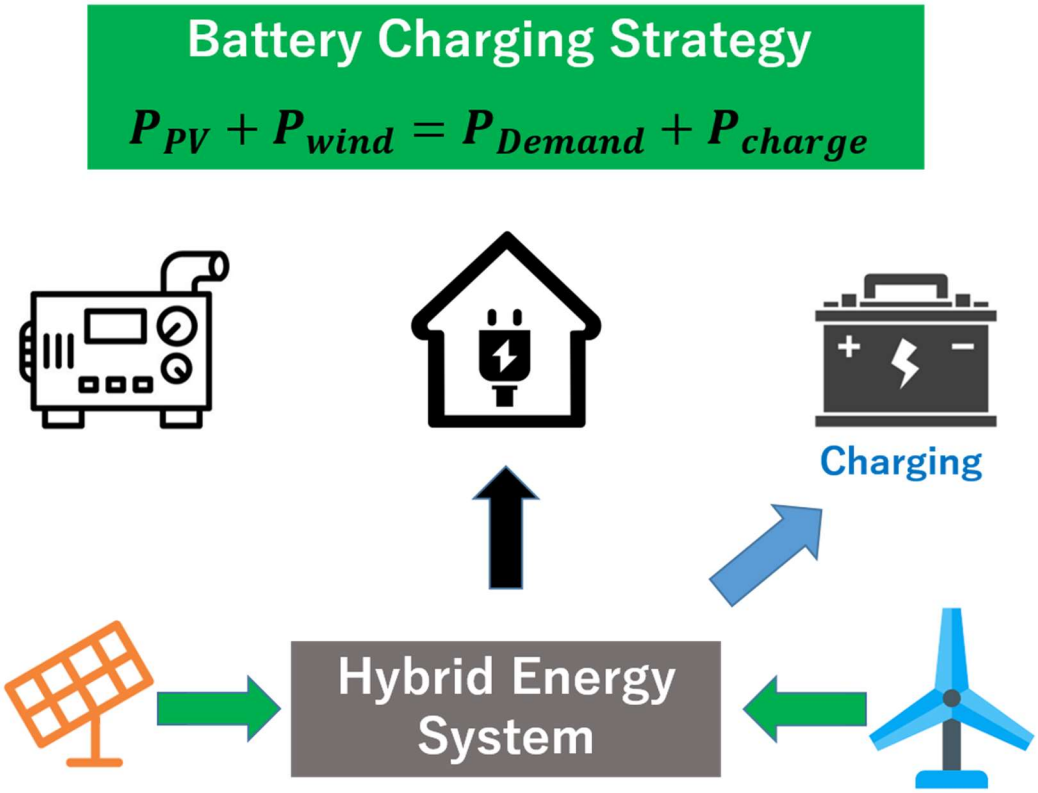

Figure 4.3: Battery Charging Strategy

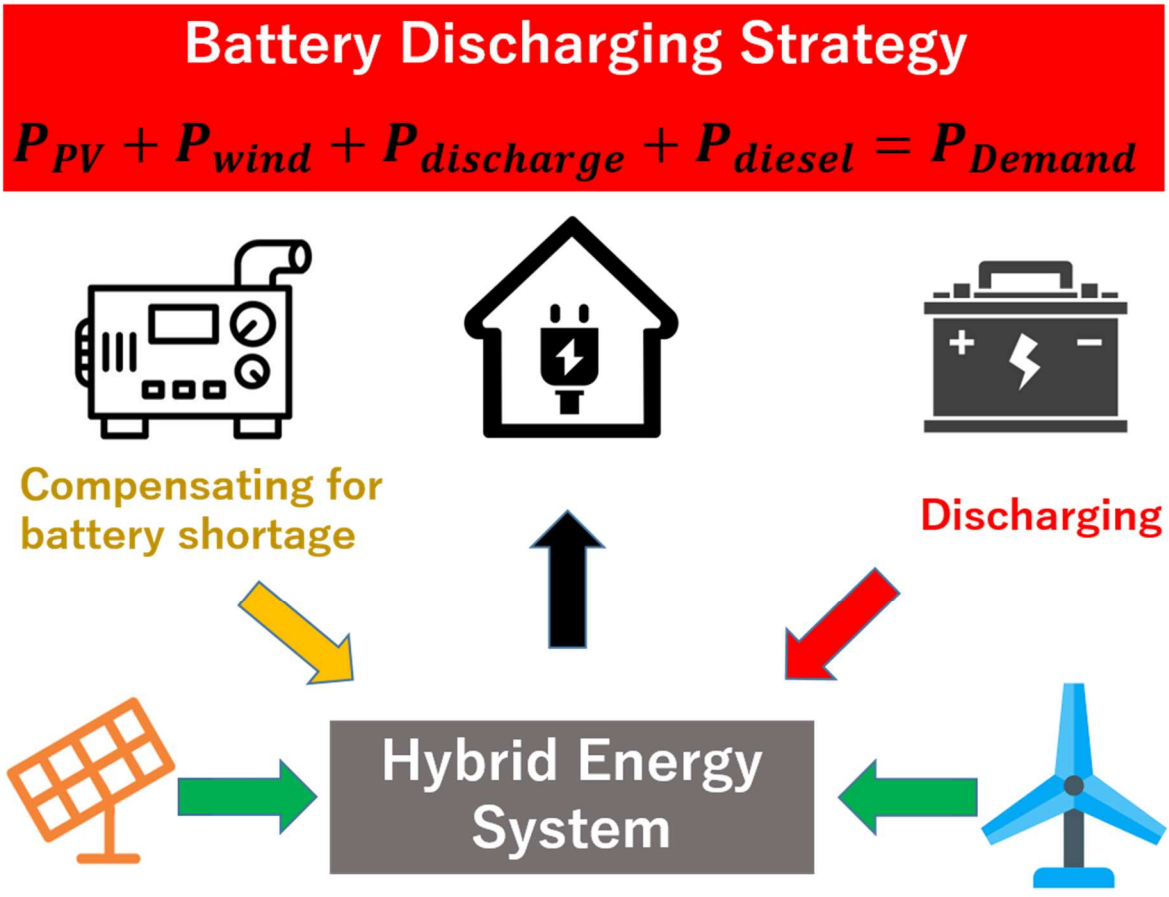

Figure 4.4: Battery Discharging Strategy

4.4 Solving Method: Particle Swarm Optimization (PSO) algorithm

In this research, Particle Swarm Optimization algorithm is used to find the least expensive combination of the decision variables which are shown in Eq. (71) [13]. Particle Swarm Optimization is originally proposed to simulate birds searching for food, the movement of fishes' shoal, etc. It can simulate behaviors of swarms in order to optimize a numeric problem iteratively. Particle Swarm Optimization (PSO), proposed by R. Eberhart by J. Kennedy in 1995, has become very popular because the continuous optimization process allows for multi-target changes [34]. This method, which consists of a constant search of the best solution, moves the particles at a specific speed calculated in each iteration. The expected result is that the particle swarm converges to the best solution. In PSO, a randomly generated particles of swarms which are described by their position and velocity vector fly through the search space by following the current optimum particle [48]. Particles motions are defined by a vector, which defines the velocity of the swarm in each direction. The best solution for each particle obtained so far is stored in the particle memory and named particle experience. In addition, the best-obtained solution among all particles so far is named the best global particle. The velocity and position for each swarm are updated according to its experience and the best global particle. The experience sharing of each particle with other swarms is the most important reason behind PSO success, and it leads the particle to move to a better region. First, a random population of swarms is generated with random position vectors and velocity vectors. The fitness value of each particle is calculated to evaluate the current position of particles and compare it with its best experience and other swarms' fitness value. If the current position of the particle is better than the best historically obtained one, the experience of the particle is adjusted. Moreover, the velocity of a particle is adjusted according to the global best particle and its bests own experience. In fact, particles move toward the best global particle in each iteration. Finally, the best global particle will be updated, as shown in Figure 4.5. As mentioned earlier, each particle has two state variables, its current position, and its velocity. The best experience for each particle is stored in the particle memory while the global best position denotes the best global particle among the population. In each iteration, the position and velocity of the particles are updated toward the best experience and the best global particle by applying recursive Equations (52) and (53).

$$v_{id}(t+1) = \omega \cdot v_{id}(t) + c_1 \cdot \phi_1 \cdot (P_{id}(t) - x_{id}(t)) + c_2 \cdot \phi_2 \cdot (g_{id}(t) - x_{id}(t)) \tag{53}$$

$$x_{id}(t+1) = x_{id}(t) + v_{id}(t+1) \tag{54}$$

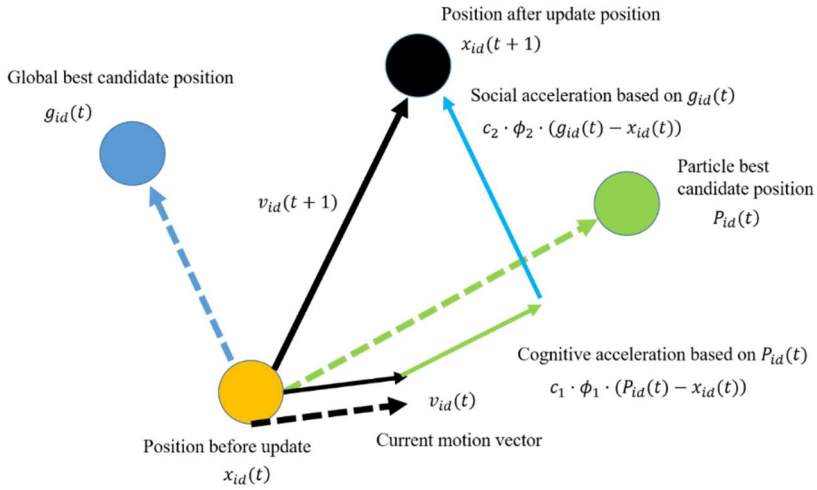

Figure 4.5: Dynamic of swarm in PSO

There are three main terms in the velocity update equation. The first term $v_{id}(t)$ represents the velocity of inertia and u is called the coefficient of inertia. This term ensures that the velocity of each particle does not change rapidly, but rather the previous velocity of the particle is taken into account. As a result, particles generally tend to point in the same direction as the flying direction. The parameters c_1 and c_2 are positive weighting constants, represented as "self-confidence" and "swarm confidence" respectively. They control the movement of individual particles versus their global best. The parameters φ_1 and φ_2 are two uniform random numbers between 0 and 1. The first iteration ends by adjusting the speed and position of the next time step $t + 1$. Consistently, this process is performed until specific stopping criteria is met. The stopping criterion is the maximum number of steps, the improvement of the best objective function value, or an average value calculated from all population objective function values. The main parameters of the PSO algorithm are ω, c_1, c_2 and the size of the group. These parameters are extrinsic that are initialized by the user prior to execution. The optimal setting of the parameters depends on the problem at hand. According to the literature, PSO parameters are set at the following intervals. Inertia weight ω is the high settings in the range [0.5, 1] and near 1 facilitates global search [13]. Swarm size depends on problem search space; the number of particles can be in the range (20-60). Acceleration coefficients are usually an equal value of c_1 and c_2 which is used within the range [0, 4]. In this paper, for all variants, fixed values considered as defaults for PSO parameters were used as $c_1 = c_2 = 1.5$, $\omega = 0.8$, iterations = 100, population size = 20[13,48]. Figure 4.6 shows the PSO pseudo code included boundary conditions in this research.

```
FOR each particle i
   FOR each dimension d
      Initialize position x_id randomly within range
      Initialize position v_id randomly within range
   End FOR
END FOR
Iteration k=1
DO
   FOR each particle i
      Calculate fitness value
      IF the fitness value is better than p_best_id in in history
         Set current fitness value as the p_best_id
      END IF
   END FOR
   Choose the particle having the best fitness value as the g_best_id
   FOR each particle i
      FOR each dimension d
         Calculate velocity according to the equation (11)
         Update particle position according to the equation (12)
         IF Updated particle occurs the boundary
            Update particle takes dumping
         ENDIF
      END FOR
   END FOR
k=k+1
WHILE maximum iterations or minimum error criteria are not attained
```

Figure 4.6: Particle swarm optimization algorithm

4.5 Boundary conditions for PSO

Four types of boundary conditions have been reported for: absorption, reflection, invisibility, and attenuation as shown in Figure 4.7 [49]. In this research, the attenuation will be used to represent the boundary condition. Figure 4.8 shows the unique features that distinguish this boundary condition. There are two groups, restricted and unlimited. Limited boundary conditions such as absorption, reflection, and attenuation relocate the wrong particles in the acceptable solution space, evaluate the fitness function, and provide a valid solution to the optimization problem. Therefore, the entire trajectory of the swarm is confined in the feasible area. On the other hand, unbounded boundary conditions, such as hiding, simply assign an inappropriate fitness value to the wrong particle, for example, a very large value to minimize the problem, and the fitness evaluation is skipped and invalid which prevents solutions from being generated. In this study, Damping is used as the boundary condition. Figure 4.9 shows the concept of damping when particles are updated out of the search space.

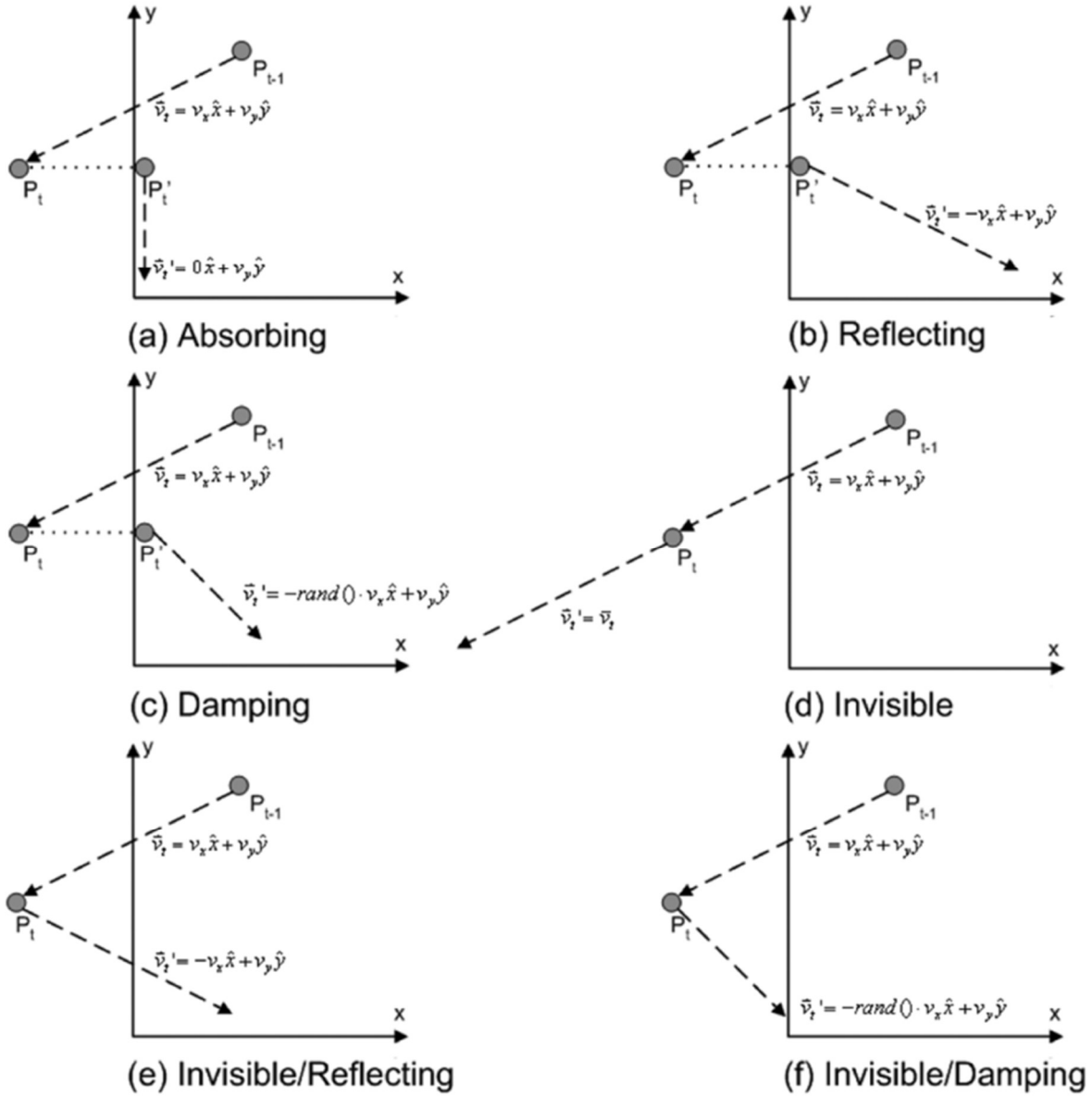

Figure 4.7: Six different boundary conditions for a two-dimensional problem. $\boldsymbol{P'}$ and $\vec{\boldsymbol{v}}$ represent the modified position and velocity, respectively, after the errant particle is treated by boundary conditions. Adopted from Ref. [49].

Figure 4.8: Summary of various boundary conditions. Adopted from Ref.[49].

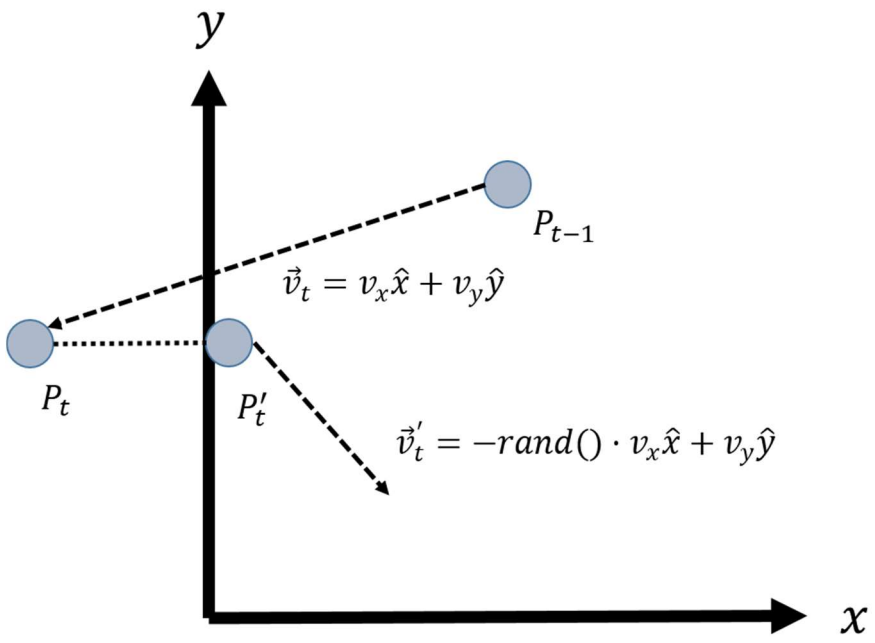

Figure 4.9: Boundary conditions for PSO developed in this research. Adopted from Ref. [49]

Chapter 5

Weather forecasting model

This research predicts the amount of hourly electricity generation from solar and wind power systems, using the GPV-MSM weather forecast which is provided by the Japan Meteorological Agency. The GPV-MSM weather forecasting system reproduces atmospheric phenomena using non wet Meso scale modeling [29]. As shown in Figure 5.1, Meso model which considers the calculation area in Japan and its neighboring seas includes a horizontal grid of 5km.

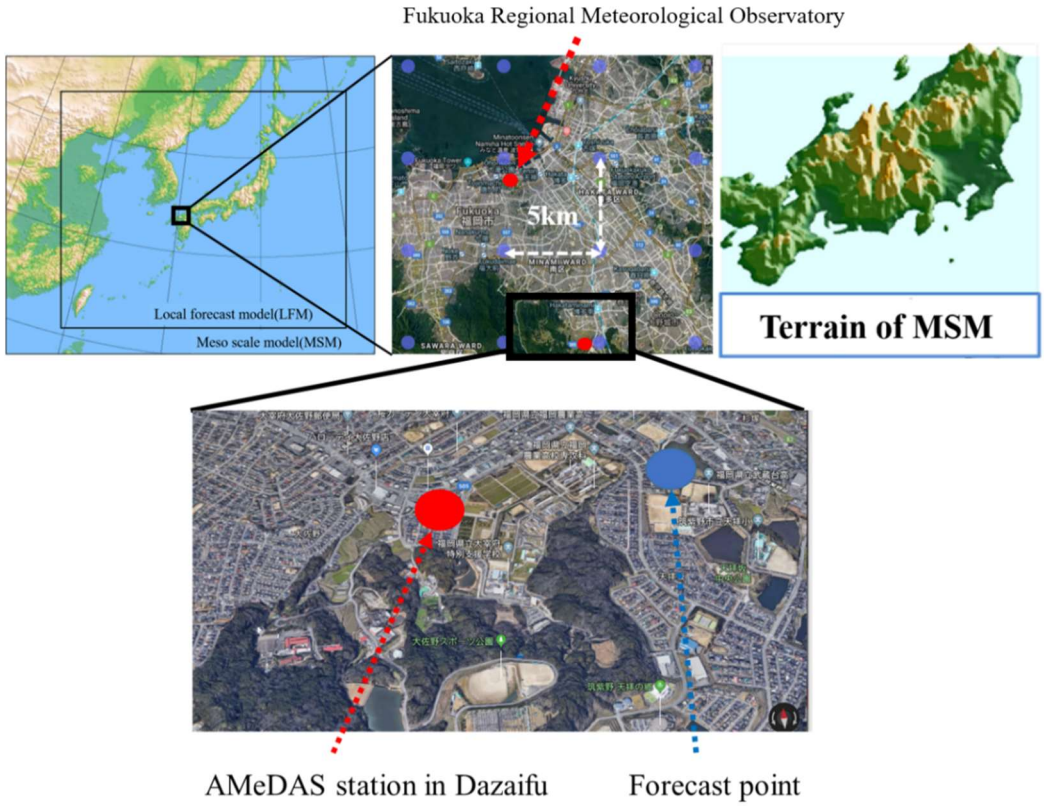

Figure 5.1: Topographic resolution of MSM and two points of meteorological GPV data (MSM-S, 10m above ground) in this study

Hourly forecasts of 7 weather-related variables are provided eight times a day (00:00, 03:00, 06:00, 09:00, 12:00, 15:00, 18: 00, 21:00 UTC time zone). The forecast period depends on the forecast time and can be up to 39 hours or 51 hours ahead. In this research, we used the first 24 hours of forecast weather data up to 39 hours or 51 hours ahead updated at UTC 00:00 hours (JST 9:00) [50,51]. Temperature and wind speed are the actual meteorological data were measured at AMeDAS Observatory in Dazaifu City [52]. The solar radiation and the Mean Sea Level pressure (MSL) are those which can be observed from the Fukuoka District Meteorological Observatory. On the other hand, the forecast data uses the data of the lattice point closest to this AMeDAS station. Since the position and altitude of the

forecast data and observation data are slightly different, the wind speed and MSL were corrected using the following formula. The position and altitude of the predicted data and observation data are different which causes forecasting errors in the wind speed and MSL data. Therefore, using the following formula, the average ratio k between the predicted data and the observed data was derived and corrected through multiplying it to the predicted data.

$$k = \frac{\vec{r}}{\vec{p}} = \frac{\sum_i^n r_i}{\sum_i^n p_i} \tag{55}$$

$$\vec{p_i} = kp_i \tag{56}$$

$\vec{r}$ and $\vec{p}$ are average values. r_i and p_i are the actual measurement values and forecast values before correction at each time. p_i is the corrected forecast value. n is a number of values. Figures Figure 5.2, Figure 5.3, Figure 5.4 and Figure 5.5 show the values of each measured and forecast meteorological data at each time step. Figure 5.7 shows the observed versus the predicted regression scatter plot derived from the linear model. Figure 5.6 shows the MSL and wind speed over the first week of May 2019. As can be seen from this figure, more accurated prediction values can be obtained by executing correction. *MAE*, *RMSE* and R^2 were used as indicators for evaluating the forecast data. Mean absolute error (*MAE*) measures the average magnitude of the error in a series of predictions regardless to direction. Root Mean Square Error (*RMSE*) is a second-order scoring rule that also measures the average magnitude of the error. The coefficient of determination (R^2) is an indicator of the goodness of fit of the model and is 1.0 when it is the best fit. These metrics are calculated using the following formulas:

$$MAE = \frac{1}{n}\sum_j^n |y_j - \hat{y}_j| \tag{57}$$

$$RMSE = \sqrt{\frac{1}{n}\sum_j^n (y_j - \hat{y}_j)^2} \tag{58}$$

$$R^n = 1 - \frac{\sum_j^n (y_j - \hat{y}_j)^2}{\sum_j^n (y_j - \bar{y})^2} \tag{59}$$

y is the average of predicted values. The accuracy of the wind speed is not satisfactory because the local wind cannot be reproduced correctly, due to lack of spatial resolution in MSM-GPV [53]. From Figures Figure 5.2 and Figure 5.5, temperature and MSL were predicted precisely. In the case of solar radiation, the value of R^2 is 0.886.

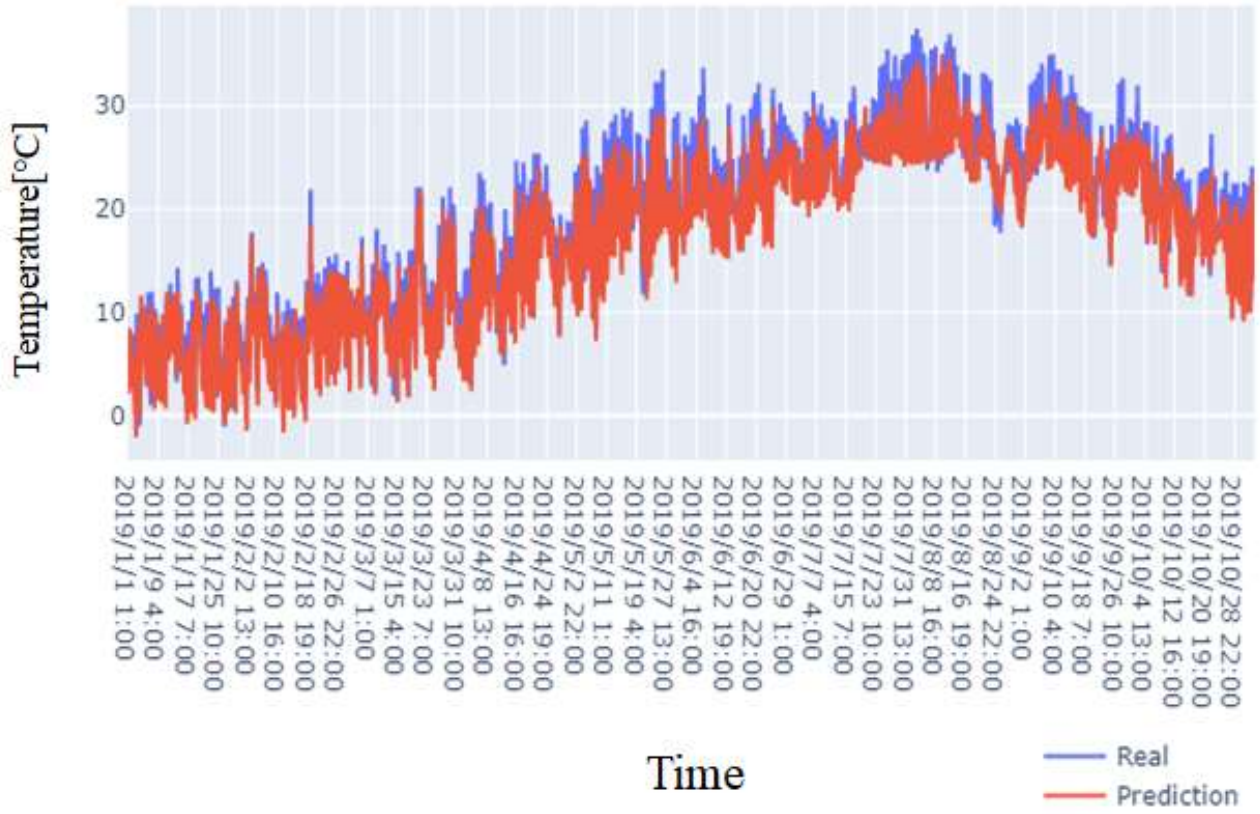

Figure 5.2: Comparison between the measured values and predicted values of temperature in 2019

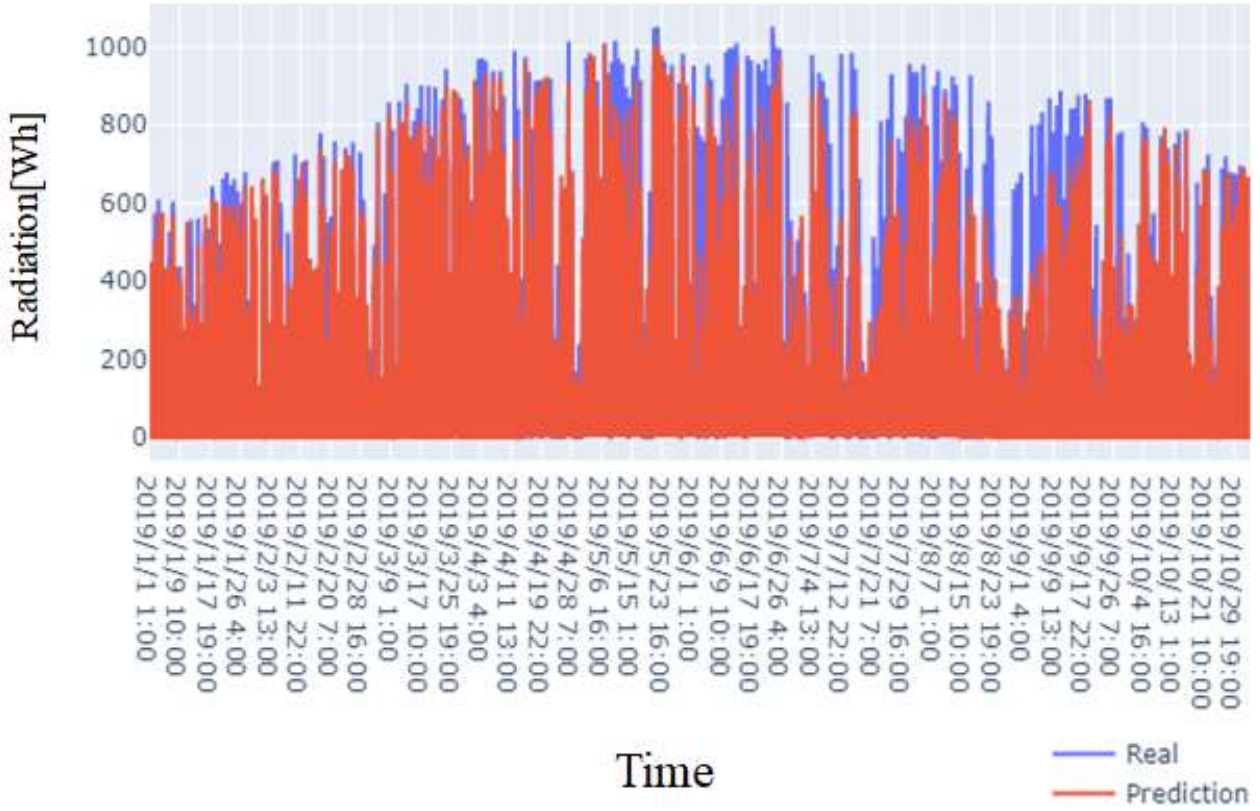

Figure 5.3: Comparison between the measured values and predicted values of radiation in 2019

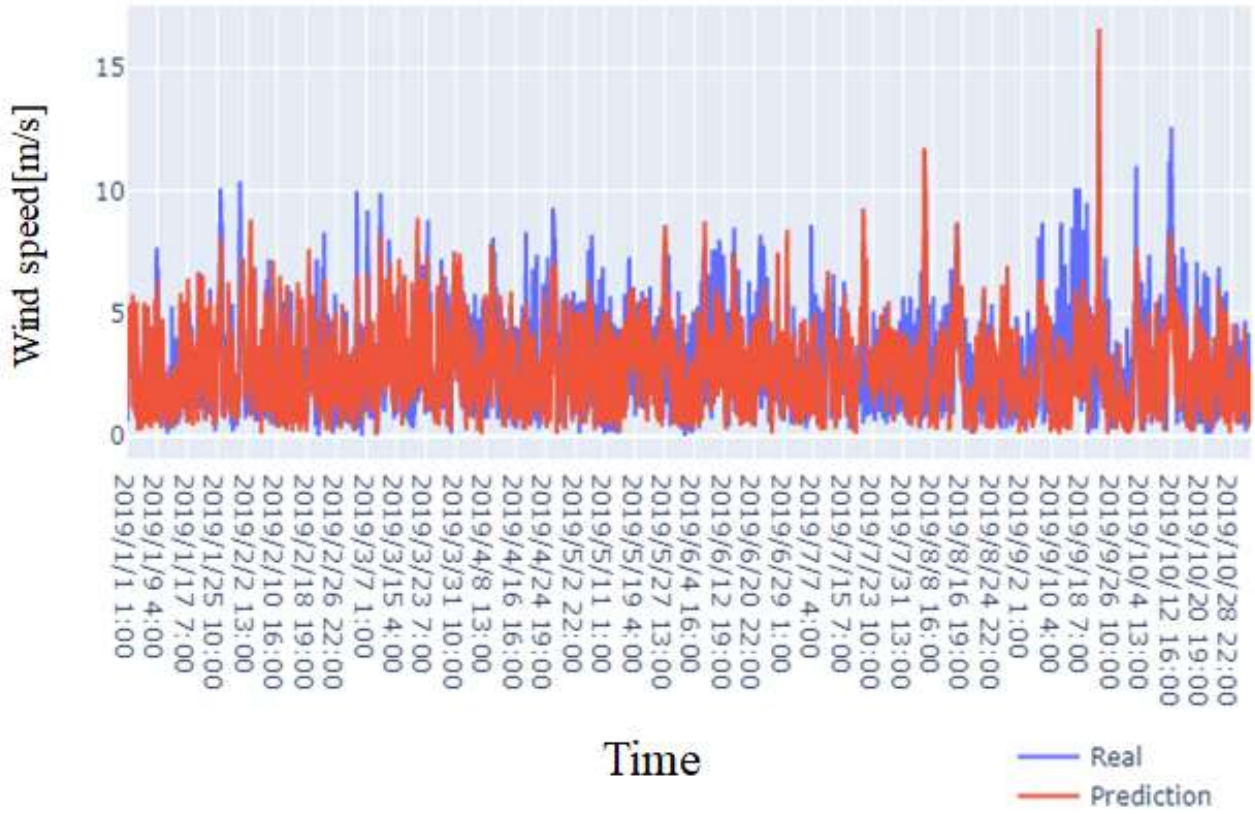

Figure 5.4: Comparison between the measured values and predicted values of wind speed in 2019

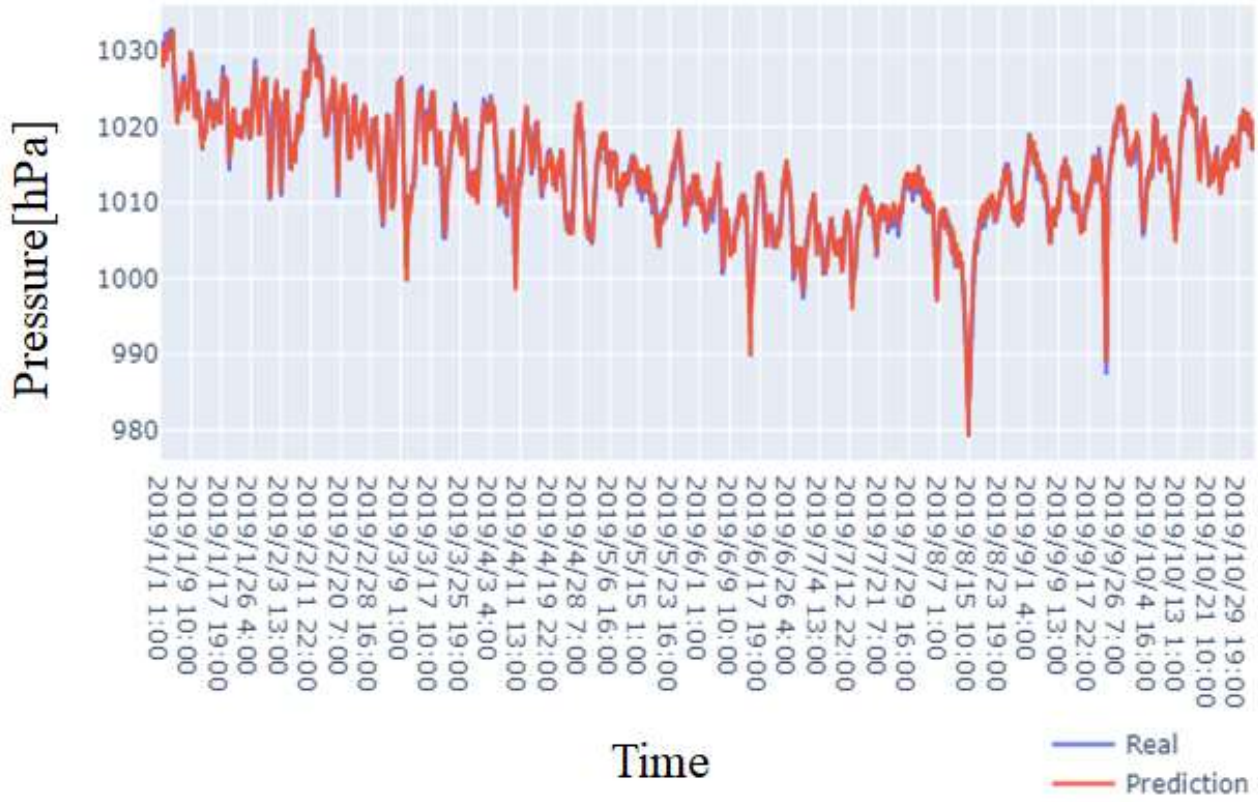

Figure 5.5: Comparison between the measured values and predicted values of MSL in 2019

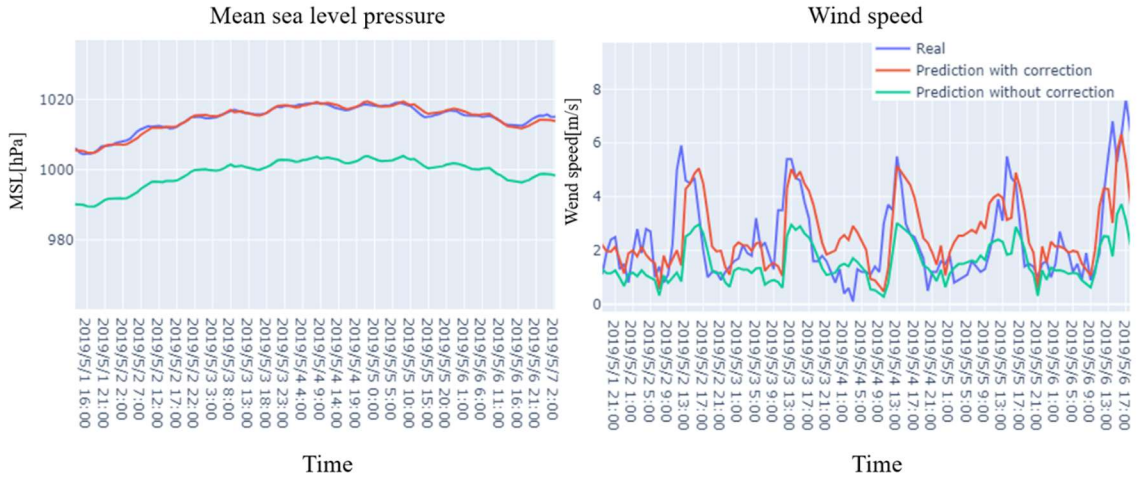

Figure 5.6: Comparison between the measured and predicted values of MSL and wind speed in the first week of May

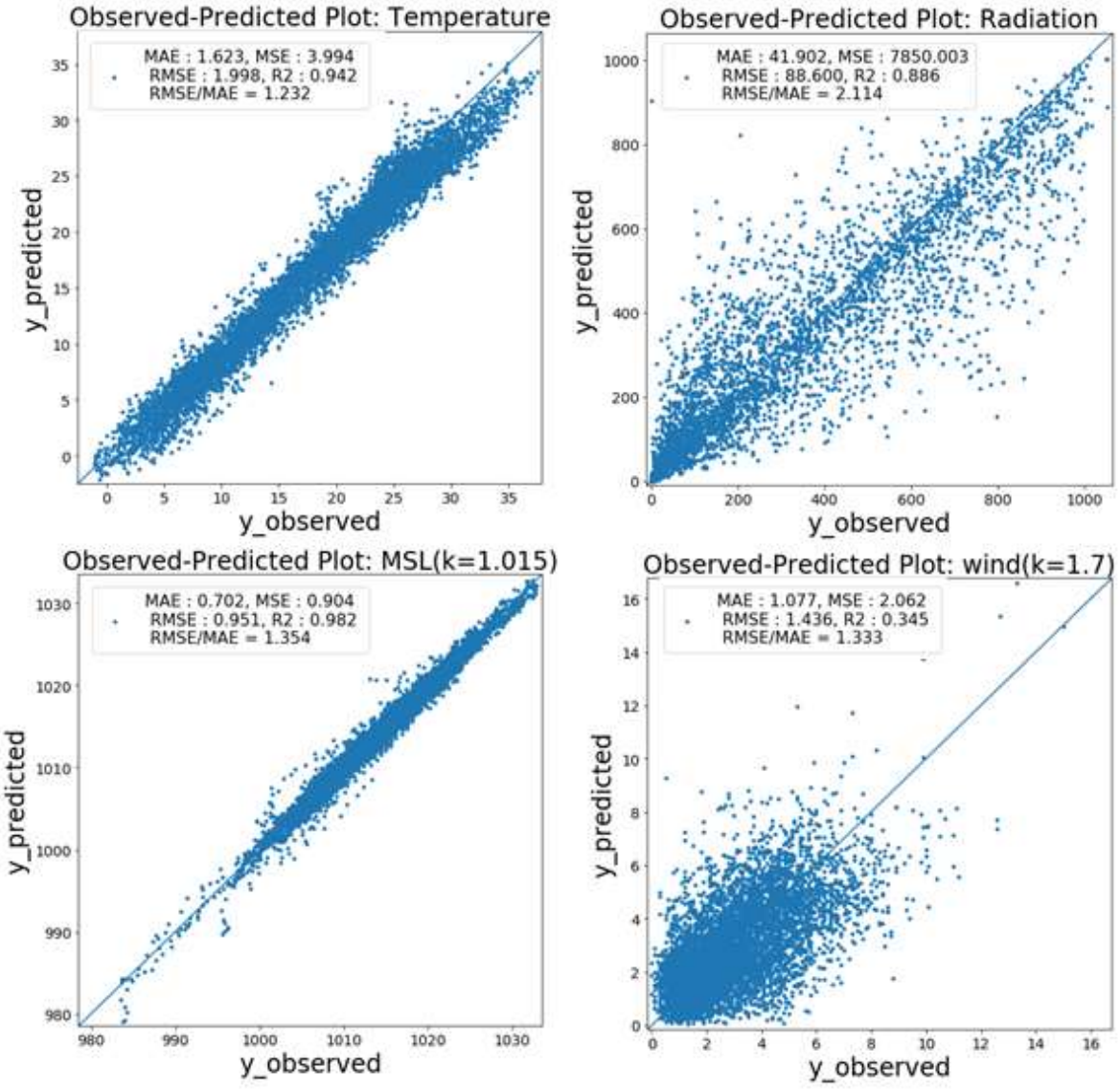

Figure 5.7: Comparison between the measured values and predicted values of meteorological data, and observed-predicted regression scatter plots

Chapter 6

Model Application

6.1 Study area

This study area is located in Kasuga city, Fukuoka, Japan which is as shown in Figure 6.1. This prefecture, located to the north of Kyushu, is a major transportation hub connecting Kyushu and Honshu.

Fukuoka Prefecture covers an area of about 4,987 square kilometers, ranking 29th in Japan. It accounts for 1.3% of the total area of the country and 11.8% of Kyushu. Prefectural land is characterized by relatively gentle topography, a large area of habitable lands such as agricultural land and residential land, and little forest compared to all prefectures in Japan.

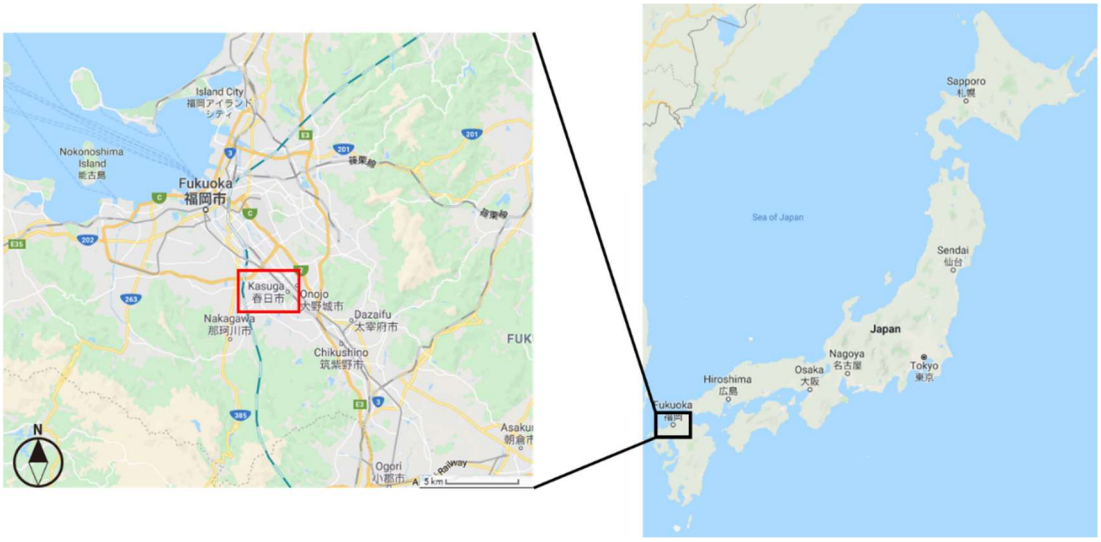

Figure 6.1: Study area in this research which is indicated by the black frame.

The weather in Fukuoka is relatively warm throughout the year. Chikuho and Chikugo regions, which are surrounded by mountains, have a characteristic of inland climate. The amount of rainfall exceeds 1,600 mm annually, and in some mountainous areas at the prefectural border exceeds 2,400 mm. Figure 6.2 and Figure 6.3 show the hourly and monthly average temperature measured by AMeDAS station in Dazaifu City, Fukuoka Prefecture in 2018. In Fukuoka, summer temperatures can be higher than 30°, while winter temperatures rarely drop below 0°. Figure 6.4 shows the Mean Sea Level Pressure measuded by Fukuoka Sendai Regional Headquarters, JMA in 2018. In winter, due to the influence of the Siberian high, the pressure is set to the west high east low, which is relatively high.

Figure 6.5 and Figure 6.6 show the hourly solar irradiation and wind speed. Solar irradiation has been measured at height 10m by AMeDAS station in Dazaifu City, Fukuoka Prefecture in 2018. The wind speed has been measured by Fukuoka Sendai Regional Headquarters, JMA in 2018. The average wind speed is very weak, about 2 m / s, making it difficult for wind power generation. On the other hand, a relatively large amount of solar irradiation indicates that Fukuoka is suitable for solar power generation.

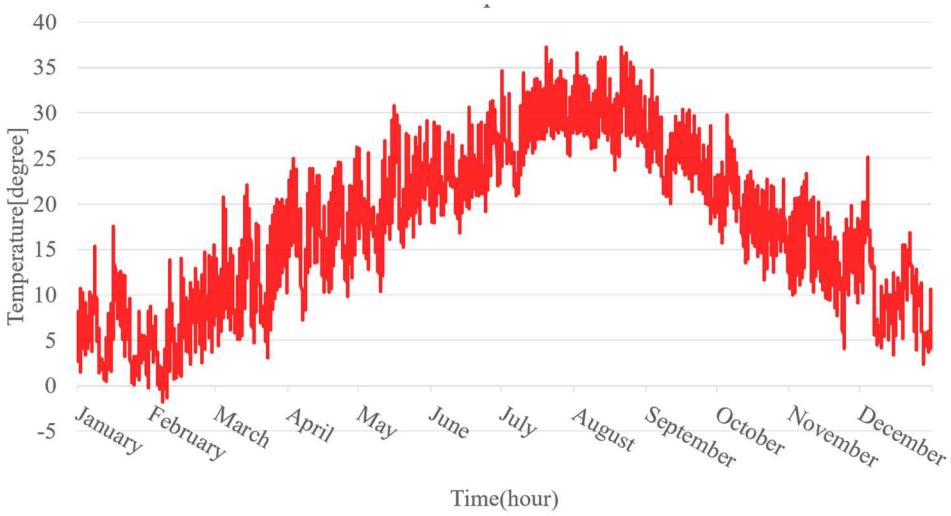

Figure 6.2: Hourly temperature in Fukuoka Prefecture in 2018

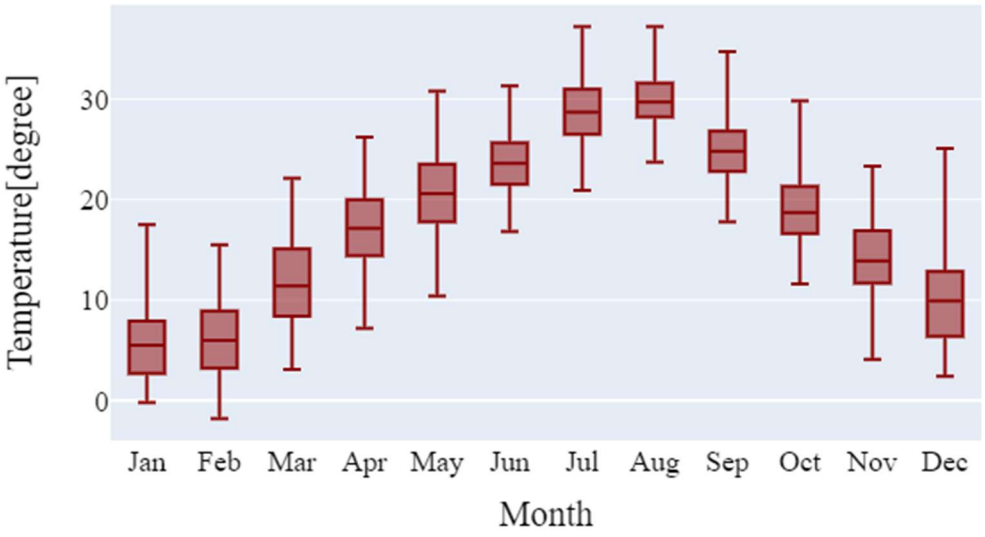

Figure 6.3: Monthly average temperature in Fukuoka Prefecture in 2018

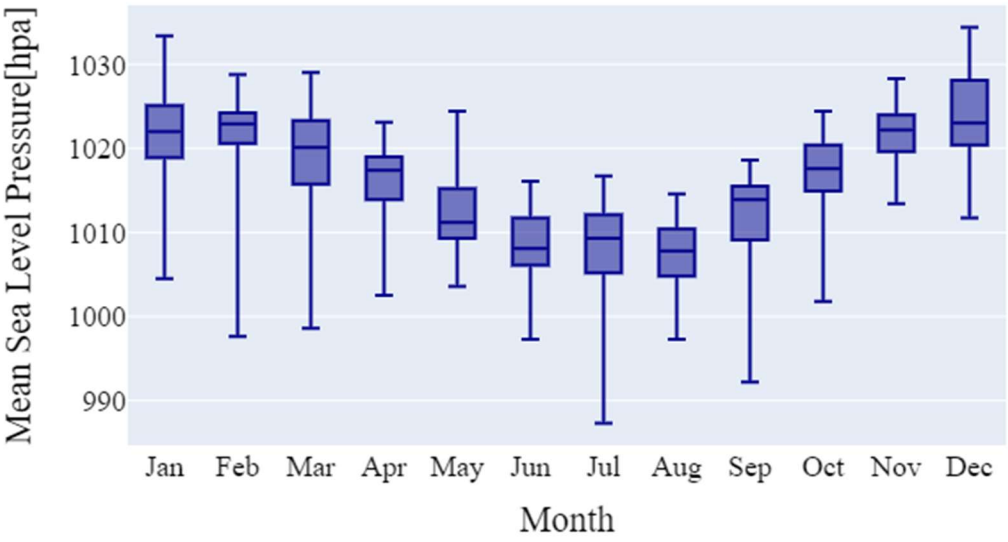

Figure 6.4: Mean Sea Level Pressure in Fukuoka Prefecture in 2018

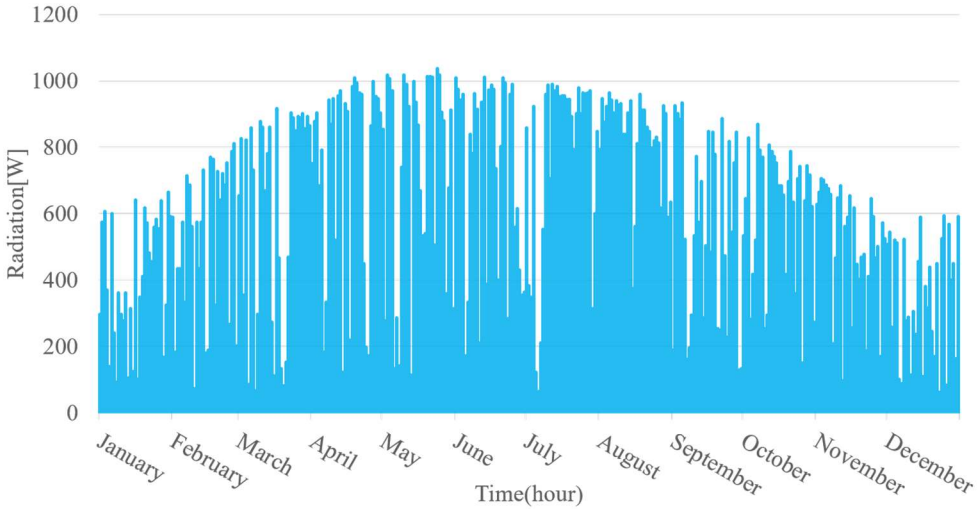

Figure 6.5: Solar irradiation in Fukuoka Prefecture in 2018

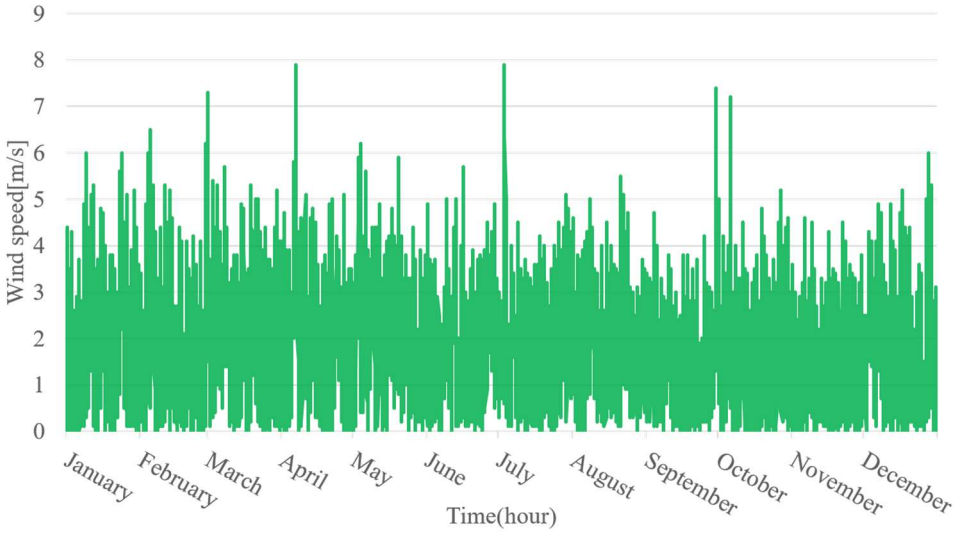

Figure 6.6: Wind speed in Fukuoka Prefecture in 2018

6.2 Demand load calculation

The energy demand simulation program, EnergyPlus, which was discussed in Chapter 3 was used to calculate the annual demand load in a standard Japanese house in the selected area. The 3D model of the targeted Japanese standard house was developed, using Sketchup 2018 which is shown in Figure 6.7 [54,55]. Stairs and furniture were not considered in this 3D model. This 3D model includes all walls, ceilings, floor, doors, and windows. The double glazing glass was used as the standard window in the Japanese house in this study which is a glass that forms a single unit by stacking multiple glass sheets to provide an intermediate layer filled with dry air or argon gas [56]. The different layers of the building and material used in each of the layers are reported in Tables Table 6.1, Table 6.2, Table 6.3 and Table 6.4. The values of the thermal conductivity of each layer were collected from the Building Component Library (BCL) [57]. The weather input data of the model, as the weather data of Fukuoka, was prepared in EPW format [58]. A normal size family, including four inhabitants such as a father, a mother, a son, and a daughter is supposed to live in the targeted building. The activity schedule was set for each person which can be taken into account for the person's internal heat gain calculation. The fraction radiant from each person was set to 0.3. The occupancy schedule of each family member in this building is shown in

Figure 6.8. To meet this schedule, the usage plan of the electrical appliances and lightings are given in Figures Figure 6.9 and Figure 6.10. Tables Table 6.5 and Table 6.6 show the hourly electricity consumption of the electrical appliances in this building. In this study, internal heat generated from electrical equipment and lighting was not included in the simulation. The variable refrigerant flow (VRF) air conditioning system was considered to provide cooling and heating loads [59]. The values of cooling and heating Coefficient of Performance (COP) for this air conditioning system was set at 3.4 and 3.3, respectively. As shown in Figures Figure 6.11 and Figure 6.12, the HVAC operation strategy is based on the heating and cooling schedule in each room. When HVAC is ON, cooling occurs when the temperature is higher than the cooling set point temperature (26 ◦C), and heating is performed when the temperature is lower than the heating set point (18 ◦C). The hourly electricity consumption by the electrical appliances and lighting are represented in Figures Figure 6.13 and Figure 6.14. Figure 6.15 shows the annual electricity consumption by the air conditioning system (Cooling and Heating) in the targeted building in this research.

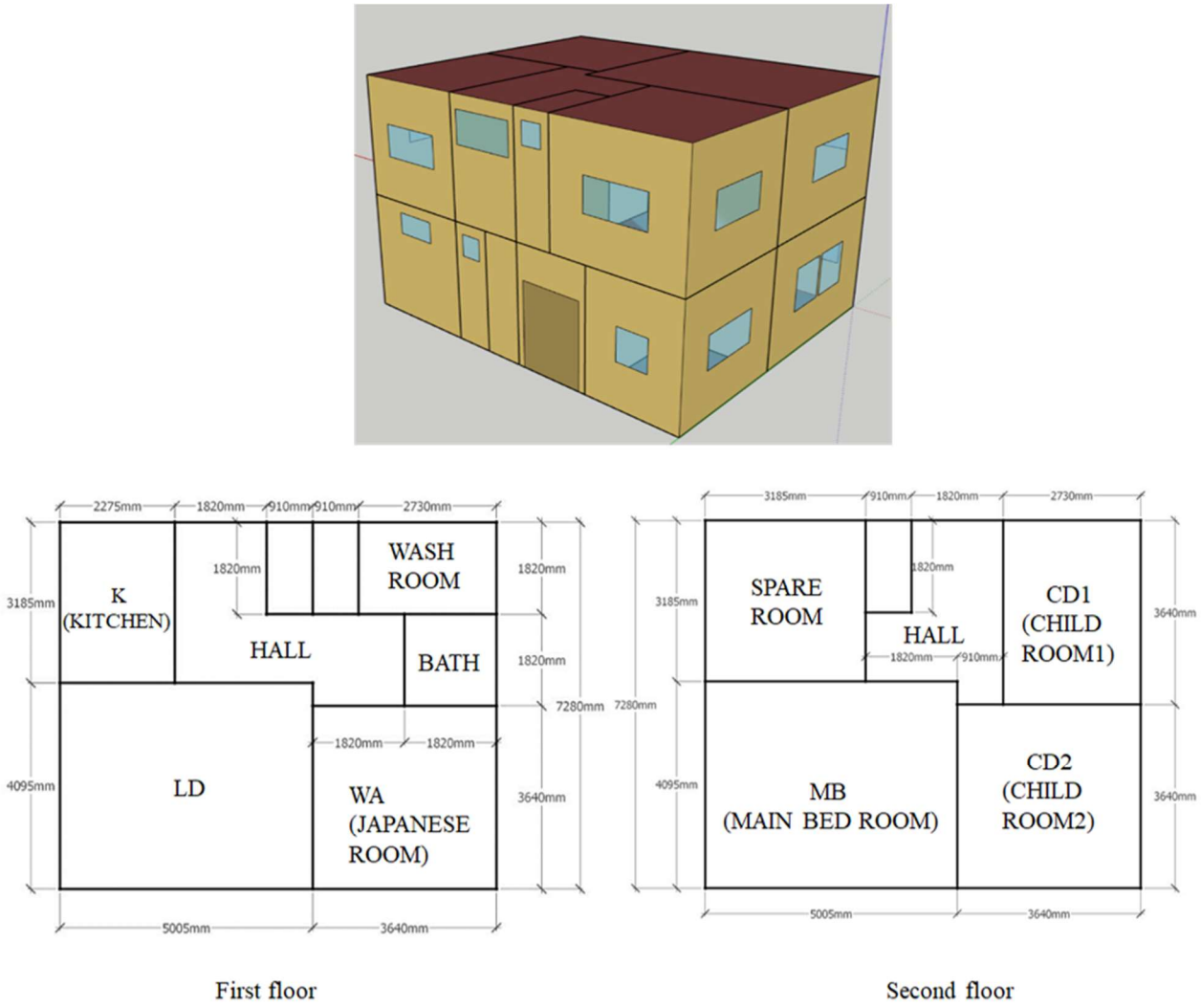

Figure 6.7: Proposed house model and architectural drawing [54,55]

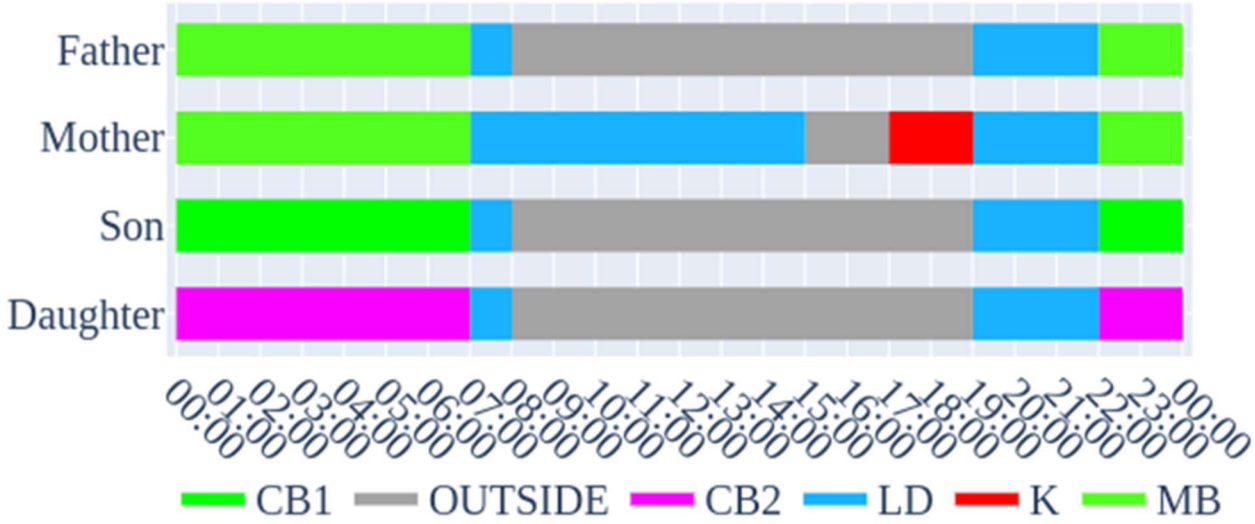

Figure 6.8: Human occupancy schedule(K: Kitchen, LD: Living Dining, MB: Main Bed room)

Table 6.1: Construction of materials [55]

Name	Ext wall	Partition	2st celling	1st floor	2nd floor	Window	1st celling	1st&2nd partition	Door
Layer 1	Mortar 3mm	Mortar 3mm	Steel Framed 1mm	Glass Fiber 150mm	Hollow Layer 20mm	Clear 3mm	Gypsum Board 12mm	Gypsum Board 12mm	Mortar 3mm
Layer 2	Plywood 9mm	Gypsum Board 12mm	Plywood 12mm	Plywood 22mm	Plywood 22mm	Air 12mm		Hollow Layer 20mm	Plywood 9mm
Layer 3	Hollow Layer 20mm	Gypsum Board 12mm	Plywood 9mm			Clear 3mm		Plywood 22mm	Hollow Layer 20mm
Layer 4	Glass Fiber 100mm		Glass Fiber 200mm						Glass Fiber 100mm
Layer 5	Gypsum Board 12mm		Gypsum Board 12mm						Gypsum Board 12mm

Table 6.2: Material data [57]

Name	Hollow Layer	Gypsum Board	Mortar	Glass Fiber	Plywood	Steel framed
Conductivity [W/m-K]	13.33	0.16	0.97	0.036	0.12	0.64
Density [kg/m3]	1.293	800	1601	64	544	81.37
Specific Heat [J/kg-K]	1006	1090	900	960	1210	628
Thermal Absorptance	0.9	0.9	0.9	0.9	0.9	0.9
Solar Absorptance	0.7	0.4	0.7	0.7	0.7	0.7
Visible Absorptance	0.7	0.4	0.7	0.7	0.7	0.7

Table 6.3: Window material data [57]

Name	Clear
Optical Data Type	Spectral Average
Thickness {m}	0.003
Solar Transmittance at Normal Incidence	0.837
Front Side Solar Reflectance at Normal Incidence	0.075
Visible Absorptance	0
Visible Transmittance at Normal Incidence	0.898
Front Side Visible Reflectance at Normal Incidence	0.081
Back Side Visible Reflectance at Normal Incidence	0
Infrared Transmittance at Normal Incidence	0
Front Side Infrared Hemispherical Emissivity	0.84
Back Side Infrared Hemispherical Emissivity	0.84
Conductivity {W/m-K}	0.9
Dirt Correction Factor	1

Table 6.4: Air data [57]

Name	Air
Das type	Dry air
Visible Absorptance	0.0127

Table 6.5: Rated output of lights

Name	Rated output[W]
Normal light	28.9
Bath light	15
Kitchen light	22.8

Table 6.6: Rated output of electrical equipment

Equipment	Rated output[kW]
Microwave	1420
Rice cooker	177
TV	57
Toilet seat	45
Dish washer	160
Refrigerator thermal device	191
Refrigerator electric motor	97

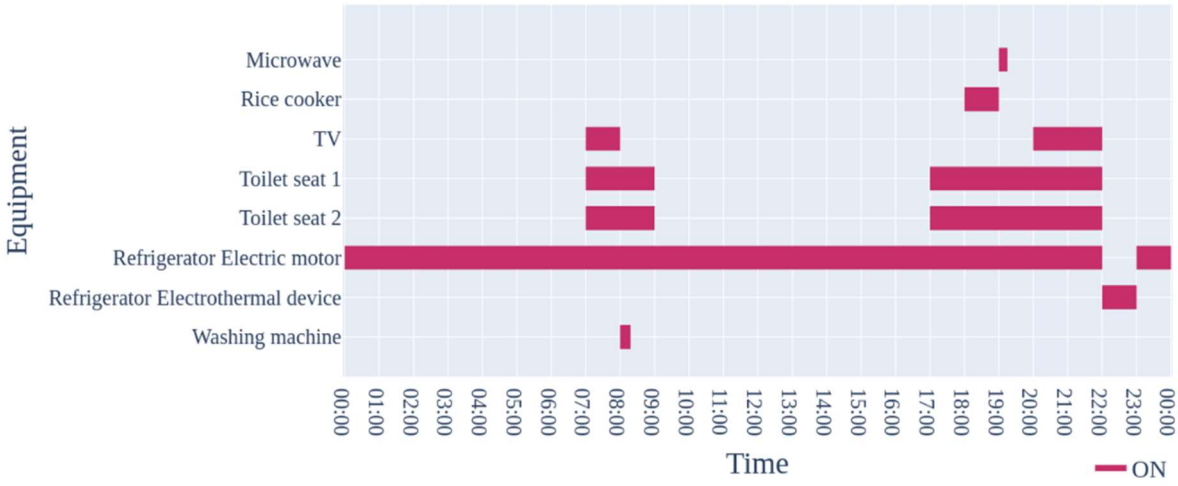

Figure 6.9: Daily electrical equipment usage schedule

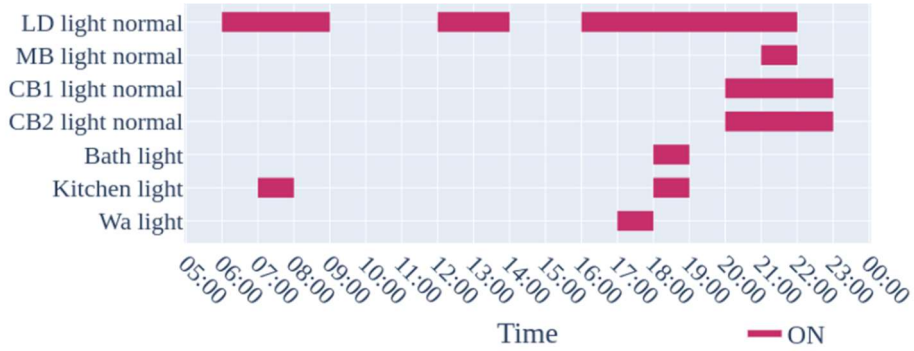

Figure 6.10: Daily lighting usage schedule

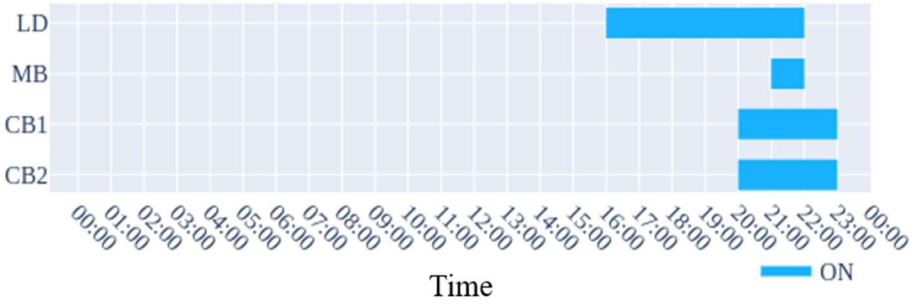

Figure 6.11: Daily cooling usage schedule

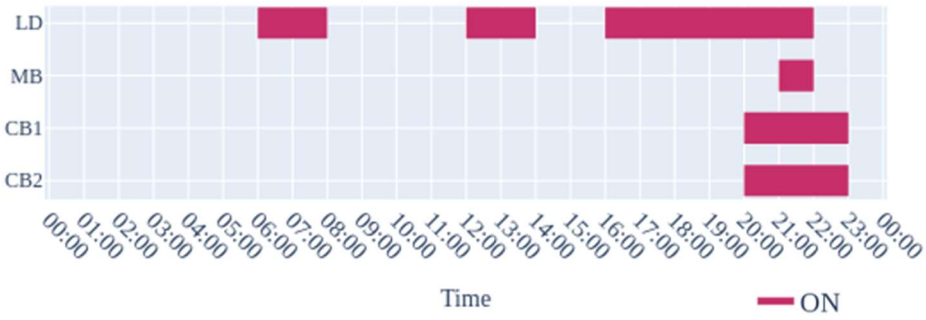

Figure 6.12: Daily heating usage schedule

The total electricity consumption for cooling and heating purposes is estimated about 600 [kWh / year]. Figure 6.16 shows the hourly electricity demand in 2018. The total electricity consumption in this building is estimated about 2308[kWh / year]. It is noted that, the usage of the appliances like vacuum cleaners and washing machines having an unclear usage schedule was not included in the results. According to a survey by the Japanese government agencies, the annual electricity consumption per household in Japan is about 4618 [kWh], and the electricity demand of the main electrical appliances account for 57% of the total which is about 2632 [kWh] [60]. Comparison between this value and the estimated value of total electricity consumption indicates the high accuracy of the results of the simulation model.

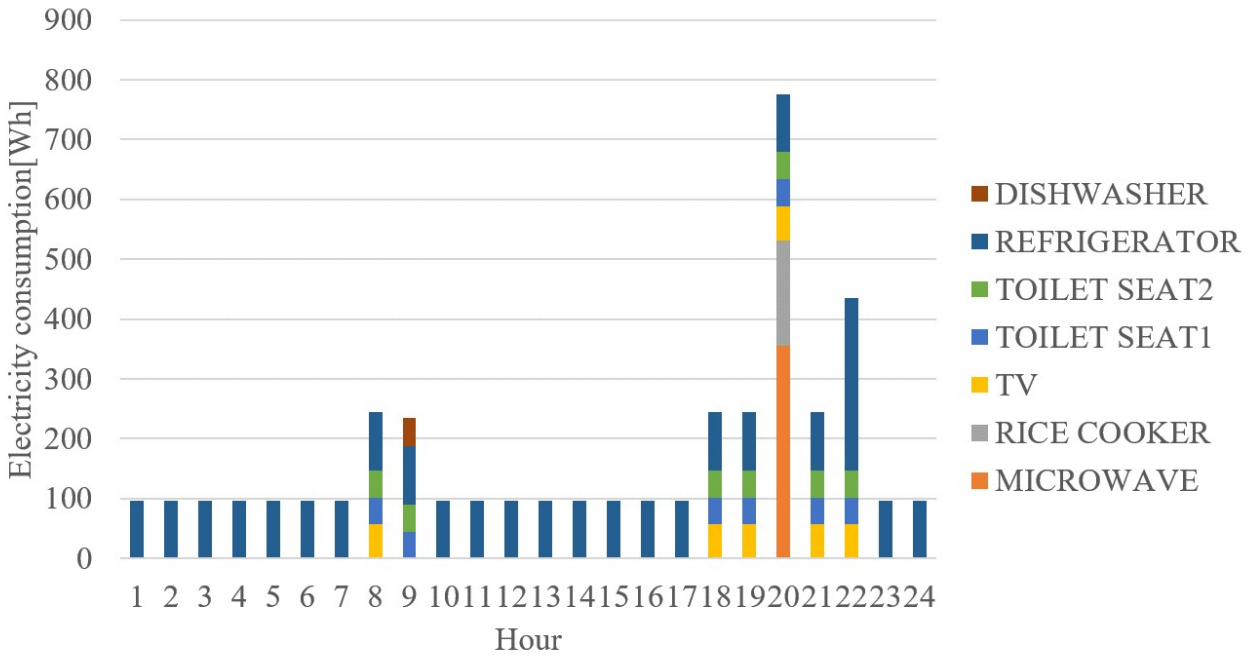

Figure 6.13: Hourly electricity consumption of the electrical appliances

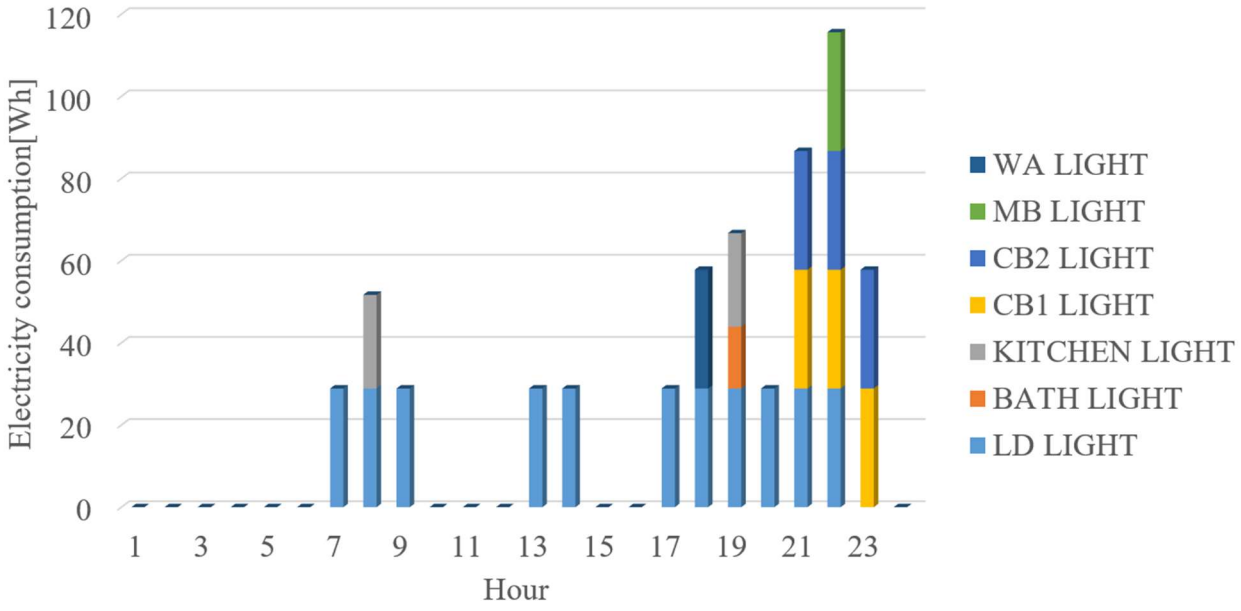

Figure 6.14: Hourly electricity consumption of lighting

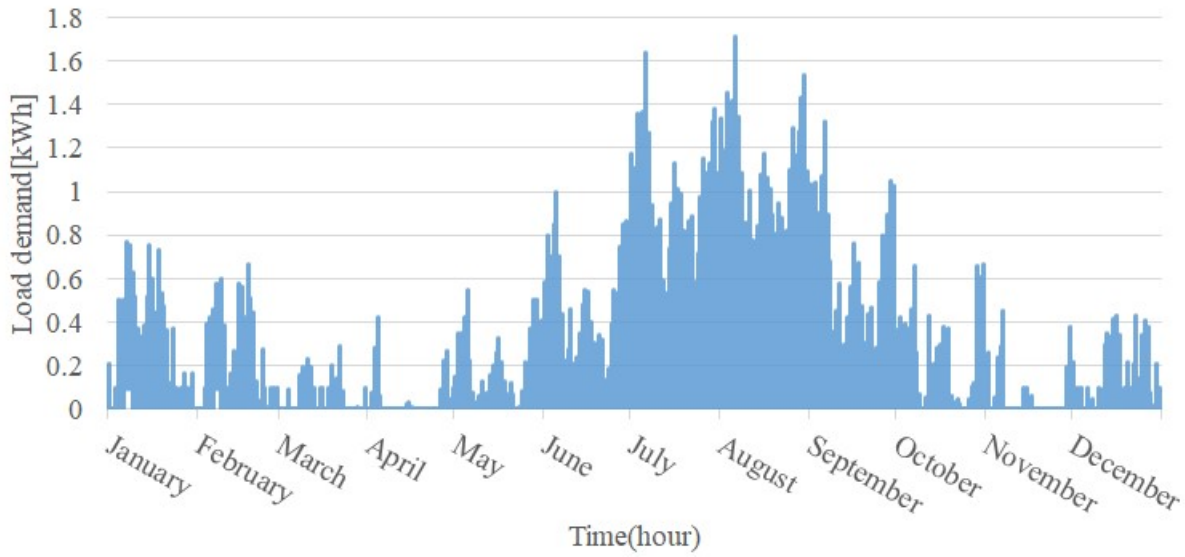

Figure 6.15: Estimated annual electricity consumption of HVAC, using the weather data in 2018

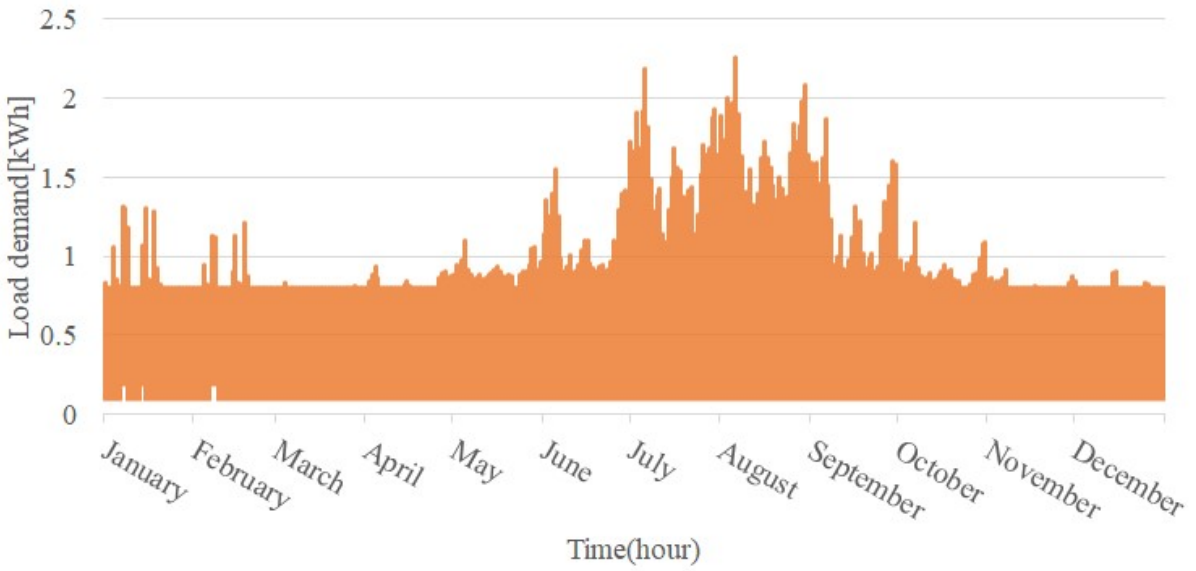

Figure 6.16: Estimated annual electricity demand, using the weather data in 2018

6.3 Optimal design of the proposed Microgrid System

The developed optimization model in Chapter 4 was used to find the optimal size of the proposed microgrid to supply the electricity requirement of the selected residential area. The proposed microgrid system in this study consists of a cluster of micro-sources such as PV panels, wind turbines, batteries, bi-directional converters and diesel generator. The technical specifications of main components of the microgrid system are given in Tables Table 6.7, Table 6.8 and Table 6.9.

Table 6.7: PV initial parameters[39,61,62]

Rated capacity of the PV array power under standard test conditions[kW]	0.245
Solar constant [kW/m2]	1.367
Solar constant [kW/m2]	0.8
Ambient temperature at which the NOCT is defined [˚C]	20
Nominal operating cell temperature [˚C]	44
PV cell temperature under standard test conditions [25˚C]	25
PV cell temperature under standard test conditions [25˚C]	3
Incident solar radiation incident on the PV array [kW/m2]	1
Module Efficiency of PV array [%/˚C]	-0.258
Slope of the surface [˚]	33
Solar absorptance and the solar transmittance [%]	0.194
PV derating factor [%]	0.8
Azimuth of the surface [˚]	0
longitude [˚]	130
latitude [˚]	33
Ground reflectance, which is also called the albedo [%]	0.2
Solar absorptance and the solar transmittance [%]	0.9
Slope of the surface [˚]	33
Azimuth of the surface [˚]	0

Table 6.8: Battery input data[42]

Battery Type	Lead-acid
Nominal cell voltage [V]	12
Nominal capacity[kWh]	1
SOC_{max} [%]	100
SOC_{min} [%]	40
Float life[year]	4
Round-trip efficiency [%]	80

Table 6.9:Wind turbine input data[42,63]

Constant power[kWh]	0.3
Cut-in wind speed[m/s]	3
Cut out wind speed[m/s]	20
Height[m]	40
Reference height[m]	10
Air density on sea surface[kg/m3]	1.225

As mentioned earlier in Chapter 3, wind power is calculated using the MSL and wind speed at hub height as inputs as shown in Figures Figure 6.17 and Figure 6.18. Figure 6.6 shows the measured wind speed at a height of 10 meters in Dazaifu city, 2018. Figure 6.18 shows the wind speed corrected value,

applying equation (1) to the wind speed at the hub height. Potential power generation per unit of wind generators is calculated as shown in Figure 6.19.

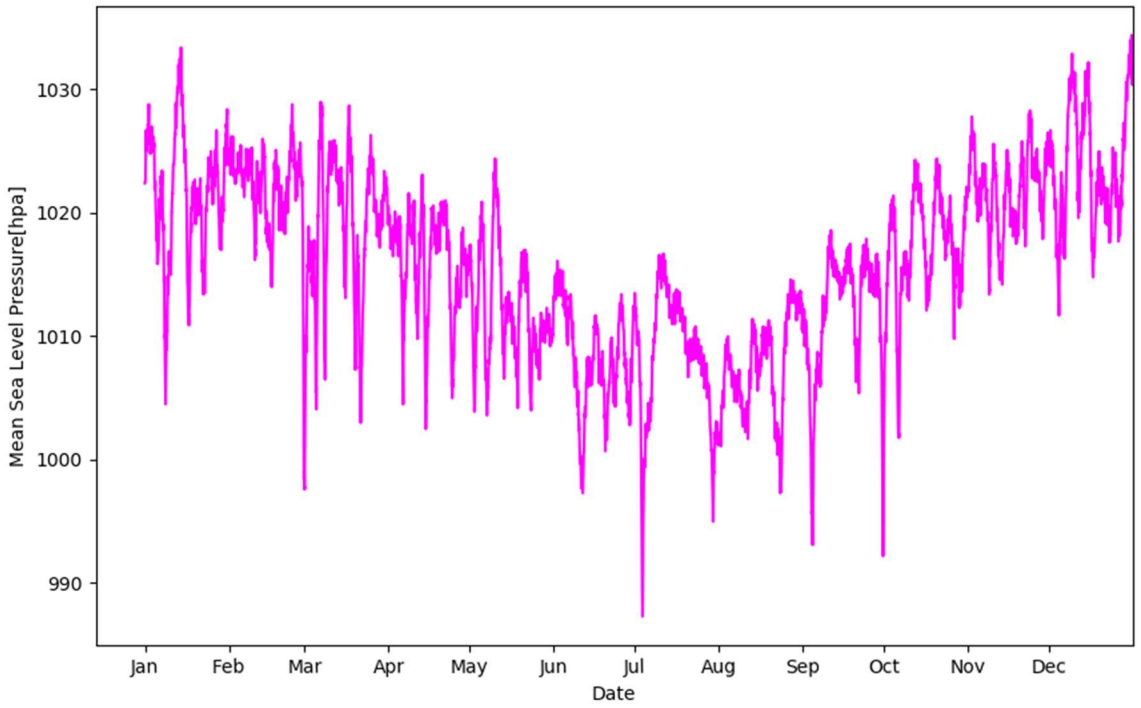

Figure 6.17: Input mean sea level pressure in 2018

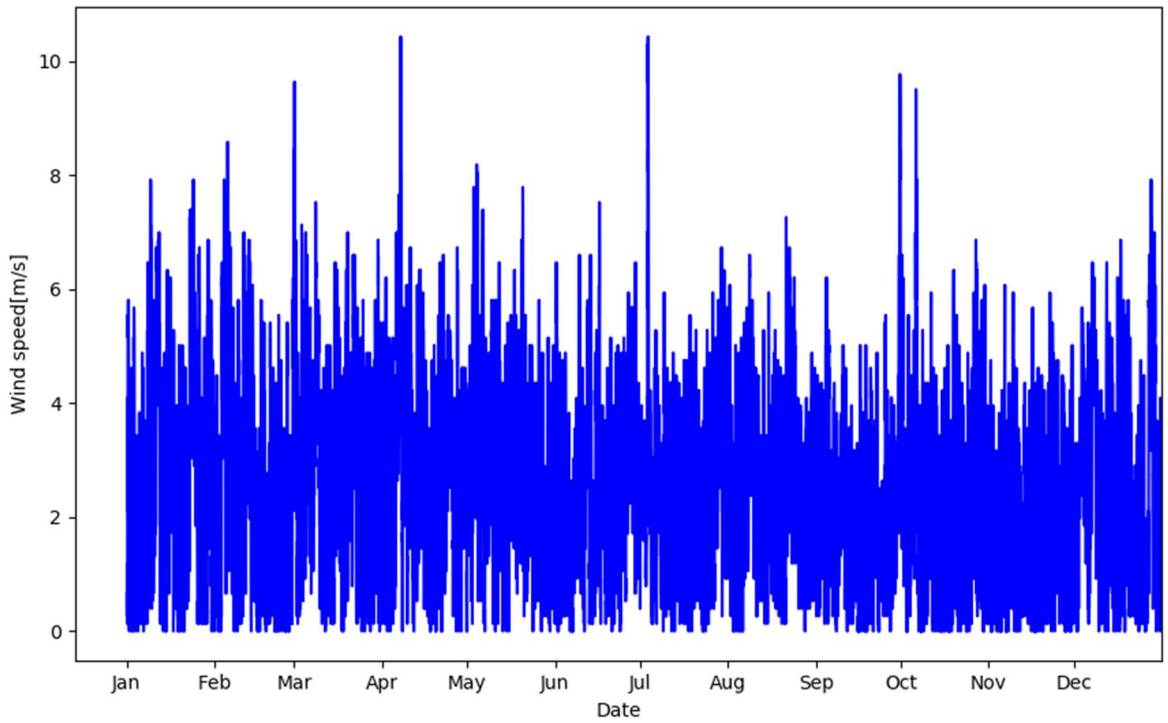

Figure 6.18: Wind speed in 2018 (H=40m, α=0.2)

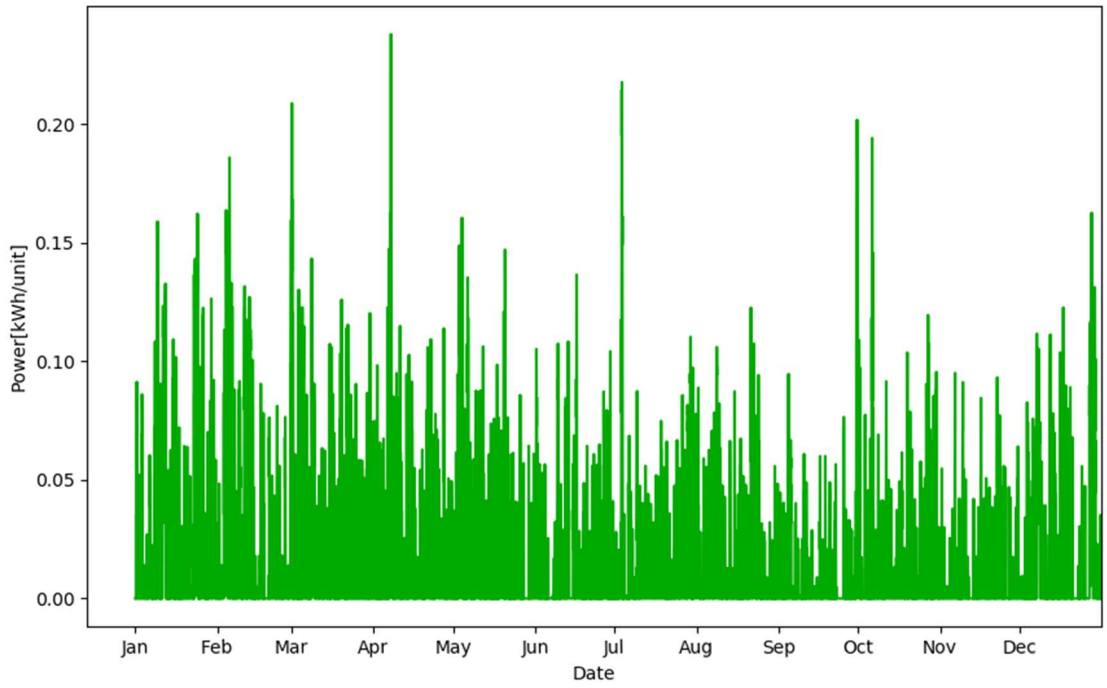

Figure 6.19: Estimated wind turbine electricity generation per unit in 2018

On the other hand, PV output power is calculated using cell temperature and solar radiation as input. Figure 6.5 shows input of radiation. Figure 6.20 shows the input Fukuoka city temperature. The cell temperature calculated based on this value is as shown in Figure 6.20. Finally, Figure 6.21 shows the calculated PV gereration in 2018.

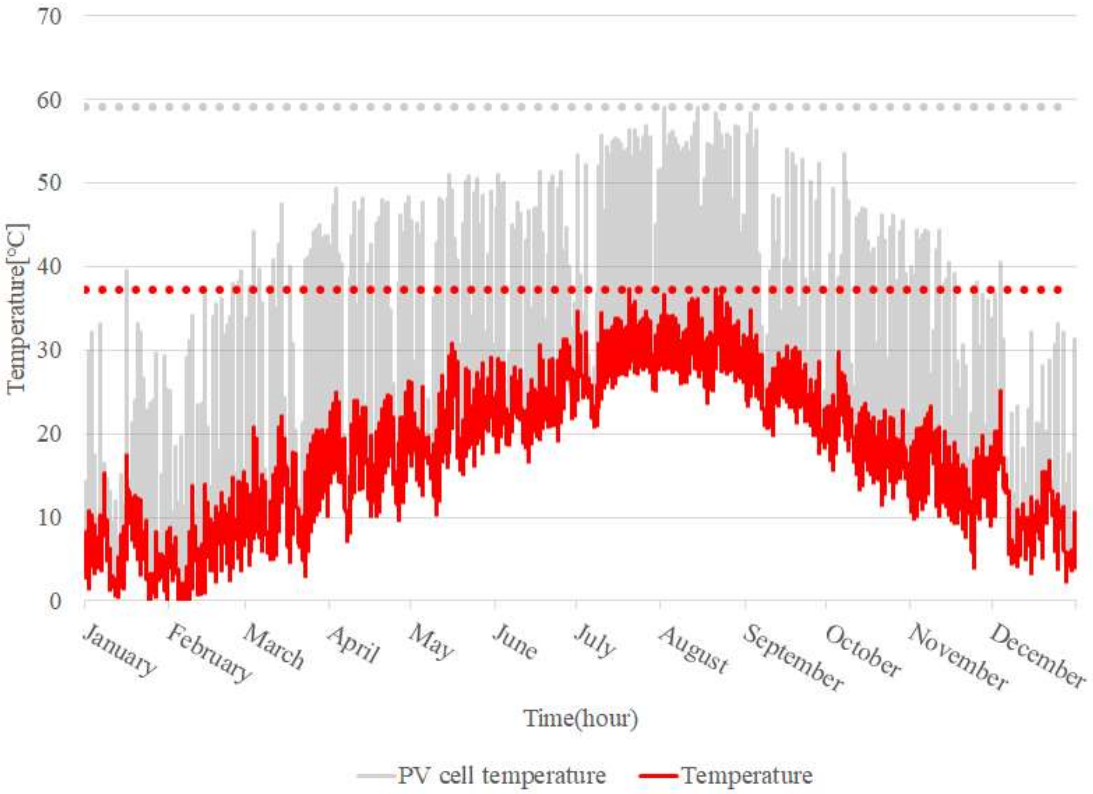

Figure 6.20: Comparision between cell and ambient temperatures

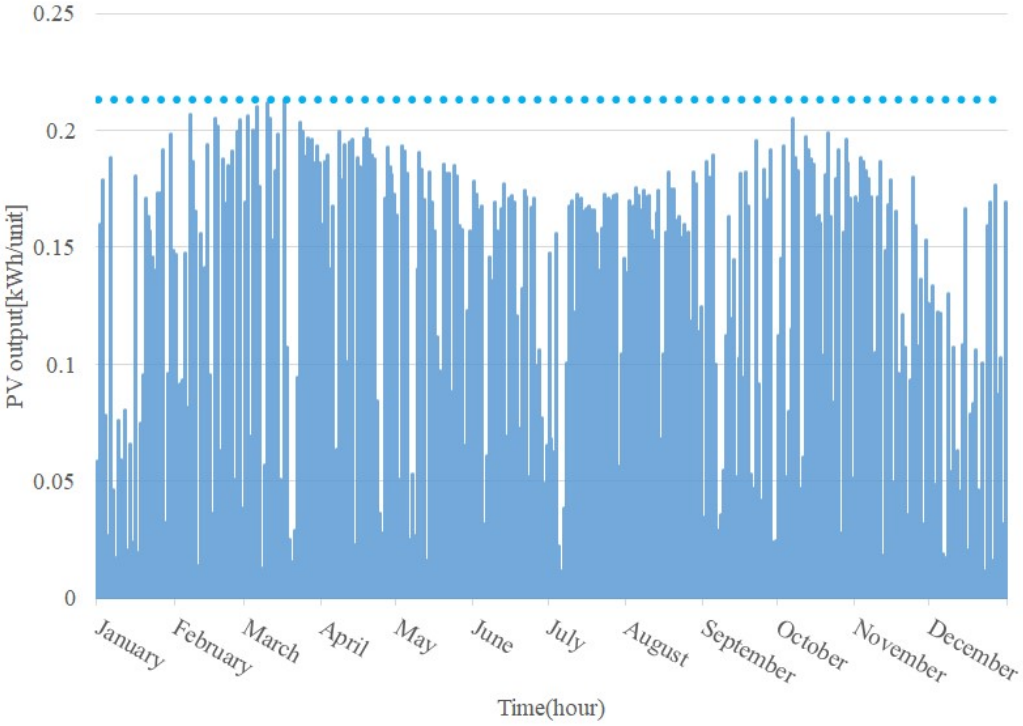

Figure 6.21: PV electricity generation per unit in 2018

Table 6.10 shows the cost analysis of the proposed system. The optimal size and cost of each component are given in Table 6.11. The total cost of the proposed system is estimated about 4.56 million JPY. Figure 6.22 depicts how PSO approach was updated and converged to find the minimum total cost of the system. Figure 6.23 shows the electricity supply mixof the proposed system. As it can be observed from Figure 6.24, the battery storage represents the largest share in total cost of the system, followed by the solar panels and diesel generator. Figure 6.25 shows the LCOE of the proposed system is estimated at 95.3 JPY/kWh which is much higher than the average electricity tariff in Japan (22 JPY/kwh). Figure 6.26 shows the PSO process through the swarms' motion in different iterations from 0 to 100. It can be seen that particles (PV, battery and wind) fly from random initialization toward the particle best and global best so that all the particles converge to one point which is called Global best. Since the optimal combinations can be located in some far points from each other with the same fitness value and different configurations in the objective domain, designing such systems is a complex task. Nevertheless, the particles become very close to each other after 100 iterations and the best combination is identified.

Table 6.10: Cost table[41,42,64]

	Capital cost [JPY/kW]	Replacement cost [JPY/kW]	O&M cost [JPY/KW]	Fuel cost [JPY/KW]	Lifetime
WG	253000	165000	220	0	20 years
PV	553000	553000	1100	0	20 years
Diesel	33611	33611	9	129	15000h
Battery	13640	13640	1100	0	4 years
Converter	13970	13970	110	0	20 years

Figure 6.27 shows the monthly total electricity generation by each component. Figure 6.28 shows the monthly electricity which was used to meet the load requirement. In summer and winter, the amount of

power generated from the diesel generator is higher than the other seasons (Figure 6.29). Figure 6.30 shows the battery charge and discharge situations in each month.

Table 6.11: Result of each component

	PV	WG	Battery	Diesel	Converter
Optimal capacity[kW]	2.65	2.01	14.86	3.6	2.8
Cost [10,000JPY]	152.3	51.9	134.0	102.	4.6
Cost ratio [%]	37.1	9.0	28.8	24.1	1.1

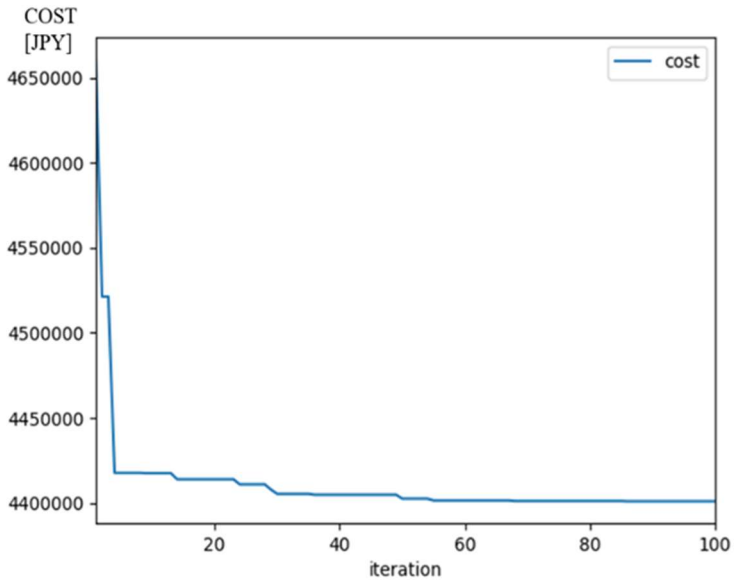

Figure 6.22: Total cost in each iteration

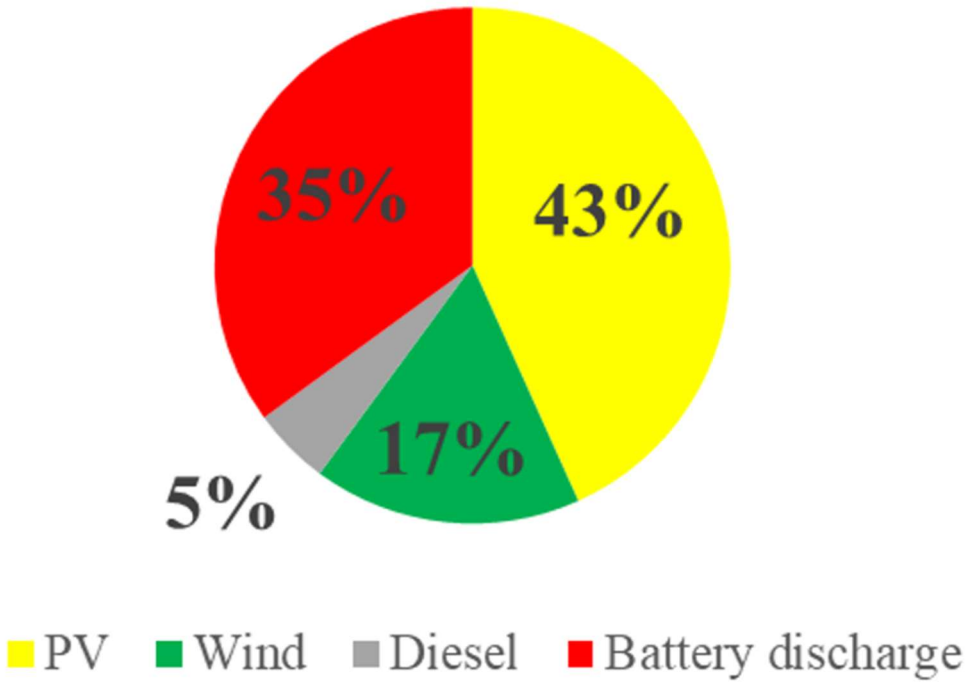

Figure 6.23: Electricity supply mix

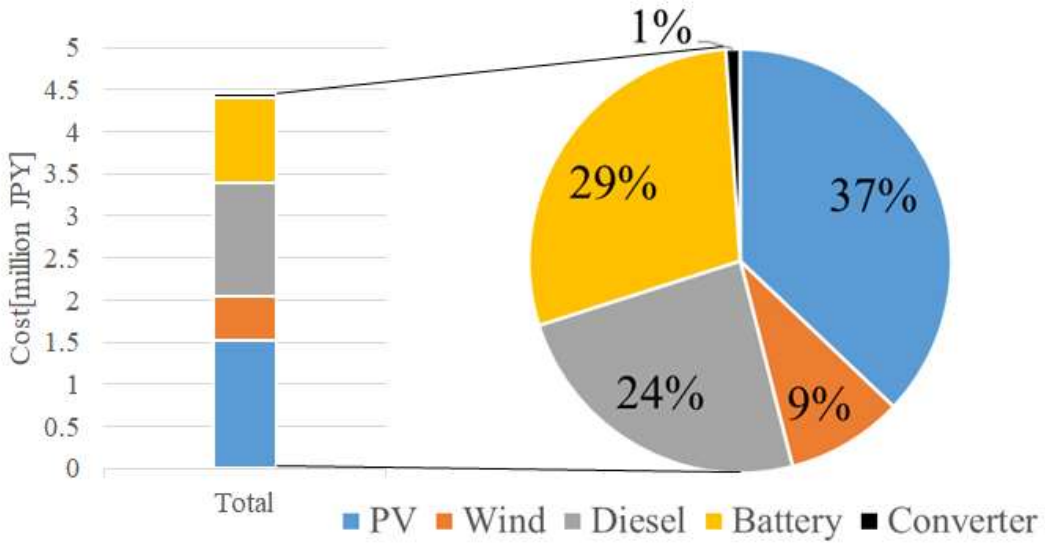

Figure 6.24: Breakdown of costs for each component

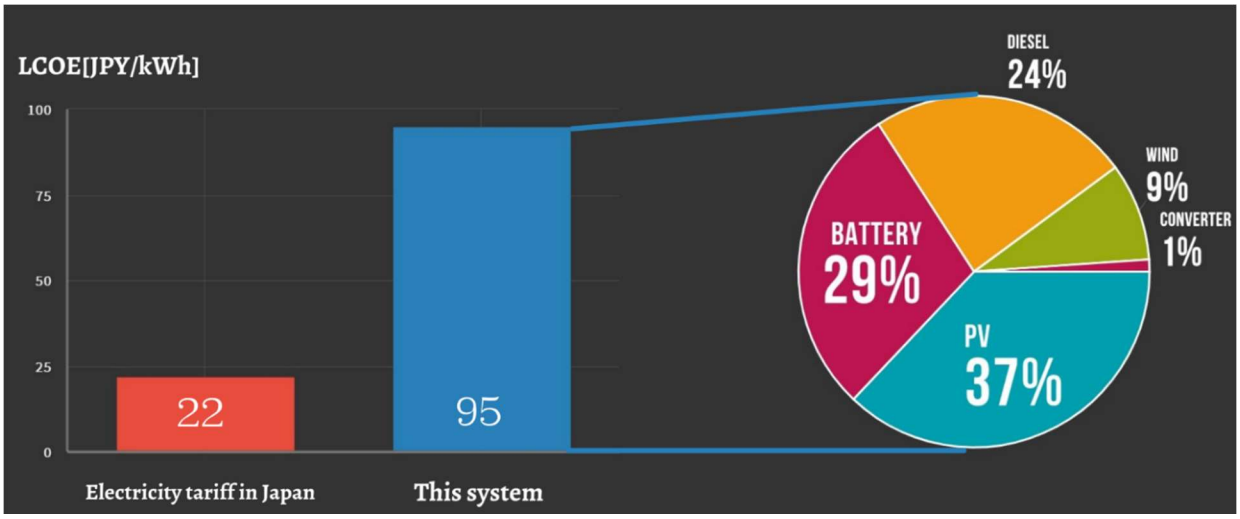

Figure 6.25: Comparision between Erectricity tariff in Japan and LCOE of this system

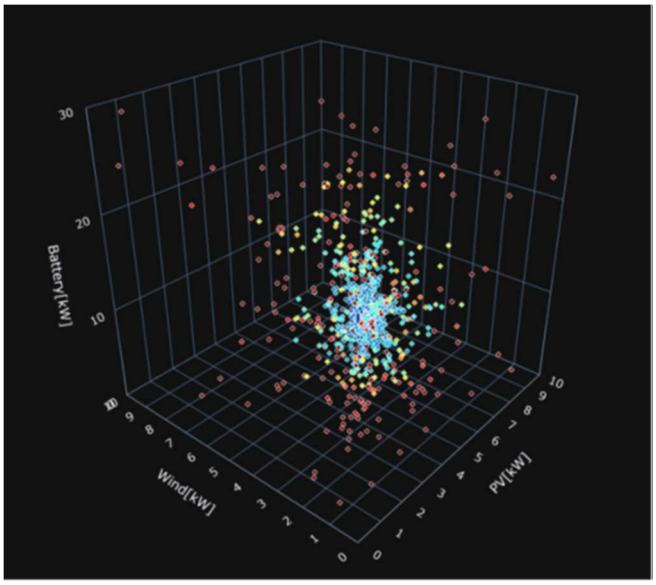

Figure 6.26: The particle positions in each time step based on the PSO algorithm used in this research

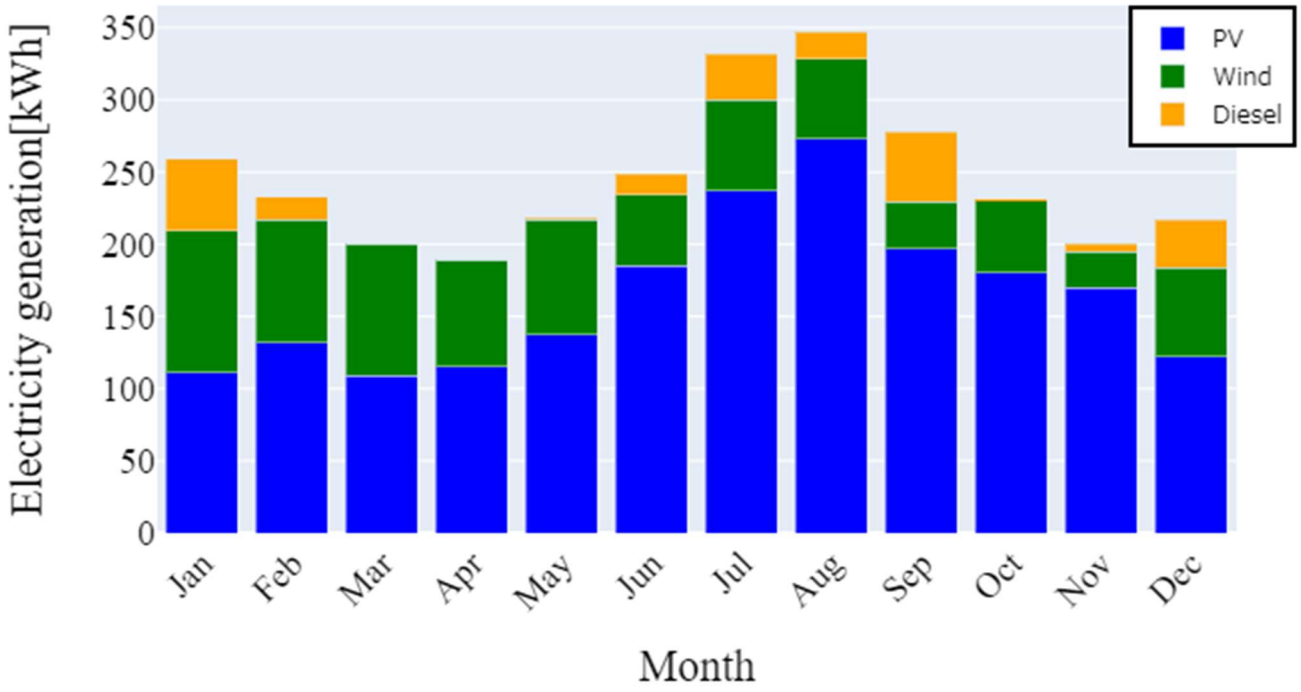

Figure 6.27: Monthly total electricity generation by each component

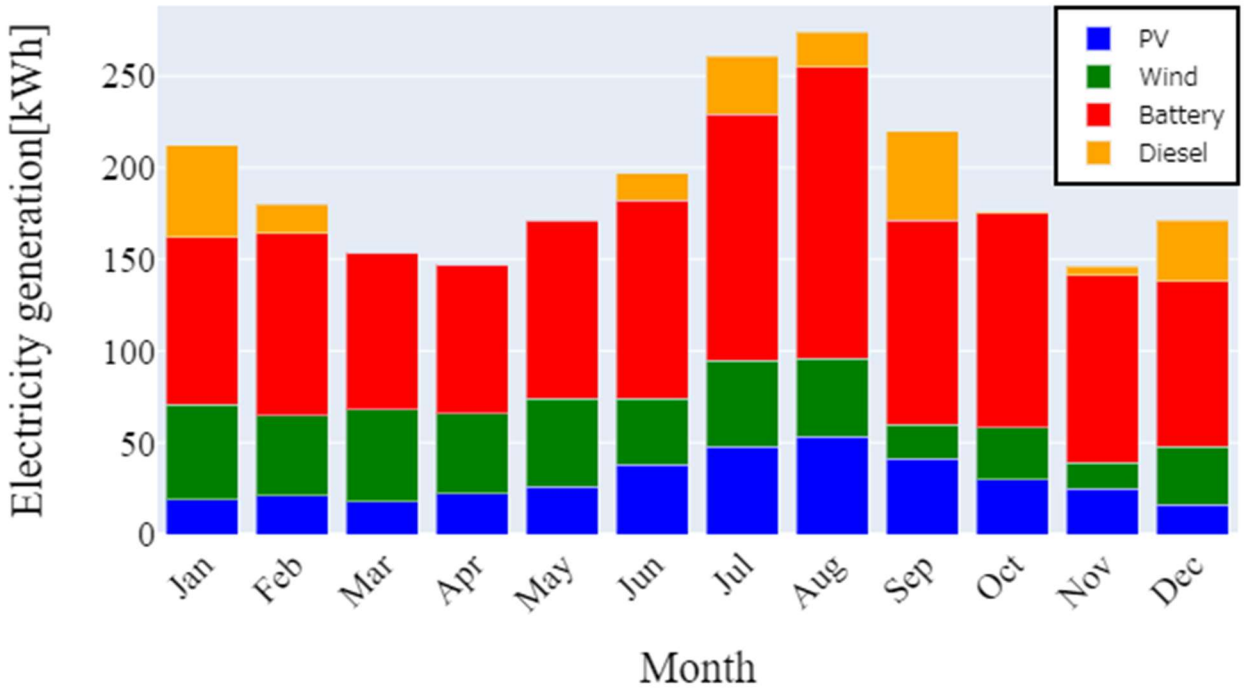

Figure 6.28: Monthly electricity used to meet the load requirement

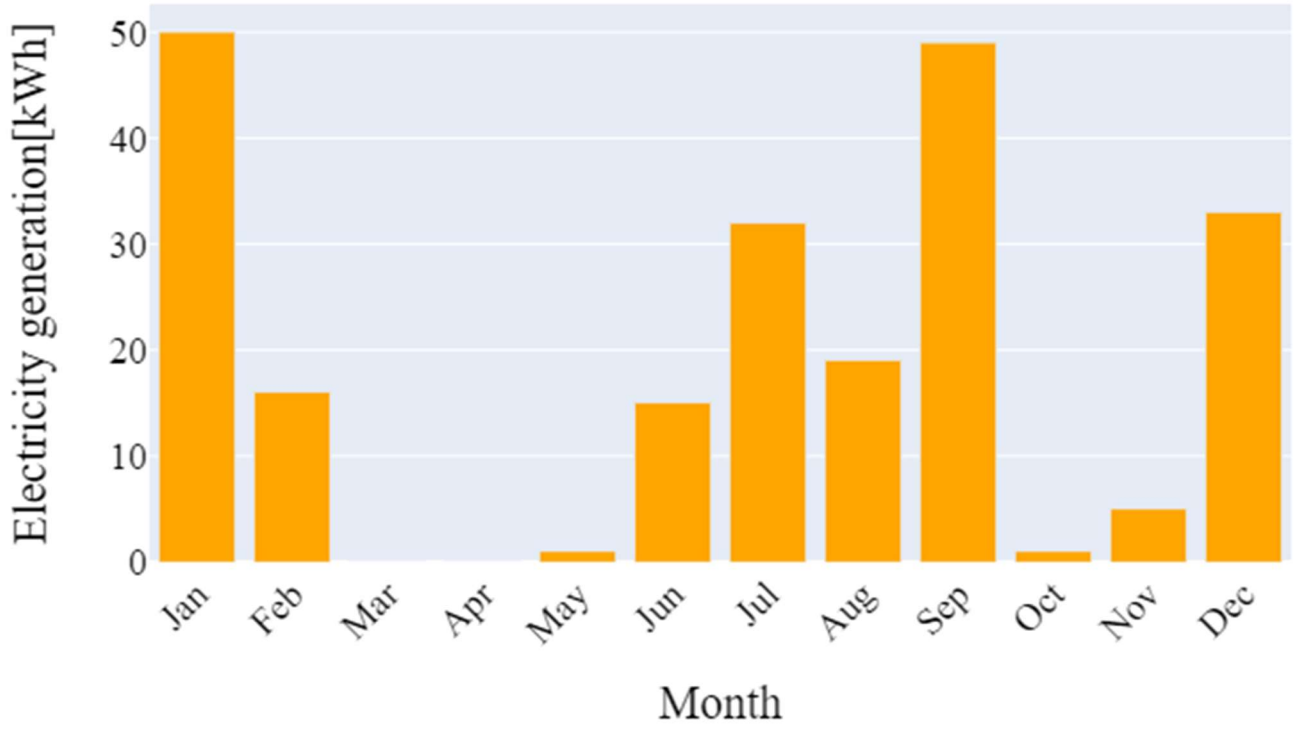

Figure 6.29: Monthly diesel electricity generation using the weather data in 2018

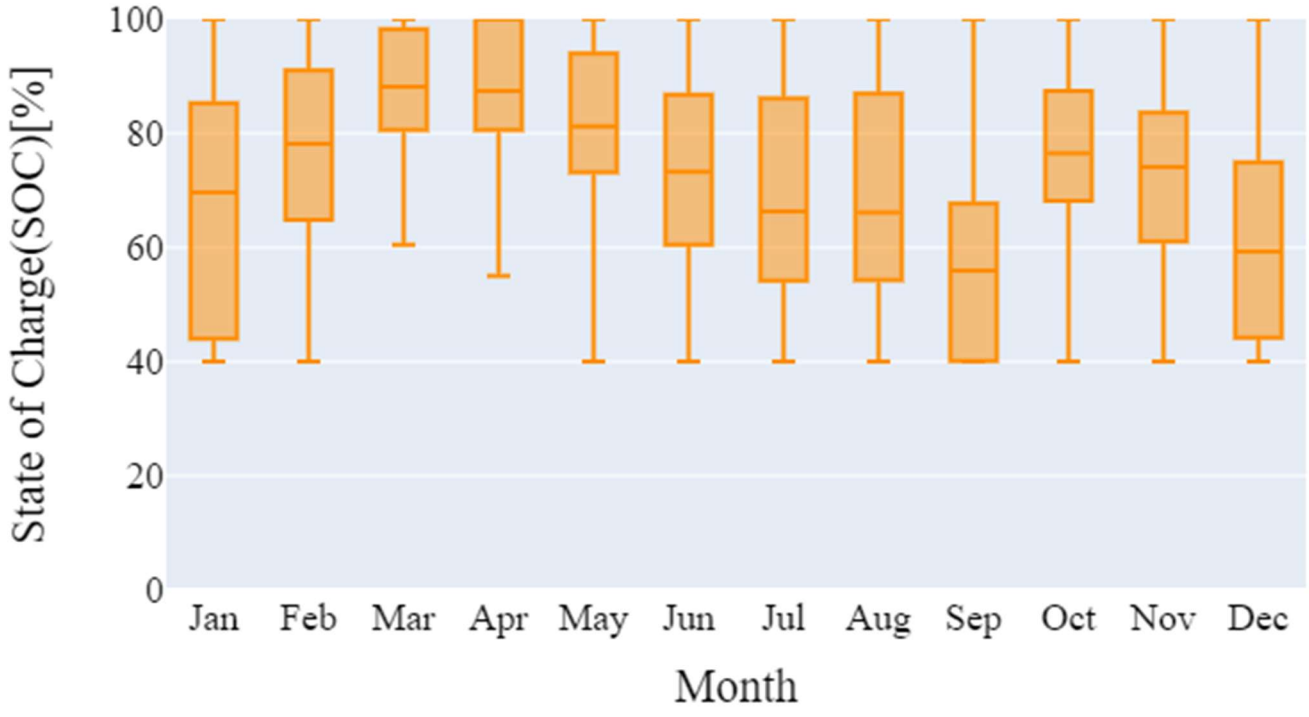

Figure 6.30: SOC of battery storage iun the proposed system

Parallel coordinates are a common way of visualizing high-dimensional geometry and analyzing multi-variate data. Figure 6.31 and Figure 6.32 demonstrates the pathways towards reaching the optimal solution by each component based on satisfy the minimum total cost of the system. It can be seen that, the size of the diesel generator increases, if the size of PV panels or battery decreases which will result in increasing the total cost of the system. The energy Sankey diagram which can provides an overview of the main energy flows and how they contribute to the global energy balance of a proposed system is shown in Figure 6.33.It shows that about 80% of the power generated from PV which cannot be used for demand directly will be charged to the battery to be used when the sunshine is not available.

Figure 6.34 represents the weather satellite images in japan which were taken by the weather satellite Himawari-8 at 12:00 on July 3rd in 2018 and 2019. On July 3rd, 2018, Typhoon No. 7 went north over the East China Sea and approached Kyushu, and Fukuoka was taken by strong winds and heavy rain. Therefore, there was insufficient solar electricity generation, but since the strong wind blew in the afternoon, a sufficient amount of electricity was generated by the wind power generator.

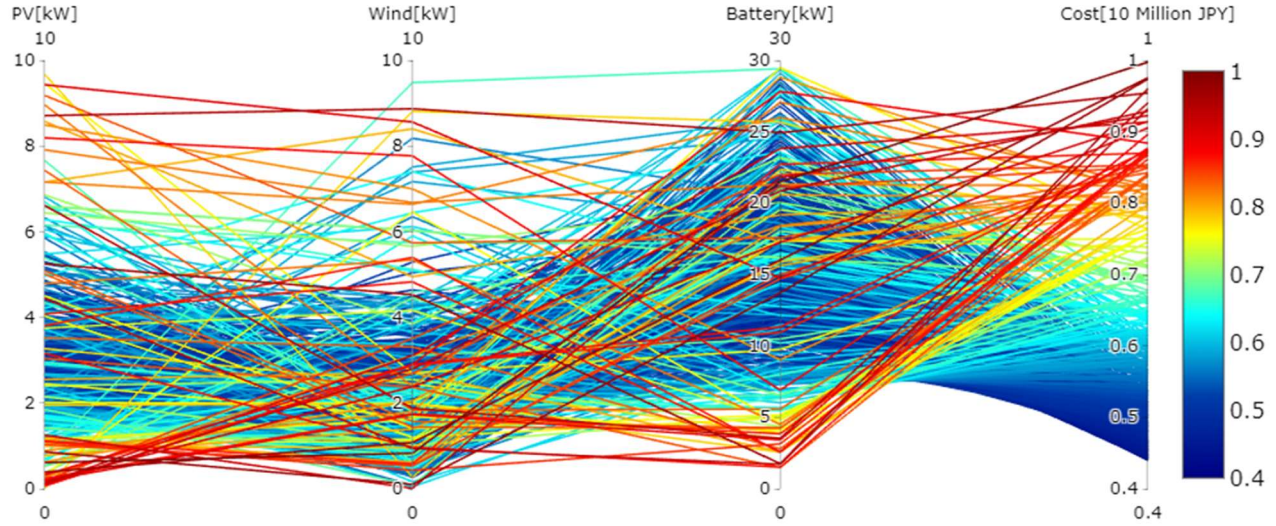

Figure 6.31: Parallel coordinates of all particles in alliterations

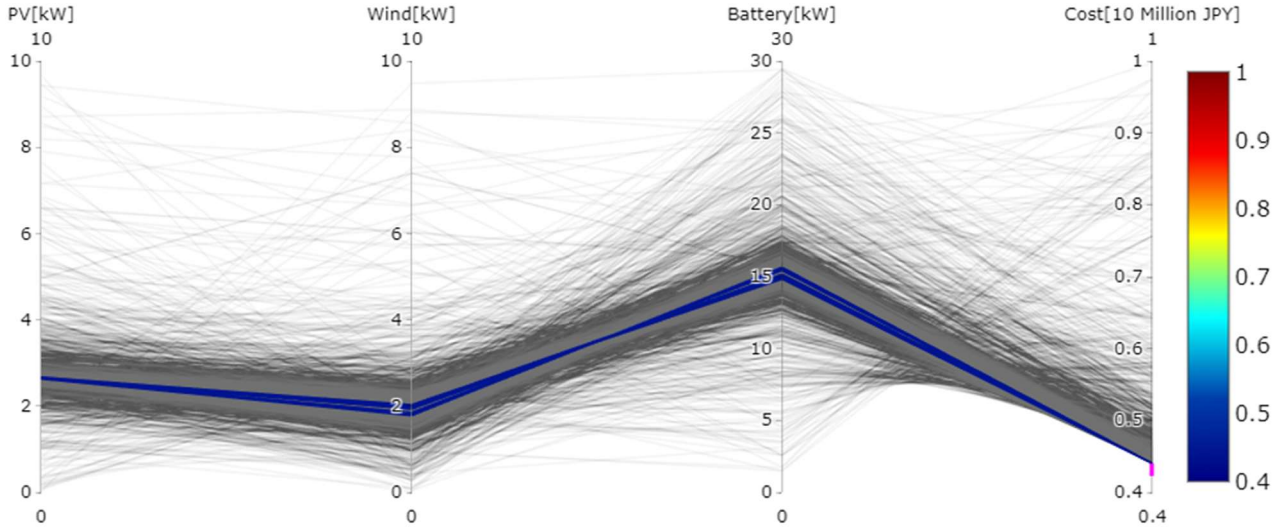

Figure 6.32: Parallel coordinates of the optimal particle

However, on the same day in 2019, Fukuoka was covered with heavy clouds and the average wind speed was very weak at 2-3 [m / s]. Therefore, there was no power generation from the wind turbine in this day. Besides, since the sky had been covered with dark clouds for a long time, there was no sufficient power output from the PV panels which resulted in reducing the SOC of the battery. As shown in Figures Figure 6.39 to Figure 6.41, the diesel generator was used to compensate the shortage of battery discharge. Comparison between the real and forecasting data highlights the remarkable impact of weather conditions on power generation from the proposed microgrid. Day ahead forecasting of the weather data will help in managing the battery operation through monitoring its SOC condition and lowering the usage of diesel generator in order to reduce its cost and environmental impacts on the system. Finally, Figures Figure 6.42 to Figure 6.44 represents a pie chart showing the percentage of power used by each component over the year.

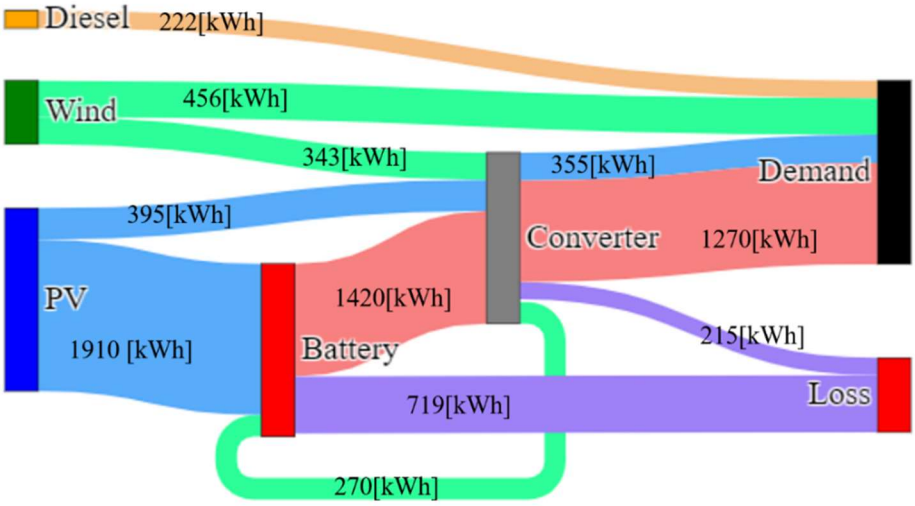

Figure 6.33: Energy flow Sankey diagram in the proposed microgrid

Table 6.12: Summary of the meteorological data used for comparing the result of the proposed microgrid simulation difference between real data and forecast data

Name	Start date	End date	Data type	Correction
2018 July real data	2018/1/1	2018/12/31	Measured by AMeDAS	×
2019 July real data	2019/1/1	2019/11/3	Measured by AMeDAS	×
2019 July forecast data	2019/1/1	2019/11/3	Forecast value of JMA	○

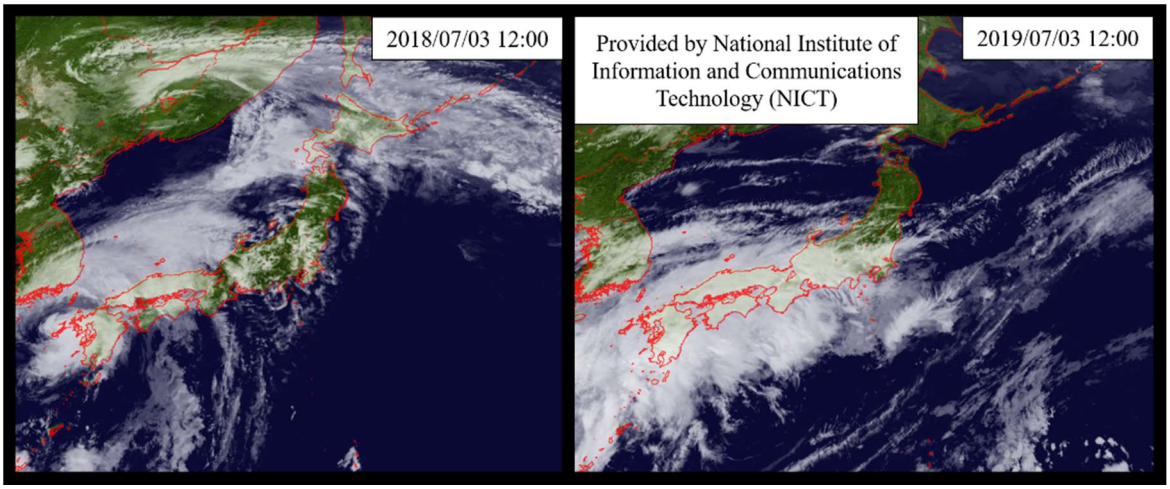

Figure 6.34: Comparison of satellite images between 2019/07/03 12:00 and 2018/07/03 12:00

Real data in 2018

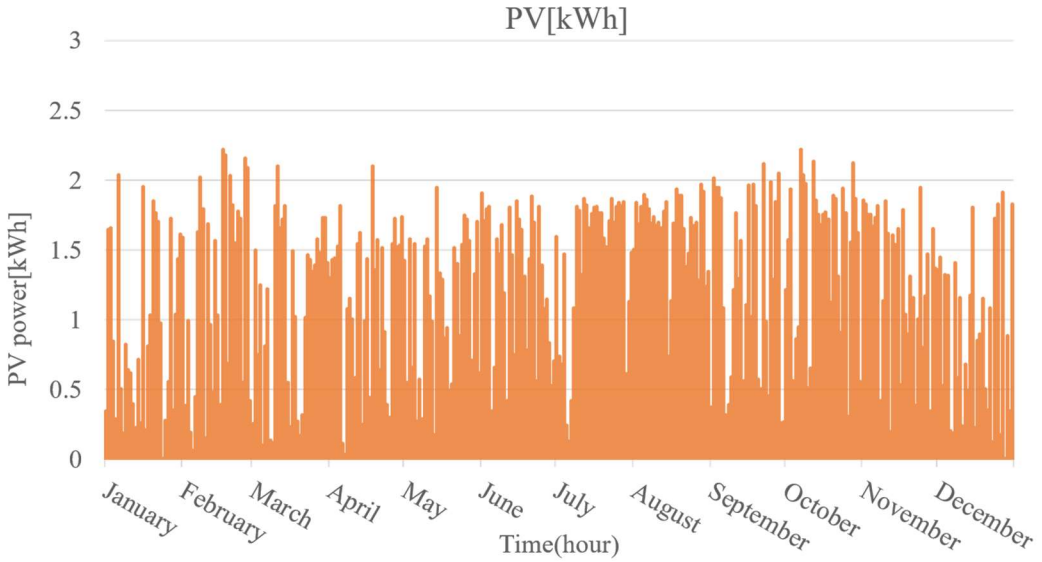

Real data in 2019

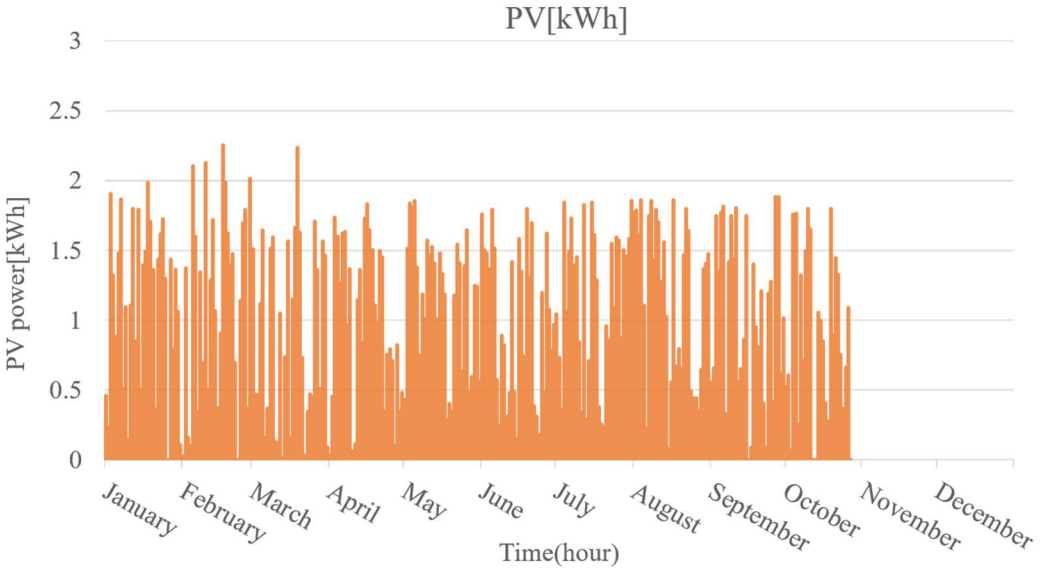

Forecast data in 2019

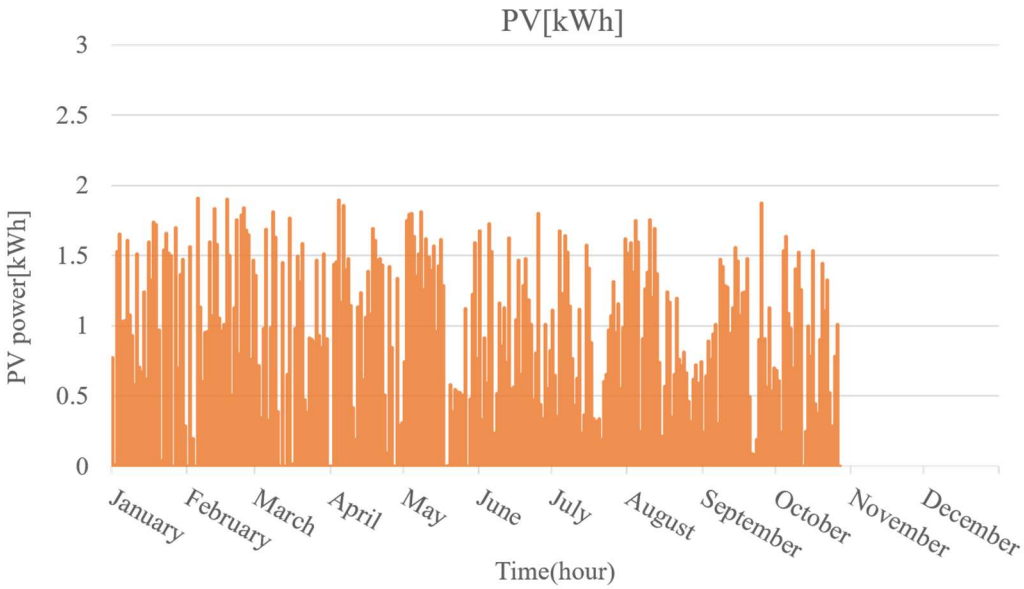

Figure 6.35: Annual hourly electricity generation of PV

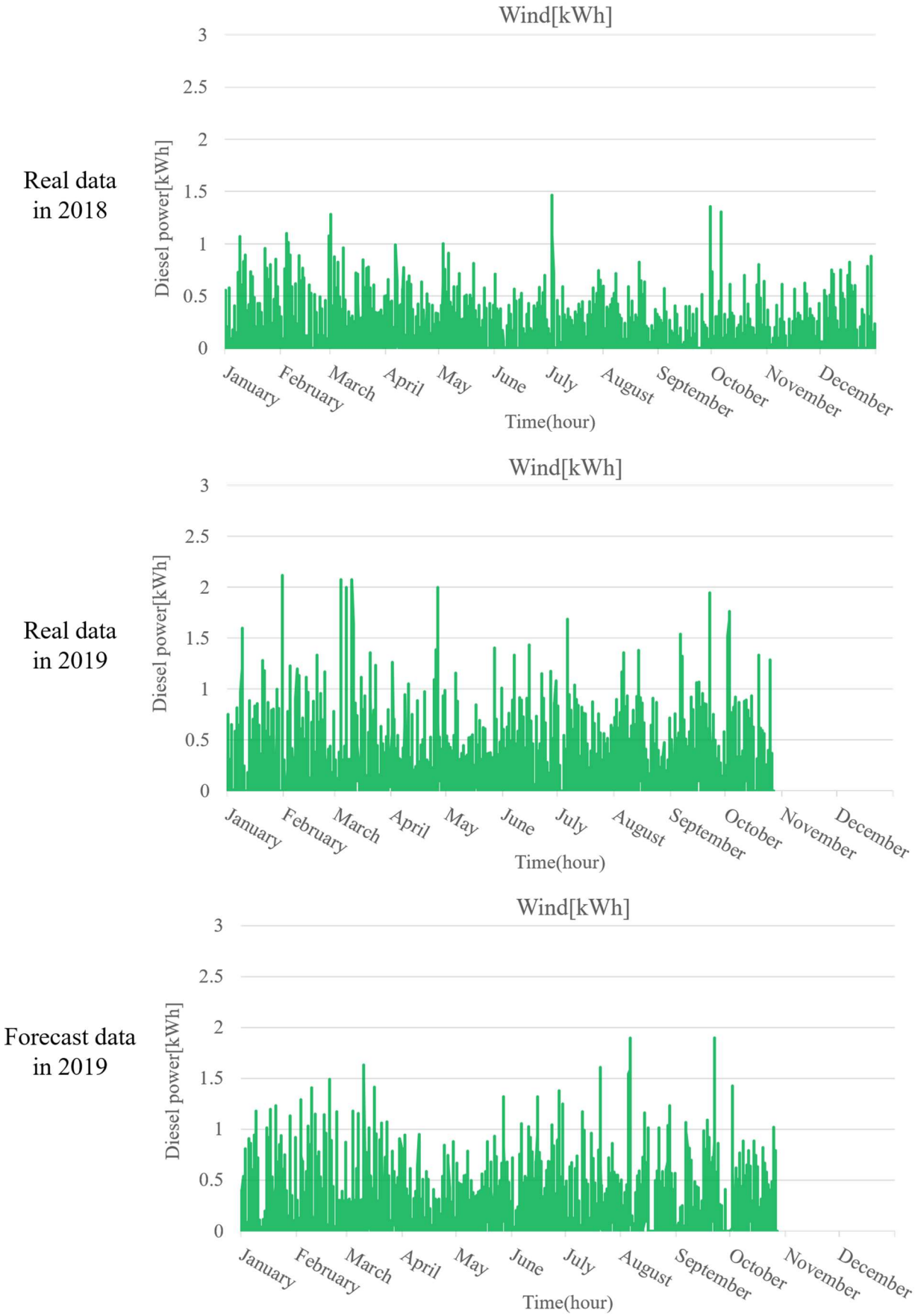

Figure 6.36: Annual hourly electricity generation of wind

Real data in 2018

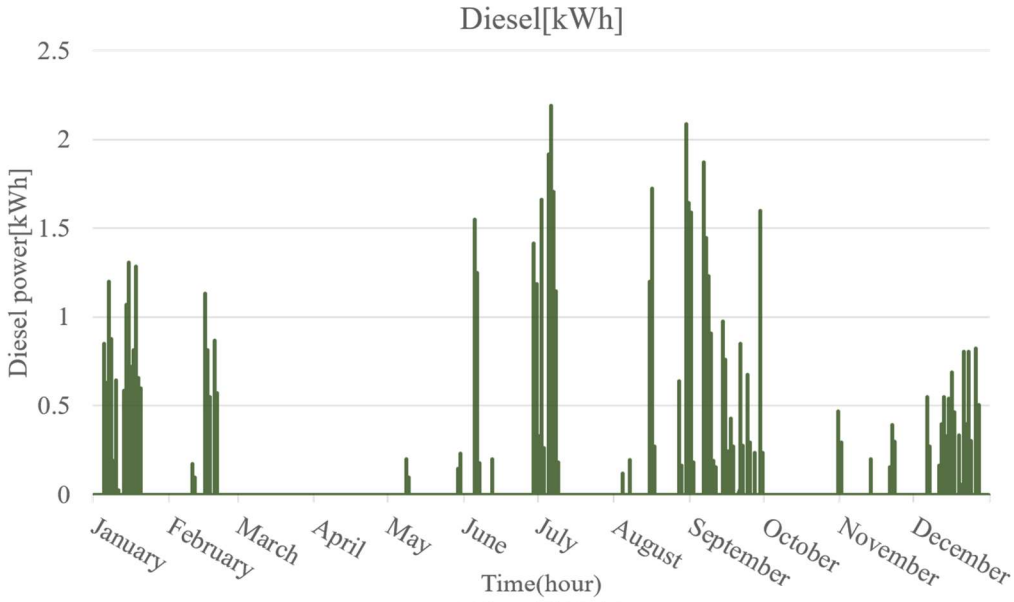

Real data in 2019

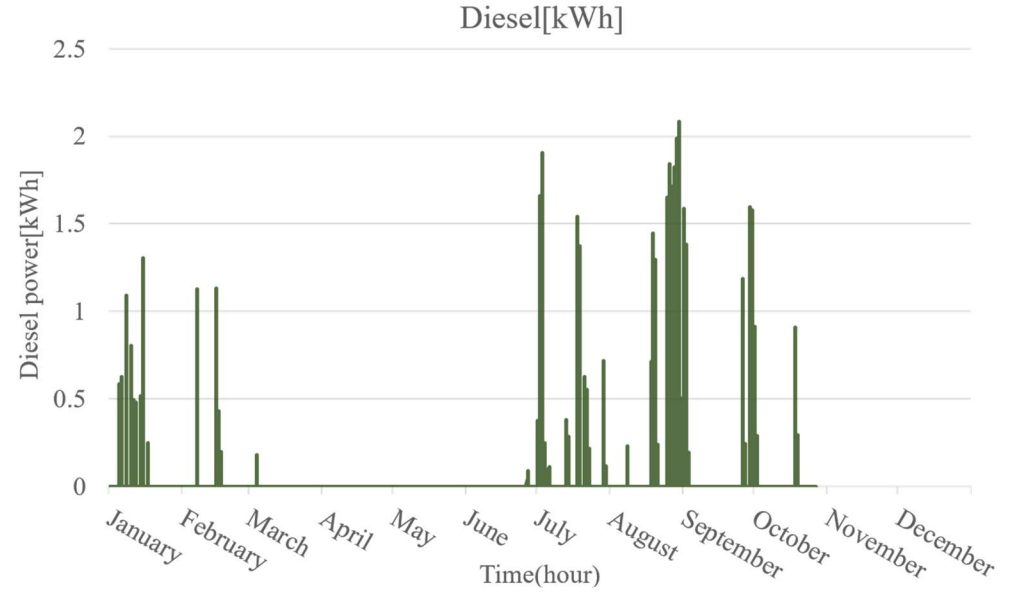

Forecast data in 2019

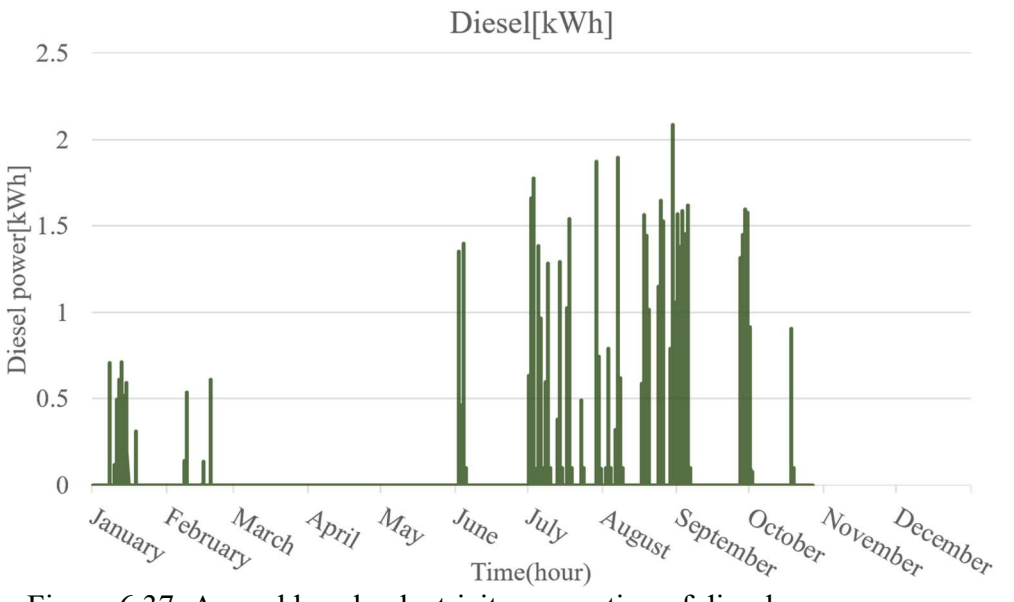

Figure 6.37: Annual hourly electricity generation of diesel

Real data in 2018

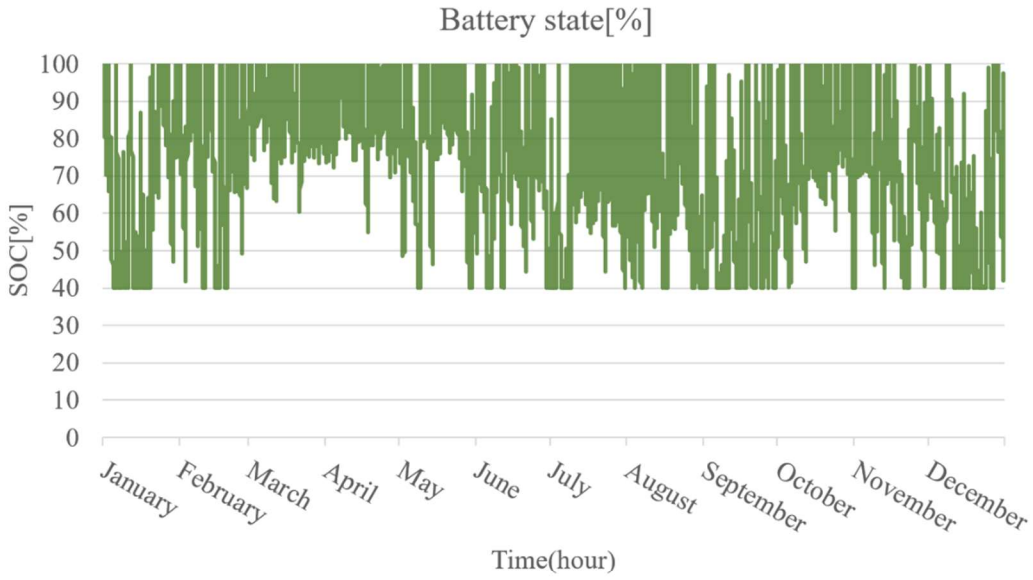

Real data in 2019

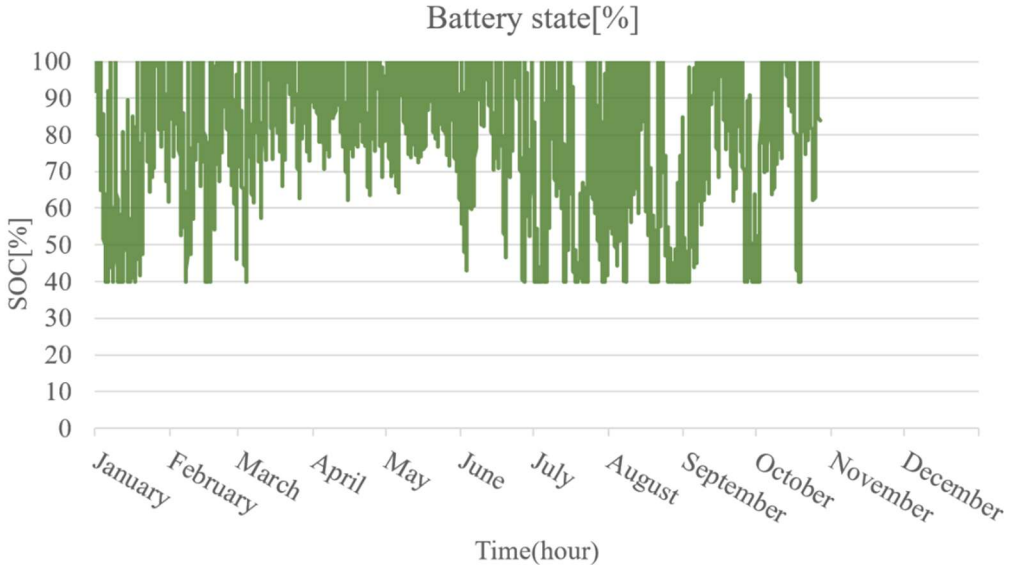

Forecast data in 2019

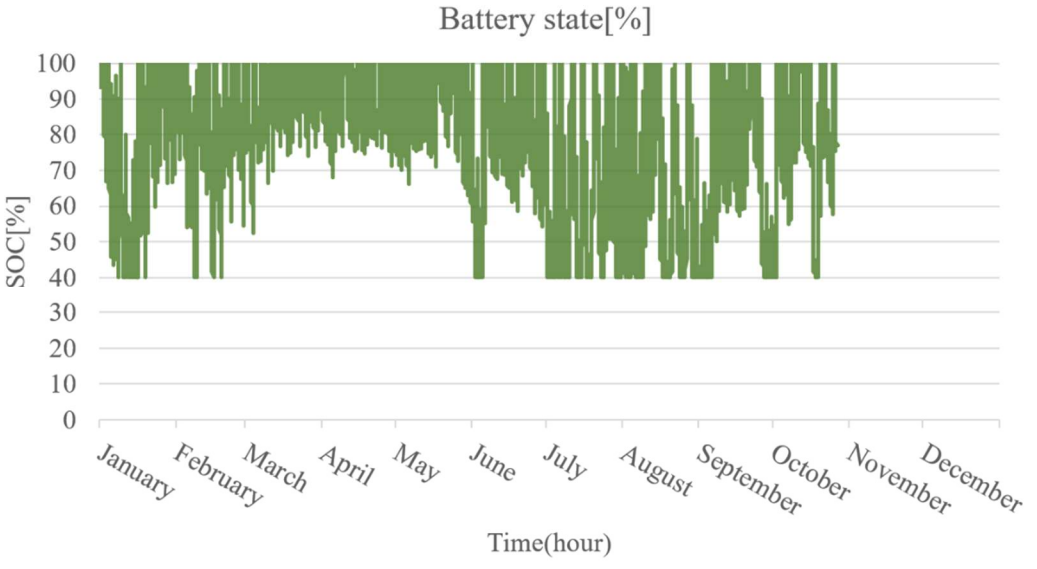

Figure 6.38: SOC of battery storage in the proposed microgrid

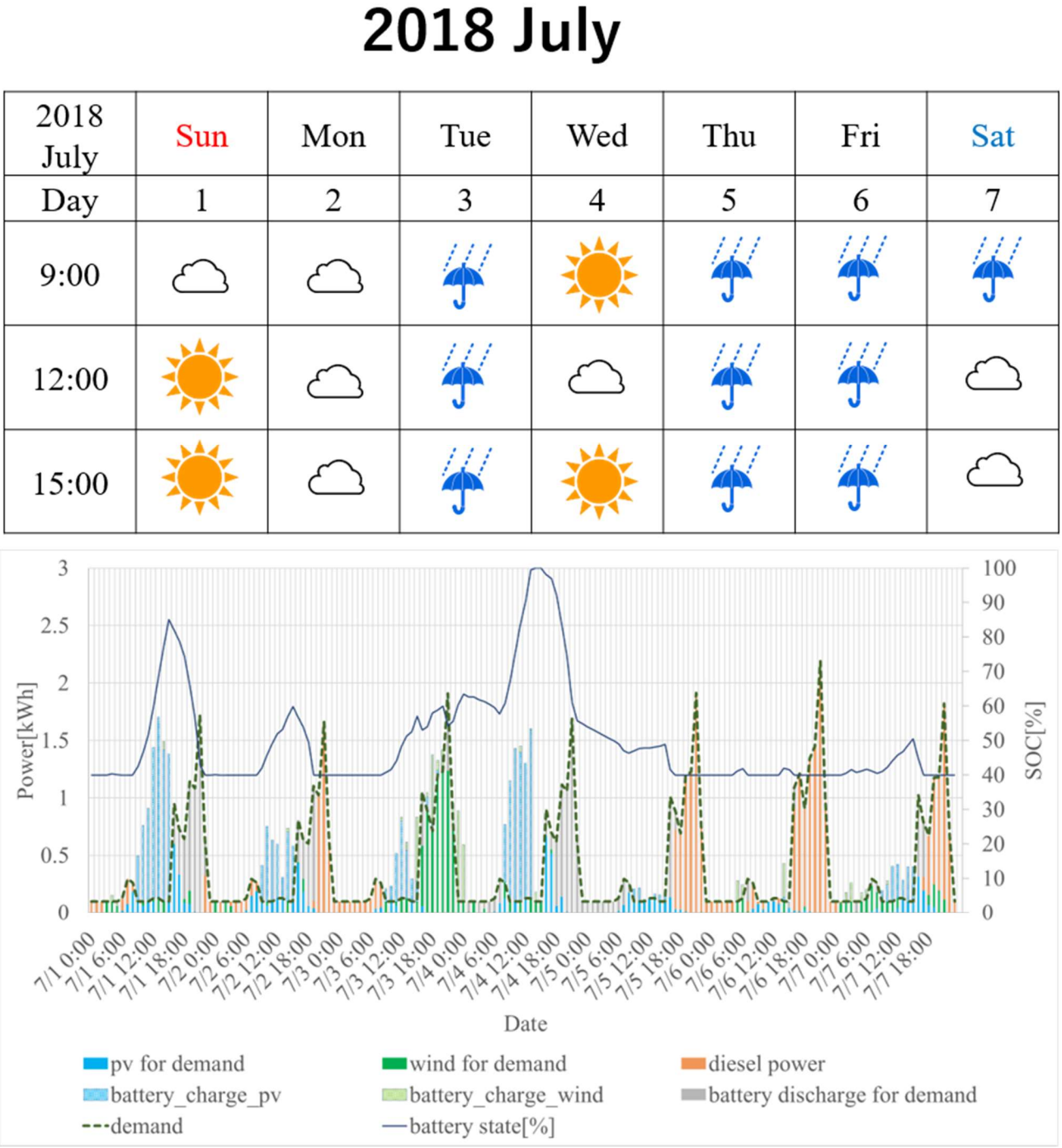

Figure 6.39: Electricity supply mix based on using 2018 real data

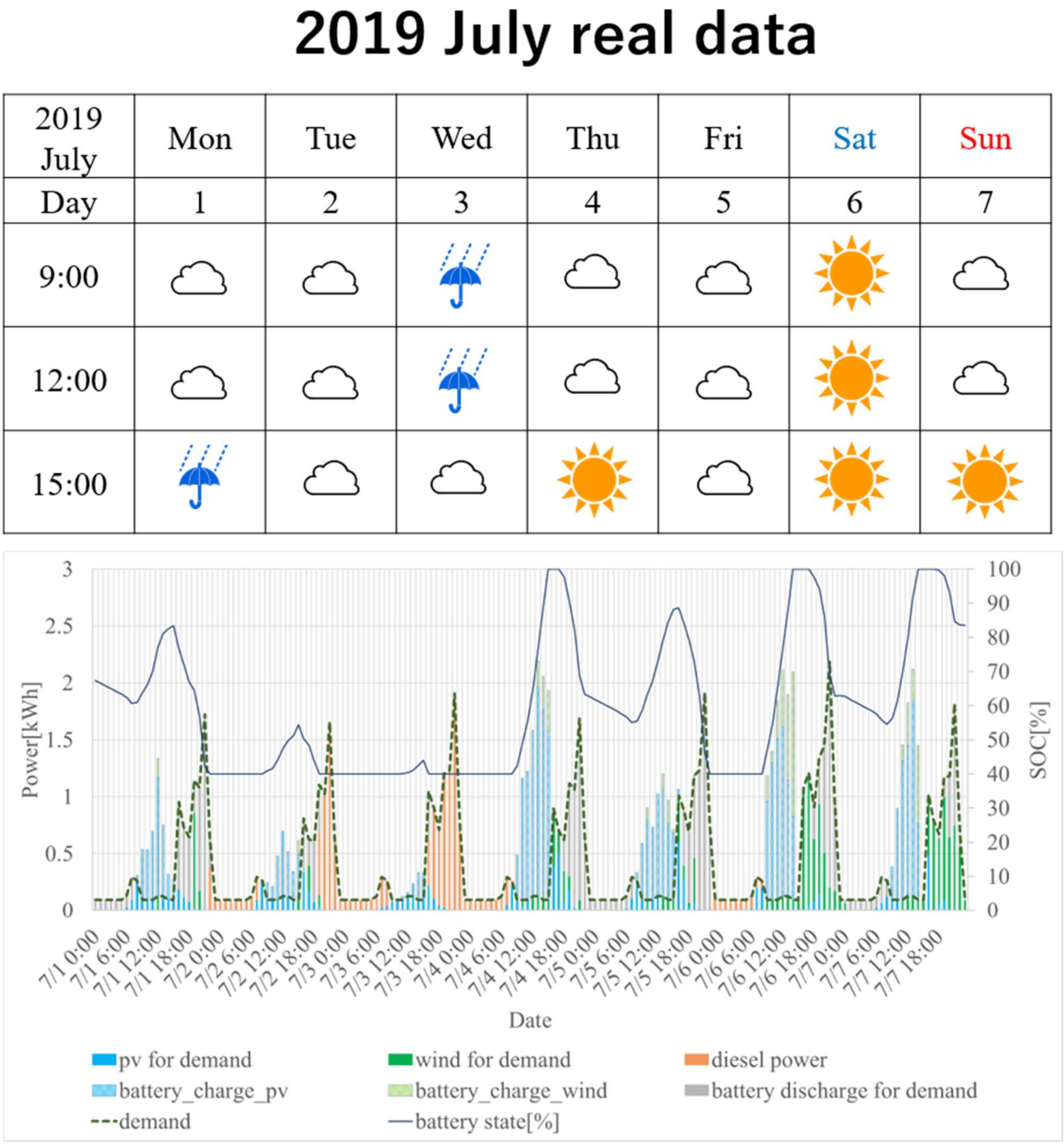

Figure 6.40: Electricity supply mix based on using 2019 real data

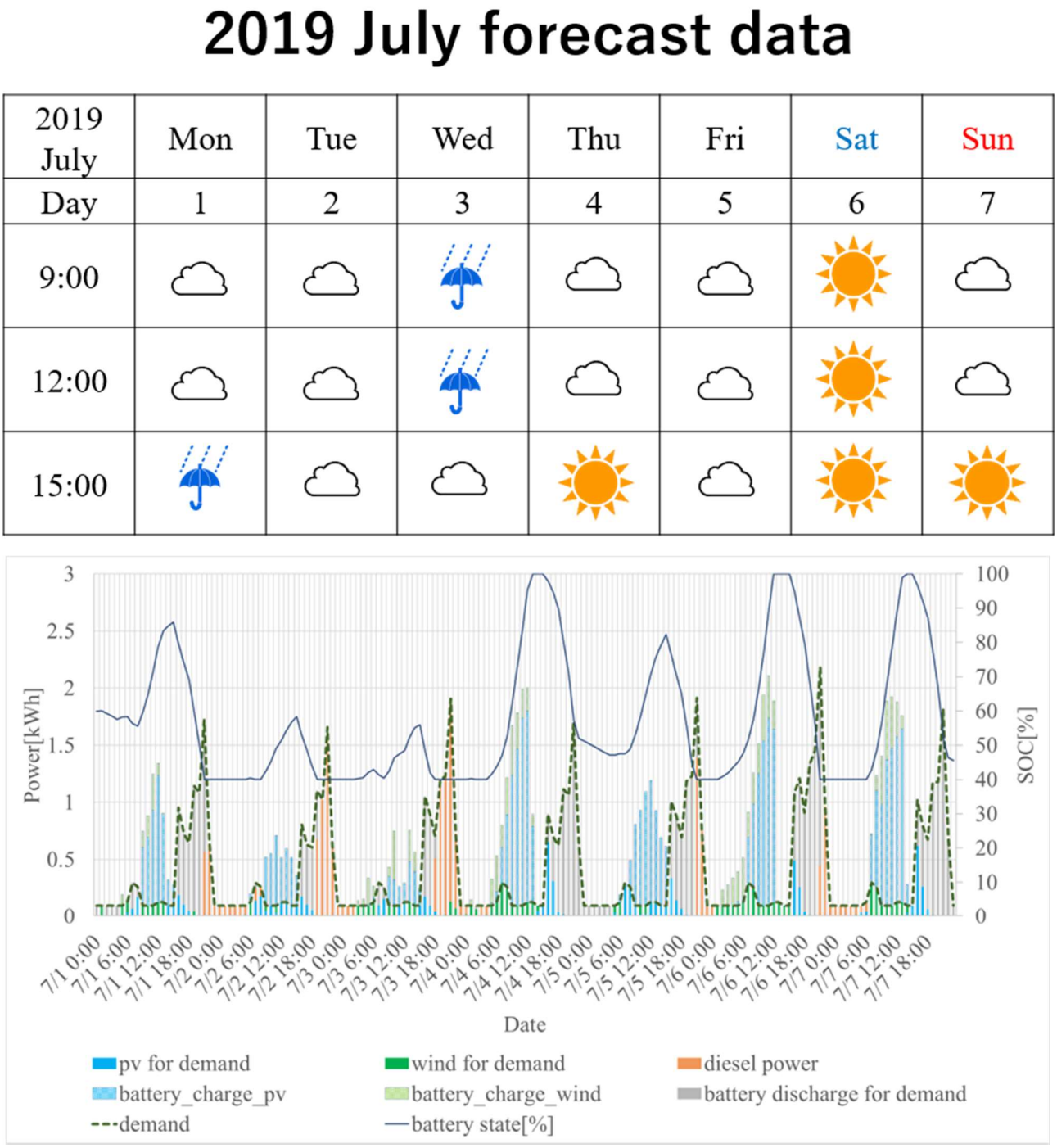

Figure 6.41: Electricity supply mix based on using 2018 forecast data

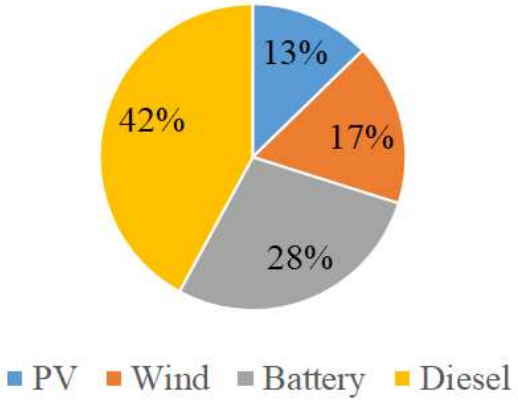

Figure 6.42: Electricity supply between 7/1 and 7/7 based on using 2018 real data

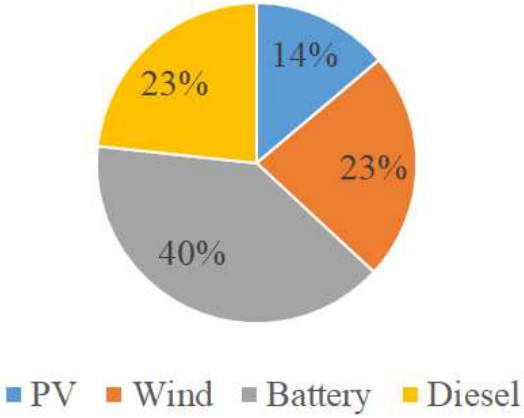

Figure 6.43: Electricity supply between 7/1 and 7/7 based on using 2019 real data

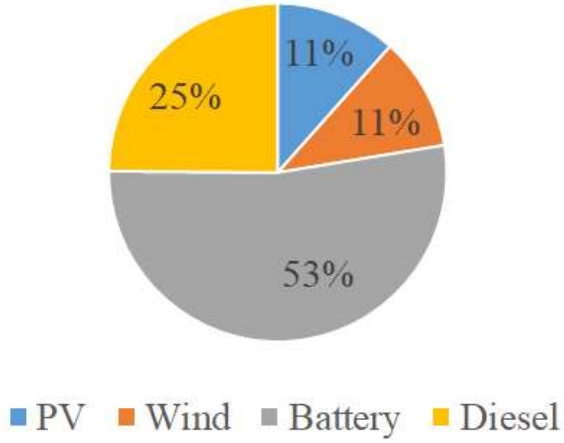

Figure 6.44: Electricity supply between 7/1 and 7/7 based on using 2019 forecast data

Chapter 7

Conclusion

This research introduced the optimal configuration and design of an autonomous renewable energy (RE) -based microgrid system which is used in order to meet the electrical load requirement in a selected Japnese standard building in Kasuga City, Fukuoka prefecture. The proposed system consists of a cluster of loads and micro-sources such as wind turbines, photovoltaic panels, battery storage, diesel generators and bi-directional converters.

To this aim, an optimization model was developed, based on the PSO approach, using the least cost perceptive approach and the load patterns of the residential end-uses. Based on the model results, the optimal size of the main components of the system was estimated as: PV: 2.65 kW, wind power: 2.01 kW, battery: 14.86kW, diesel generator: 3.6 kW, converter: 2.8 kW.

The total cost of the proposed system was estimated at 4.65 million yen. The LCOE of the proposed system was estimated at 95.3 yen / kWh, which is much higher than the average electricity rate in Japan (22 yen / kWh). The share of each power source of the proposed microgrid in supplying the annual electrical load demand of the selected building was estimated as: 43.4% solar PV, 16.7% wind, 4.9% diesel generator, and 35% battery discharge. The model results show that the operation of the proposed microgrid system is highly dependent on batteries and solar power.

The model results revealed that the power loss due to the charging and discharging efficiency of the battery is extremely large at about 720 kWh per year. This value accounts for about 30% of the total power consumption due to annual demand. This indicates that improving the charging and discharging efficiency of batteries is a very important factor for the effective use of renewable energy. Besides, mainly in the spring, there is a relatively long period when there is enough battery capacity. Therefore, there is a possibility that surplus power can be sent back to the grid, using the Feed-in-Tariff scheme. Furthermore, based on the weather forecast data provided by the Japan Meteorological Agency, we investigated the remarkable impact of weather conditions on power generation from the proposed microgrid and how forecasting of the weather data will help in managing the battery operation through monitoring its SOC condition and lowering the usage of fossil fuel in the diesel generators, especially during the typhoons and rainy seasons. This useful information can be used in developing the power dispatching strategy for the proposed microgrid and the demand response management.

Based on the research results, development of a comprehensive software entitled "MEDDULA" has been begun which can automatically collect the weather data of each city in Japan provided by the Japan Meteorological Agency to calculate the amount of renewable energy generated by the different generators and to find the optimal configuration of the selected microgrid system.

The development of an experimental setup based on the optimal results obtained from the model will also be considered as the next step of this research.

Appendix I

EnergyPlus load demand calculation

The building energy analysis program allows us to simulate buildings and their mechanical systems throughout the year. There are two main usage methods, the heat balance method and the weight coefficient method. In either case, such a simulation can provide a detailed breakdown of building energy usage over time. Building Loads Analysis and System Thermodynamics (BLAST) program are adopted as a "test bed" program for various ways to integrate building-mechanical system simulation using heat balance method. In the current version of BLAST, the building, its air handling system, and its equipment are simulated continuously without feedback. That is, the state of the building is entered into the air conditioning system and the response is determined, but the response does not affect the building.

In BLAST, there are three main sections, providing a complete simulation of buildings, fan systems, and facilities. Load simulation models all heat transfer of each building zone through zone surface by conduction, convection, and radiation considered to be of long wave (infrared) and short wave (visible) components. In addition, the load simulation models the effects of zones adjacent to each other due to the influence of people, lighting and equipment in the zone, conduction through the zone walls, mixing of zone air, and penetration of outside air into the zone.

The BLAST can simulate an air handling system that derives the supply air flow volume flow rate and temperature necessary to maintain the zone at the desired temperature and adjusts each zone of the fan system simulation. The simulation considers the influence of external conditions on the operation of system components. BLAST first performs the loads simulation by computing an hourly energy balance for each zone using weather, scheduled loads (lights, people, etc.) and desired zone conditions. This energy balance is represented as follows:

$$\sum Q_c + \sum_{i=1}^{nsurfaces} h_i A_i (T_{si} - T_Z) + \dot{m}_{inf} c_p (T_\infty - T_Z) + \sum_{i=1}^{nzones} \dot{m}_i c_p (T_{zi} - T_z) + Q_{sys} = 0 \quad (60)$$

Where $\sum Q_c$ is the sum of the internal loads, $\sum_{i=1}^{nsurfaces} h_i A_i (T_{si} - T_Z)$ represents convective heat transfer from the zone surfaces, $\dot{m}_{inf} c_p (T_\infty - T_Z)$ is infiltration of outside air, $\sum_{i=1}^{nzones} \dot{m}_i c_p (T_{zi} - T_z)$ represents inter zone air mixing, and Q_{sys} represents the system output. Internal load occurs when lighting, electrical equipment, people, etc. exist in the zone and are specified as input. The heat transfer through the zone surface is calculated from the surface convection coefficient h_i and the surface temperature T_{si} and each surface or element is assumed to be isothermal in BLAST. The surface temperature is calculated by calculating the heat balance of the inner and outer surfaces and relating the conditions of the entire surface using a transfer function. When outside air is mixed in the room, the penetration rate is specified in the input. And the outside air is due to doors and windows open to the outside environment. Since the energy Q_{sys} of the air conditioning system supplied to the zone is the difference between the supply air enthalpy and the air enthalpy leaving the zone, it can be expressed by the following equation.

$$Q_{sys} = mT_z + b \quad (61)$$

Appendix I

Or

$$Q_{sys} = \dot{m}_{sys} C_p (T_{supply} - T_z) \tag{62}$$

Where m is the slope of a linear segment in the control profile and b is the segment endpoint. The desired zone temperature is achieved by using line segments with different slopes to manipulate the shape of the control profile. Therefore, the gradient m can generally be expressed by the following expression.

$$m = \frac{dQ_{sys}}{dT_z} \tag{63}$$

When the zone temperature T_z is derived by substituting the equation (2) into the equation of the zone balance of the equation (1).

$$T_z = \frac{\sum Q_c + \sum_{i=1}^{nsurfaces} h_i A_i T_{si} + \dot{m}_{inf} c_p T_\infty + \sum_{i=1}^{nzones} \dot{m}_i c_p T_{zi} + b}{\sum_{i=1}^{nsurfaces} h_i A_i + \dot{m}_{inf} c_p + \sum_{i=1}^{nzones} \dot{m}_i c_p - m} \tag{64}$$

In the case of Energy Plus, the sum of the zone load and the air system output is equal to the change in energy stored in the zone, and typically states that capacity C_z is due only to that zone air.

$$C_z \frac{dT_z}{dt} = \sum Q_c + \sum_{i=1}^{nsurfaces} h_i A_i (T_{si} - T_Z) + \dot{m}_{inf} c_p (T_\infty - T_Z) + \sum_{i=1}^{nzones} \dot{m}_i c_p (T_{zi} - T_z) + \dot{m}_{sys} c_p (T_{supply} - T_z) \tag{65}$$

Next, using backward difference, $\frac{dT_z}{dt}|_t$ can be expressed as follows.

$$\frac{dT_z}{dt}|_t \approx (\delta t)^{-1} (T_Z^t - T_Z^{t-\delta t}) + O(\delta t) \tag{66}$$

Using this formula, deriving T based on equation (1) can be expressed as follows.

$$T_z^t = \left(\frac{\sum Q_c + \sum_{i=1}^{nsurfaces} h_i A_i T_{si} + \dot{m}_{inf} c_p T_\infty + \sum_{i=1}^{nzones} \dot{m}_i c_p T_{zi} + Q_{sys}}{\sum_{i=1}^{nsurfaces} h_i A_i + \dot{m}_{inf} c_p + \sum_{i=1}^{nzones} \dot{m}_i c_p} \right)^{(t-\delta t)} \tag{67}$$

However, with this deriving method, the response of the system output is delayed by one step from the zone load. Therefore, we need to show that it does not strongly affect the stability of the scheme. Thus, in BLAST, Q_{sys} is formulated primarily using mass flow rate and feed air temperature provided to the simulated system.

Appendix I

$$\dot{Q}_{sys} = \dot{m}_{sys} C_p (T_{supply} - T_z) \tag{68}$$

In this case, standby temperature T can be expressed as follows using the delay method.

$$T_z^t = \left(\frac{\sum Q_c + \sum_{i=1}^{nsurfaces} h_i A_i T_{si} + \dot{m}_{inf} c_p T_\infty + \sum_{i=1}^{nzones} \dot{m}_i c_p T_{zi} + \dot{m}_{sys} c_p T_{supply}}{\sum_{i=1}^{nsurfaces} h_i A_i + \dot{m}_{inf} c_p + \sum_{i=1}^{nzones} \dot{m}_i c_p + \dot{m}_{sys} c_p} \right)^{(t-\delta t)} \tag{69}$$

Since the equation (1) showing the energy balance is not established due to the response delay, the right side of the equation (1) is not 0, and the difference is set as C_z indicating the accumulated change of the zone energy.

Then, C_z can be expressed from the equation (1) as follows.

$$C_z \frac{dT_z}{dt} = \sum Q_c + \sum_{i=1}^{nsurfaces} h_i A_i (T_{si} - T_Z) + \dot{m}_{inf} c_p (T_\infty - T_Z) + \sum_{i=1}^{nzones} \dot{m}_i c_p (T_{zi} - T_z) + \dot{m}_{sys} c_p (T_{supply} - T_z) \tag{70}$$

When derivingC_z, the derivative term $\frac{dT_z}{dt}$ can be calculated using the following backward difference.

$$\frac{dT_z}{dt}|_t \approx (\delta t)^{-1} (T_Z^t - T_Z^{t-\delta t}) + O(\delta t) \tag{71}$$

From this equation, when deriving the zone air temperature using the Euler approximation, the following equation is obtained.

$$C_z \frac{T_Z^t - T_Z^{t-\delta t}}{\delta t} = \left(\sum Q_c + \sum_{i=1}^{nsurfaces} h_i A_i (T_{si} - T_Z) + \dot{m}_{inf} c_p (T_\infty - T_Z) + \sum_{i=1}^{nzones} \dot{m}_i c_p (T_{zi} - T_z) + \dot{m}_{sys} c_p (T_{supply} - T_z) \right)^{(t-\delta t)} \tag{72}$$

By explicitly computing T_z we can derive the temperature of the zone of the next time step relative to the previous time step condition.

$$T_Z^t = T_Z^{t-\delta t} + \frac{\delta t}{C_z} \left(\sum Q_c + \sum_{i=1}^{nsurfaces} h_i A_i (T_{si} - T_Z) + \dot{m}_{inf} c_p (T_\infty - T_Z) + \sum_{i=1}^{nzones} \dot{m}_i c_p (T_{zi} - T_z) + \dot{m}_{sys} c_p (T_{supply} - T_z) \right)^{(t-\delta t)} \tag{73}$$

And this equation can group all terms including zone air on the left side.

Appendix I

$$C_z \frac{T_Z^t - T_Z^{t-\delta t}}{\delta t} + \sum_{i=1}^{nsurfaces} h_i A_i T_Z^t + \dot{m}_{inf} c_p T_Z^t + \sum_{i=1}^{nzones} \dot{m}_i c_p T_z^t + \dot{m}_{sys} c_p T_z^t = \left(\sum Q_c + \sum_{i=1}^{nsurfaces} h_i A_i T_{si} + \dot{m}_{inf} c_p T_\infty + \sum_{i=1}^{nzones} \dot{m}_i c_p T_{zi} + \dot{m}_{sys} c_p T_{supply} \right)^{(t-\delta t)} \quad (74)$$

From this, the right side can be divided by the coefficientT_z. From the result, an energy balance equation similar to the delay system considering the influence of the band air capacity can be calculated.

$$T_Z^t = \frac{\left(\sum Q_c + \sum_{i=1}^{nsurfaces} h_i A_i T_{si} + \dot{m}_{inf} c_p T_\infty + \sum_{i=1}^{nzones} \dot{m}_i c_p T_{zi} + \dot{m}_{sys} c_p T_{supply} \right)^{(t-\delta t)}}{\left(\frac{C_z}{\delta t} + \sum_{i=1}^{nsurfaces} h_i A_i + \dot{m}_{inf} c_p + \sum_{i=1}^{nzones} \dot{m}_i c_p + \dot{m}_{sys} c_p \right)} \quad (75)$$

However, since certain conditioning can severely limit the time step size, EnergyPlus uses the first derivative with the corresponding higher-order truncation error in higher order expressions.

Using Taylor expansion to approximate second to fifth orders, Energy Plus states that the third-order finite difference approximation given below gives the best results.

$$\frac{dT_z}{dt} |_t = (\delta t)^{-1} \left(\frac{11}{6} T_Z^t - 3T_Z^{t-\delta t} + \frac{3}{2} T_Z^{t-2\delta t} - \frac{1}{3} T_Z^{t-3\delta t} \right) + O(\delta t^3) \quad (76)$$

Using this approximate expression, T_z can be derived according to the above flow, as follows.

$$T_Z^t = \frac{1}{\left(\frac{11}{6}\right)\frac{C_z}{\delta t} + \sum_{i=1}^{nsurfaces} h_i A_i + \dot{m}_{inf} c_p + \sum_{i=1}^{nzones} \dot{m}_i c_p + \dot{m}_{sys} c_p} \left(\sum Q_c + \sum_{i=1}^{nsurfaces} h_i A_i T_{si} + \dot{m}_{inf} c_p T_\infty + \sum_{i=1}^{nzones} \dot{m}_i c_p T_{zi} + \dot{m}_{sys} c_p T_{supply} - \left(\frac{C_z}{\delta t}\right) \left(-3T_Z^{t-\delta t} + \frac{3}{2} T_Z^{t-2\delta t} - \frac{1}{3} T_Z^{t-3\delta t} \right) \right) \quad (77)$$

This is the form historically used in EnergyPlus and is the current default referred to as 3rdOrderBackwardDifference in the ZoneAirHeatBalanceAlgorithm object. This algorithm requires zone air temperatures at three previous time steps and uses constant temperature coefficients. The assumption is that three previous time steps lengths are the same.

$$\dot{Q}_{sys} = \dot{m}_{sys} C_p \eta (T_{supply} - T_{Z,desired}) \quad (78)$$

Where η is the fraction of the time step that the air system is turned on and varies between 0 and 1.

Appendix Ⅰ

REFERENCES

[1] A. for Natural Resources, Energy, Energy white paper 2019, (n.d.). https://www.enecho.meti.go.jp/about/whitepaper/2019html/ (accessed December 14, 2019).
[2] T. of Economy, I.A. for Natural Resources, Energy, Japan`s Energy 2018, 10 Questions for Understanding the Current Energy Situation, (2018). https://www.enecho.meti.go.jp/en/category/brochures/pdf/japan_energy_2018.pdf.
[3] FY2016 Annual Report on Energy (Energy White Paper), (2017). https://www.meti.go.jp/english/report/downloadfiles/2017_outline.pdf.
[4] T.F. of Electric Power Companies of Japan, Why is Nuclear Energy Necessary in Japan?, (n.d.). https://www.fepc.or.jp/english/nuclear/necessary/index.html (accessed December 14, 2019).
[5] T. y Agency for Natural Resources aMinistry of Economy, I.A. for Natural Resources, Energy, JAPAN'S ENERGY 20 Questions to understand the current energy situation, (2017). https://www.enecho.meti.go.jp/en/category/brochures/pdf/japan_energy_2017.pdf.
[6] G. Horst, R. Dugan, Virtual Power Plant Modeling & Simulation, Electr. Power Res. Inst. (n.d.). https://smartgrid.epri.com/doc/07_AEP Smart Grid Project Modeling and Simulations.pdf (accessed December 15, 2019).
[7] B. Zhao, X. Zhang, J. Chen, C. Wang, L. Guo, Operation Optimization of Standalone Microgrids Considering Lifetime Characteristics of Battery Energy Storage System, IEEE Trans. Sustain. Energy. 4 (2013) 934–943. doi:10.1109/TSTE.2013.2248400.
[8] W. Zhang, A. Maleki, M.A. Rosen, J. Liu, Sizing a stand-alone solar-wind-hydrogen energy system using weather forecasting and a hybrid search optimization algorithm, Energy Convers. Manag. 180 (2019) 609–621. doi:10.1016/j.enconman.2018.08.102.
[9] A.H. Fathima, K. Palanisamy, S. Twaha, M.A.M. Ramli, R. Atia, N. Yamada, Optimization in microgrids with hybrid energy systems – A review, Renew. Sustain. Energy Rev. 45 (2015) 431–446. doi:https://doi.org/10.1016/j.rser.2015.01.059.
[10] A.L. Bukar, C.W. Tan, K.Y. Lau, Optimal sizing of an autonomous photovoltaic/wind/battery/diesel generator microgrid using grasshopper optimization algorithm, Sol. Energy. 188 (2019) 685–696. doi:10.1016/j.solener.2019.06.050.
[11] D. Neves, M.C. Brito, C.A. Silva, Impact of solar and wind forecast uncertainties on demand response of isolated microgrids, Renew. Energy. 87 (2016) 1003–1015. doi:10.1016/j.renene.2015.08.075.
[12] R. Jing, M. Wang, Z. Zhang, J. Liu, H. Liang, C. Meng, N. Shah, N. Li, Y.Y. Zhao, Y. Lu, S. Wang, Y.Y. Zhao, C. Yan, Renewable energy system optimization of low/zero energy buildings using single-objective and multi-objective optimization methods, Energy Build. 89 (2019) 123–139. doi:10.1016/j.enbuild.2019.04.023.
[13] M. Sharafi, T.Y. ELMekkawy, Multi-objective optimal design of hybrid renewable energy systems using PSO-simulation based approach, Renew. Energy. 68 (2014) 67–79. doi:10.1016/j.renene.2014.01.011.
[14] L. Kuznia, B. Zeng, G. Centeno, Z. Miao, Stochastic optimization for power system configuration with renewable energy in remote areas, Ann. Oper. Res. 210 (2013) 411–432. doi:10.1007/s10479-012-1110-9.
[15] T. Khatib, A. Mohamed, K. Sopian, Optimization of a PV/wind micro-grid for rural housing electrification using a hybrid iterative/genetic algorithm: Case study of Kuala Terengganu, Malaysia, Energy Build. 47 (2012) 321–331. doi:10.1016/j.enbuild.2011.12.006.
[16] A.-T.A.E.M.F.-F.M. Ahmarinezhad A., Optimal sizing of a stand alone hybrid system for Ardabil area of Iran (2012) IJTPE, 4 (12), pp. 118-125., (n.d.).

References

[17] G. Giannakoudis, A.I. Papadopoulos, P. Seferlis, S. Voutetakis, Optimum design and operation under uncertainty of power systems using renewable energy sources and hydrogen storage, Int. J. Hydrogen Energy. 35 (2010) 872–891. doi:10.1016/j.ijhydene.2009.11.044.

[18] A. Kashefi Kaviani, G.H. Riahy, S.M. Kouhsari, Optimal design of a reliable hydrogen-based stand-alone wind/PV generating system, considering component outages, Renew. Energy. 34 (2009) 2380–2390. doi:10.1016/j.renene.2009.03.020.

[19] Y.P. Cai, G.H. Huang, Q. Tan, Z.F. Yang, Planning of community-scale renewable energy management systems in a mixed stochastic and fuzzy environment, Renew. Energy. 34 (2009) 1833–1847. doi:10.1016/j.renene.2008.11.024.

[20] J. Lagorse, M.G. Simões, A. Miraoui, P. Costerg, Energy cost analysis of a solar-hydrogen hybrid energy system for stand-alone applications, Int. J. Hydrogen Energy. 33 (2008) 2871–2879. doi:10.1016/j.ijhydene.2008.03.054.

[21] R. Dufo-López, J.L. Bernal-Agustin, J. Contreras, Optimization of control strategies for stand-alone renewable energy systems with hydrogen storage, Renew. Energy. 32 (2007) 1102–1126. 10.1016/j.renene.2006.04.013.

[22] R.S. Garcia, D. Weisser, A wind-diesel system with hydrogen storage: Joint optimisation of design and dispatch, Renew. Energy. 31 (2006) 2296–2320. doi:10.1016/j.renene.2005.11.003.

[23] E. Koutroulis, D. Kolokotsa, A. Potirakis, K. Kalaitzakis, Methodology for optimal sizing of stand-alone photovoltaic/wind-generator systems using genetic algorithms, Sol. Energy. 80 (2006) 1072–1088. doi:10.1016/j.solener.2005.11.002.

[24] E. Craparo, M. Karatas, D.I. Singham, A robust optimization approach to hybrid microgrid operation using ensemble weather forecasts, Appl. Energy. 201 (2017) 135–147. doi:10.1016/j.apenergy.2017.05.068.

[25] S. Salcedo-Sanz, M.P.B. Ángel, E.G. Ortiz-Garcia, A. Portilla-Figueras, L. Prieto, D. Paredes, E.G. Ortiz-García, A. Portilla-Figueras, L. Prieto, D. Paredes, Hybridizing the fifth generation mesoscale model with artificial neural networks for short-term wind speed prediction, Renew. Energy. 34 (2009) 1451–1457. doi:10.1016/j.renene.2008.10.017.

[26] S.S. Soman, H. Zareipour, O. Malik, P. Mandal, A review of wind power and wind speed forecasting methods with different time horizons, North Am. Power Symp. 2010, NAPS 2010. (2010) 1–8. doi:10.1109/NAPS.2010.5619586.

[27] J.G.D.S.F. Junior, T. Oozeki, H. Ohtake, K. ichi Shimose, T. Takashima, K. Ogimoto, J.G. Da Silva Fonseca Junior, T. Oozeki, H. Ohtake, K. ichi Shimose, T. Takashima, K. Ogimoto, Regional forecasts and smoothing effect of photovoltaic power generation in Japan: An approach with principal component analysis, Renew. Energy. 68 (2014) 403–413. doi:10.1016/j.renene.2014.02.018.

[28] J.M. Agency, Start providing solar radiation forecast data, (2017). https://www.jma.go.jp/jma/press/1712/05a/20171205_nissha.html (accessed December 15, 2019).

[29] K. Saito, J.I. Ishida, K. Aranami, T. Hara, T. Segawa, M. Narita, Y. Honda, Nonhydrostatic atmospheric models and operational development at JMA, J. Meteorol. Soc. Japan. 85 B (2007) 271–304. doi:10.2151/jmsj.85B.271.

[30] J.M. Agency, Numerical forecast commentary (numerical forecast training text), (n.d.). https://www.jma.go.jp/jma/kishou/books/nwptext/nwptext.html (accessed December 15, 2019).

[31] B. Homan, M. V. ten Kortenaar, J.L. Hurink, G.J.M.M. Smit, A realistic model for battery state of charge prediction in energy management simulation tools, Energy. 171 (2019) 205–217. doi:10.1016/j.energy.2018.12.134.

[32] B.P. Roberts, C. Sandberg, The role of energy storage in development of smart grids, Proc. IEEE. 99 (2011) 1139–1144. doi:10.1109/JPROC.2011.2116752.

References

[33] E. Koliou, C. Eid, J.P. Chaves-Ávila, R.A. Hakvoort, Demand response in liberalized electricity markets: Analysis of aggregated load participation in the German balancing mechanism, Energy. 71 (2014) 245–254. doi:10.1016/j.energy.2014.04.067.

[34] J. Kennedy, R. Eberhart, Particle swarm optimization, in: Proc. ICNN'95 - Int. Conf. Neural Networks, 1995. 10.1109/ICNN.1995.488968.

[35] K.E. Parsopoulos, M.N. Vrahatis, On the Computation of all global minimizers through particle swarm optimization, IEEE Trans. Evol. Comput. 8 (2004) 211–224. doi:10.1109/TEVC.2004.826076.

[36] Agency for Natural Resources and Energy, What is renewable energy?, (n.d.). https://www.enecho.meti.go.jp/category/saving_and_new/saiene/index.html (accessed January 14, 2020).

[37] J.A. Duffie, W.A. Beckman, Solar Engineering of Thermal Processes, Wiley, 1991. https://books.google.co.jp/books?id=w0QzhrBV21gC.

[38] HOMER Pro 3.12 User Manual, (n.d.). https://www.homerenergy.com/products/pro/docs/ (accessed December 13, 2019).

[39] B.K. Das, N. Hoque, S. Mandal, T.K. Pal, M.A. Raihan, A techno-economic feasibility of a stand-alone hybrid power generation for remote area application in Bangladesh, Energy. 134 (2017) 775–788. doi:10.1016/j.energy.2017.06.024.

[40] A.B. Forough, R. Roshandel, A. Behzadi Forough, R. Roshandel, Multi objective receding horizon optimization for optimal scheduling of hybrid renewable energy system, Energy Build. 150 (2017) 583–597. doi:10.1016/j.enbuild.2017.06.031.

[41] M. Jamshidi, A. Askarzadeh, Techno-economic analysis and size optimization of an off-grid hybrid photovoltaic, fuel cell and diesel generator system, Sustain. Cities Soc. 44 (2019) 310–320. doi:10.1016/j.scs.2018.10.021.

[42] S. Dhundhara, Y.P. Verma, A. Williams, M. Ehsan, L. Kuznia, B. Zeng, . . . B. Guo, Techno-economic analysis of the lithium-ion and lead-acid battery in microgrid systems, Renew. Energy. 145 (2017) 304–317. doi:10.1016/j.enbuild.2017.04.028.

[43] 2009 ASHRAE handbook : fundamentals, in: 2009 ASHRAE Handb. Fundam., American Society of Heating, Refrigerating and Air-Conditioning Engineers, 2009.

[44] A. Bhatia, HVAC cooling load calculations and principles, New York Contin. Educ. (2012).

[45] V. Shabunko, C.M. Lim, S. Mathew, EnergyPlus models for the benchmarking of residential buildings in Brunei Darussalam, Energy Build. 169 (2018) 507–516. doi:https://doi.org/10.1016/j.enbuild.2016.03.039.

[46] S. Twaha, M.A.M.M. Ramli, A review of optimization approaches for hybrid distributed energy generation systems: Off-grid and grid-connected systems, Sustain. Cities Soc. 41 (2018) 320–331. doi:10.1016/j.scs.2018.05.027.

[47] W.J. Zhang, X.F. Xie, D.C. Bi, Handling boundary constraints for numerical optimization by particle swarm flying in periodic search space, Proc. 2004 Congr. Evol. Comput. CEC2004. 2 (2004) 2307–2311.

[48] K. Parsopoulos, M. Vrahatis, Particle Swarm Optimization Method for Constrained Optimization Problem, in: Front. Artif. Intell. Appl., 2002: pp. 214–220.

[49] S. Xu, Y. Rahmat-Samii, Boundary conditions in particle swarm optimization revisited, IEEE Trans. Antennas Propag. 55 (2007) 760–765. doi:10.1109/TAP.2007.891562.

[50] H. Seko, T. Miyoshi, Y. Shoji, K. Saito, Data assimilation experiments of precipitable water vapour using the LETKF system: intense rainfall event over Japan 28 July 2008, Tellus A Dyn. Meteorol. Oceanogr. 63 (2011) 402–414. doi:10.1111/j.1600-0870.2010.00508.x.

[51] W. Iqbal, A. Hannachi, T. Hirooka, L. Chafik, Y. Harada, Troposphere-stratosphere dynamical coupling in regard to the north atlantic eddy-driven jet variability, J. Meteorol. Soc. Japan. 97 (2019) 657–671. doi:10.2151/jmsj.2019-037.

References

[52] M. Nishio, M. Mori, WEB-BASED DELIVERY SYSTEM for DISASTER PREVENTION INFORMATION USING A NEW JMA DPI XML FORMAT and AMEDAS DATA, ISPRS Ann. Photogramm. Remote Sens. Spat. Inf. Sci. 1 (2012) 23–27. doi:10.5194/isprsannals-I-4-23-2012.

[53] T. Misaki, T. Ohsawa, M. Konagaya, S. Shimada, Y. Takeyama, S. Nakamura, Accuracy Comparison of Coastal Wind Speeds between WRF Simulations Using Different Input Datasets in Japan, Energies. 12 (2019). doi:10.3390/en12142754.

[54] M. Jradi, C. Veje, B.N. Jørgensen, B.N., Deep energy renovation of the Mærsk office building in Denmark using a holistic design approach, Energy Build. 151 (2017) 306–319. doi:https://doi.org/10.1016/j.enbuild.2017.06.047.

[55] Reduction Effects of the cooling and heating load in a newly insulated wooden old house., in: The Society of Heating, Air-Conditioning and Sanitary Engineers of Japan, n.d.: pp. 369–372. 10.18948/shasetaikai.2004.1.0_369.

[56] S.L. Garvin, J. Wilson, Environmental conditions in window frames with double-glazing units, Constr. Build. Mater. 12 (1998) 289–302. doi:https://doi.org/10.1016/S0950-0618(98)00008-7.

[57] N.R.E.L. (NREL), Building Component Library (BCL), (n.d.).

[58] D.B. Crawley, L.K. Lawrie., Climate.OneBuilding.Org., (n.d.). http://climate.onebuilding.org/ (accessed December 13, 2019).

[59] B.L.S. LLC, EnergyPlus Version 8.7 Documents, (n.d.). https://bigladdersoftware.com/epx/docs/8-7/ (accessed December 5, 2019).

[60] A. for Natural Resources, Energy, Energy Saving Performance Catalog 2013 Summer Edition, in: Energy Sav. Perform. Cat. 2013 Summer Ed., . https://www.enecho.meti.go.jp/category/saving_and_new/saving/data/13summer0172.pdf.

[61] Panasonic, Panasonic Photovoltaic module HIT VBHN245SJ25 VBHN240SJ25, (n.d.). https://panasonic.net/lifesolutions/solar/download/pdf/VBHN245_240SJ25_ol_190226.pdf (accessed January 14, 2020).

[62] L. Idoko, O. Anaya-Lara, A. McDonald, Enhancing PV modules efficiency and power output using multi-concept cooling technique, Energy Reports. 4 (2018) 357–369. doi:10.1016/j.egyr.2018.05.004.

[63] Intelligent Energy - Europe, Catalogue of european urban wind turbine manufacturers, (2011) 61. http://123doc.org/document/1227748-catalogue-of-european-urban-wind-turbine-manufacturers-potx.htm.

[64] Panasonic, Panasonic residential catalog, (n.d.) 52. https://sumai.panasonic.jp/catalog/solarsystem.html (accessed December 10, 2018).